NASA Contractor Report 4405

Development of Unsteady Aerodynamic Analyses for Turbomachinery Aeroelastic and Aeroacoustic Applications

Joseph M. Verdon, Mark Barnett,
Kenneth C. Hall, and Timothy C. Ayer

CONTRACT NAS3-25425
OCTOBER 1991

NASA

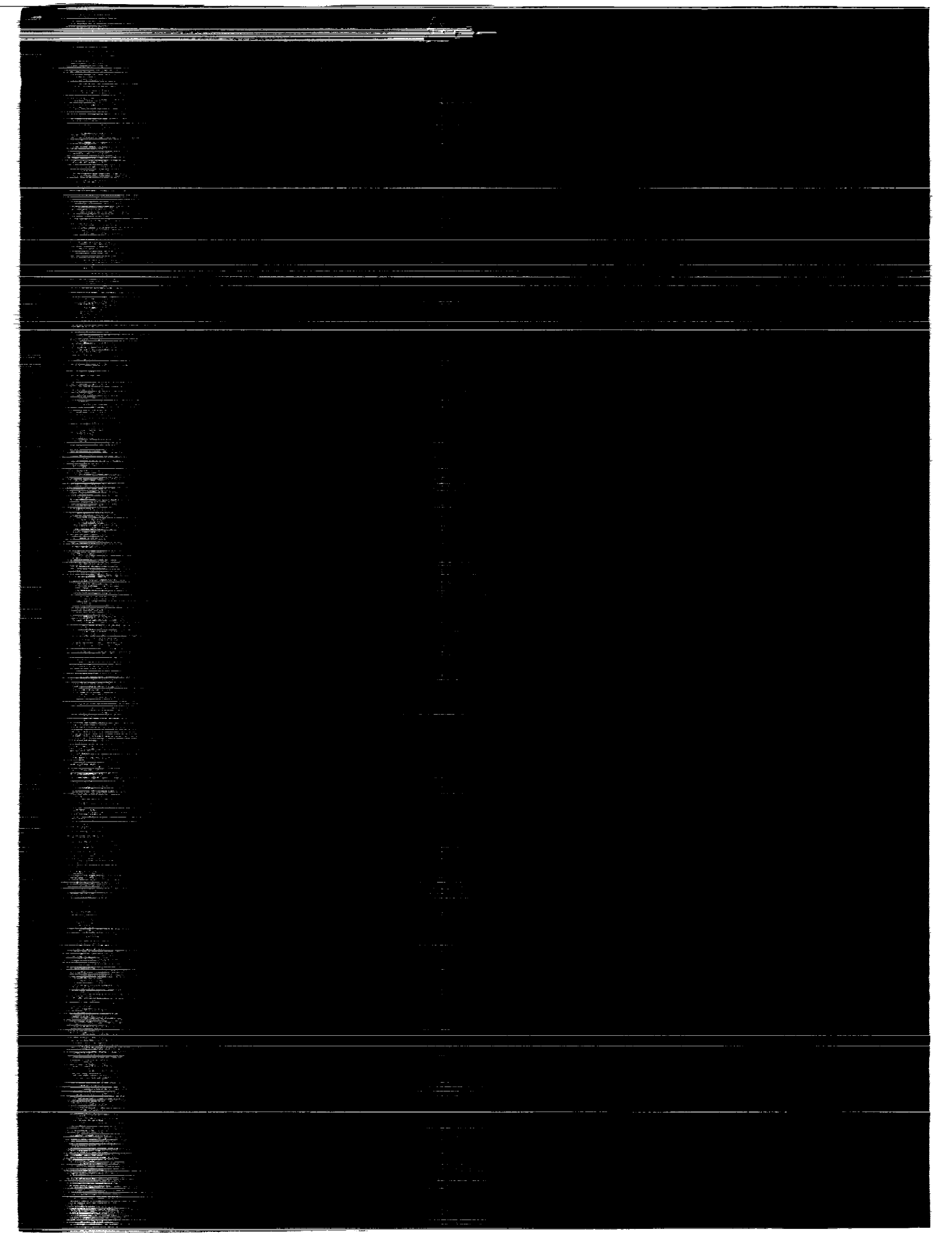

NASA Contractor Report 4405

Development of Unsteady Aerodynamic Analyses for Turbomachinery Aeroelastic and Aeroacoustic Applications

Joseph M. Verdon, Mark Barnett,
Kenneth C. Hall, and Timothy C. Ayer
United Technologies Research Center
East Hartford, Connecticut

Prepared for
Lewis Research Center
under Contract NAS3-25425

National Aeronautics and
Space Administration

Office of Management

Scientific and Technical
Information Program

1991

Development of Unsteady Aerodynamic Analyses for Turbomachinery Aeroelastic and Aeroacoustic Applications

Contents

Development of Unsteady Aerodynamic Analyses for Turbomachinery Aeroelastic and Aeroacoustic Applications

Summary

Theoretical analyses and computer codes are being developed under Contract NAS3–25425 for predicting compressible unsteady inviscid and viscous flows through blade rows. Such analyses are needed to determine the impact of unsteady flow phenomena on the structural durability and noise generation characteristics of turbomachinery blading. Emphasis is being placed on developing analyses based on asymptotic representations of unsteady flow phenomena. Thus, flows driven by small-amplitude unsteady excitations in which viscous effects are concentrated in thin layers are being considered. The resulting analyses should apply in many practical situations, lead to a better understanding of the relevant physics, and they will be efficient computationally, and therefore, appropriate for aeroelastic and aeroacoustic design applications.

Under the present phase (Task III) of this contract research program, the effort has been focused on providing inviscid and viscid prediction capabilities for subsonic unsteady cascade flows. Thus, a composite (global/local) mesh, gust response solution capability for the linearized inviscid component of the flow has been developed, and an existing nonlinear viscous-layer analysis has been extended and coupled to the inviscid analysis to provide a weak inviscid/viscid interaction solution capability for unsteady cascade flows. The linearized inviscid and the nonlinear viscous layer analyses are described in detail in this report. Numerical results are also presented to illustrate the effects of vortical excitation on the inviscid pressure response and acoustic excitation on the viscous-layer response for representative two-dimensional compressor, turbine and flat plate cascade configurations. These results show that nonuniform mean flow phenomena can have a substantial impact on the response of cascades to vortical gusts, particularly for gusts occurring at high wave numbers. In addition, for flat plate cascades the viscous-layer responses to acoustic excitations from upstream tend to be linear, but high frequency or high amplitude acoustic excitations from downstream, which travel against the main stream flow direction, are likely to excite significant nonlinear responses. Finally, because of boundary layer separation, weak inviscid/viscid interaction solutions can only be determined for a very restricted range of flow conditions. Therefore, a strong, or simultaneous, coupling of the inviscid and viscous-layer analyses must be developed to provide a useful unsteady viscous aerodynamic analysis for realistic cascade configurations.

1. Introduction

The unsteady aerodynamic analyses intended for turbomachinery aeroelastic and aeroacoustic predictions must be applicable over a wide range of operating conditions and to unsteady excitations at moderate through high reduced frequencies. In addition, these analyses must be capable of predicting unsteady pressure responses that arise from various sources of excitation. The latter include structural (blade) motions, variations in total temperature and total pressure (entropy and vorticity waves) at inlet and variations in static pressure (acoustic waves) at inlet and exit. Finally, because of the large number of controlling parameters involved, there is a stringent requirement for computational efficiency, if the analysis is to be used successfully in the blade design process. To satisfy this latter requirement a number of restrictive assumptions must be introduced into the development of an appropriate unsteady aerodynamic model.

The theoretical analyses that have been developed to predict the aeroelastic and aeroacoustic behavior of turbomachinery blading, i.e., the onset of blade flutter, the amplitudes of forced blade vibration and the sound pressure levels upstream and downstream of the blade row, have, for the most part, been based on the following geometric and aerodynamic assumptions. The blades of an isolated, two-dimensional cascade are usually considered with the effects of neighboring structures being represented via prescribed nonuniform flow conditions at inlet and exit. In addition, the Reynolds number is assumed to be sufficiently high (i.e., $\mathrm{Re} \rightarrow \infty$) so that the displacement of the inviscid flow by viscous layers has a negligible impact on the unsteady pressure field. Finally, the unsteady excitations are assumed to be sufficiently small so that a linearized treatment of the unsteady inviscid flow is justified.

Until recently, the inviscid unsteady aerodynamic analyses that have been available for turbomachinery aeroelastic applications were based on classical linearized theory, as reviewed by Whitehead in Ref. [1]. Because of the limitations in physical modeling associated with the classical linearization researchers have developed more general inviscid unsteady aerodynamic linearizations. These account for the effects of important design features such as real blade geometry, mean blade loading and operation at transonic Mach numbers on the unsteady aerodynamic response of two-dimensional cascades [2, 3, 4]. The unsteady disturbances are regarded as small-amplitude harmonic fluctuations relative to a nonuniform steady (in a coordinate frame attached to the blade row) background flow. The steady flow is determined as a solution of a nonlinear inviscid equation set, and the linearized unsteady flow, as the solution of a set of linear equations with variable coefficients that depend on the underlying steady flow. This type of analytical model has received considerable attention in recent years, and we refer the reader to the articles by Whitehead [5] and Verdon [6, 7] for a description of the theoretical formulation and recent numerical results.

In particular, the linearized inviscid flow analysis (LINFLO), described in Refs. [6] and [7], employs a velocity decomposition introduced by Goldstein [8, 9], and later modified by Atassi and Grzedzinski [10], to split the linearized unsteady velocity into rotational and irrotational components. This decomposition leads to a very convenient description of the linearized unsteady perturbation — one in which closed form solutions can be determined for the entropy and rotational velocity fluctuations in terms of the drift and stream functions of the underlying steady flow and numerical field methods are required only to determine the

unsteady potential. The latter is governed by an inhomogeneous wave equation in which the source term depends only upon the rotational velocity field. Finite-difference procedures for solving the potential equation have been developed for the prediction of unsteady subsonic and transonic flows excited by blade vibrations or acoustic disturbances [11], and for the prediction of unsteady subsonic flows excited by entropic and vortical gusts [12].

The unsteady flows of practical interest usually occur at high, but finite Reynolds number, so that viscous effects can have an impact on the unsteady pressure response. Provided that large-scale flow separations do not occur, the overall flow field can be separated conceptually into "inner" viscous or dissipative regions, consisting of thin layers that lie along the blade surfaces (boundary layers) and extend downstream from the blade trailing edges (wakes), and an "outer" inviscid region. Solutions to the complete flow problem can then be determined by an iterative process involving successive solutions of the inviscid and viscid equations. If the inviscid/viscid interaction is "weak", then at each step of the iteration, the inviscid and viscid solutions can be determined sequentially with the pressure being determined by the inviscid flow. However, in most flows, strong inviscid/viscid interactions occur due, for example, to boundary-layer separations, shock/boundary-layer interactions and trailing-edge/near-wake interactions, and the pressure must be determined by solving the inviscid and viscous layer equations simultaneously.

To date, there has been no effort to couple a viscous-layer analysis to the steady and linearized unsteady inviscid aerodynamic analyses that have been developed for turbomachinery aeroelastic and aeroacoustic applications. As a step toward this goal, a fully nonlinear unsteady viscous-layer analysis (UNSVIS), which can also be applied to predict steady flows, was developed in Ref. [13]. This approach, rather than one in which the results of separate nonlinear steady and linearized unsteady viscous analyses are superposed, will allow an assessment to be made of the relative importance of nonlinear unsteady effects in viscous regions. In the UNSVIS analysis the flow in the viscous layer is described by Prandtl's equations, with algebraic models used to account for the effects of transition and turbulence. These equations are solved in terms of Levy-Lees type variables using a finite-difference technique in which solutions are advanced in time and in the streamwise direction. Numerical solutions are determined by marching implicitly, first in time and then in the streamwise direction, over several periods of unsteady excitation from an initial steady solution, and from an approximate time-dependent, upstream flow solution. Numerical results were presented in [13] for flat-plate airfoils and for the turbine cascades, studied experimentally by Dring et al. [14, 15]. These were found to be in good agreement with previous analytical and numerical solutions for flat-plate airfoils and with the experimental results for the turbine cascades.

1.1 Scope of the Present Effort

The objective of the research program being conducted under Contract NAS3–25425 is to provide efficient theoretical analyses for predicting compressible unsteady flows through two-dimensional blade rows. Such analyses are needed to understand the impact of unsteady aerodynamic phenomena on the aeroelastic and aeroacoustic performance of the blading. The work being conducted under this contract is directed primarily towards low-speed aeroelastic applications, however, for the most part it will apply more generally to the aeroelastic and

aeroacoustic performance of turbomachinery blading operating at high subsonic through transonic Mach numbers.

In the first phase of this program [16] the linearized inviscid analysis (LINFLO) was extended to predict the response of a cascade to entropic and vortical excitations. Here, the velocity decomposition of Refs. [8]—[10] was employed to split the unsteady velocity into rotational and irrotational parts. Closed form solutions were then determined for the unsteady entropic and rotational velocity fluctuations, and the potential fluctuations were determined numerically on an H-type mesh in which the streamlines of the steady background flow were used as mesh lines. Numerical solutions were reported for several configurations including flat-plate cascades, a compressor exit guide vane, a high-speed compressor cascade, and a turbine cascade.

Under the present effort the linearized inviscid analysis (LINFLO) and the nonlinear viscous-layer analysis (UNSVIS) have been extended and coupled to provide a weak viscid/inviscid interaction solution capability for unsteady cascade flows. In particular, a composite (global/local) mesh solution capability for flows driven by entropic and vortical gusts has been incorporated into LINFLO. The meshes used in the composite analysis are the general curvilinear H-mesh of Refs. [12] and [16] and a polar type local mesh. Also, analytical expressions for the values of the inviscid flow variables at moving blade and wake surfaces, i.e., at the edge of viscous layers, have been developed and incorporated into LINFLO, to provide the inviscid information needed for an unsteady viscous-layer calculation.

The UNSVIS analysis has been extended so that the unsteady viscous effects in the vicinity of leading-edge stagnation points and in blade wakes can be predicted. In particular, a similarity analysis has been developed to predict unsteady viscous compressible flow in the vicinity of a moving leading-edge stagnation point and incorporated into the existing UNSVIS code. This analysis provides the "initial" upstream information needed to advance or march the viscous-layer calculation downstream along the blade and wake surfaces. Initial upstream profiles for the latter calculation are specified at a distance from the mean stagnation-point location which is beyond the furthest point at which any reverse flow, associated with the motion of the stagnation point, might occur. In addition, the wake analysis used previously in UNSVIS has been extended so that the changes or jumps in the inviscid velocity that occur across vortex-sheet unsteady wakes could be properly accommodated.

The linearized inviscid and nonlinear viscous-layer unsteady aerodynamic analyses are described in detail in this report, and demonstrated via application to several cascade configurations. In particular, the inviscid analysis has been applied to predict the pressure response of compressor and turbine cascades, and their flat plate counterparts, to vortical excitations. Our numerical results indicate that it is important to account for mean flow nonuniformity in predicting the pressure response resulting from the interaction of a vortical gust and a cascade, particularly for high-wave-number gusts. The nonlinear unsteady viscous-layer analysis has been applied to study the viscous-layer response of an unstaggered flat-plate cascade and a turbine cascade to external pressure excitations. The flat-plate results indicate that the viscous-layer responses to upstream pressure excitations are essentially linear over a broad range of excitation amplitudes and temporal frequencies, but significant nonlinear responses occur for downstream pressure excitations at high amplitude or high temporal frequency. Finally, the coupled LINFLO/UNSVIS analysis has been applied to a turbine cascade subjected to a pressure excitation from upstream to demonstrate the current

weak inviscid/viscid interaction solution capability on a realistic cascade configuration.

2. Physical Problem

We consider time-dependent, high Reynolds number (Re) flow, with negligible body forces, of a perfect gas with constant specific heats and constant Prandtl number (Pr) through a two-dimensional cascade, such as the one shown in Figure 1. The unsteady fluctuations in the flow arise from one or more of the following sources (Figure 2): blade motions, upstream entropic and vortical disturbances, and upstream and/or downstream acoustic disturbances which carry energy toward the blade row. These excitations are assumed to be of small amplitude, periodic in time, and periodic in the cascade "circumferential" direction.

The mean or steady-state positions of the blade chord lines coincide with the line segments $\eta = \xi \tan\Theta + mG, 0 \leq \xi \leq \cos\Theta, m = 0, \pm 1, \pm 2, \ldots$, where ξ and η are coordinates in the axial-flow and cascade directions, respectively, m is a blade number index, Θ is the cascade stagger angle, and $\mathbf{G}$ is the cascade gap vector which is directed along the η-axis with magnitude equal to the blade spacing. The blade motions, $\mathcal{R}_{\mathrm{B_m}}(\mathbf{x}, t)$, where $\mathcal{R}_{\mathrm{B_m}}$ is the displacement of a point on a moving blade surface ($\mathcal{B}_m$) relative to its mean or steady-state position (B_m), $\mathbf{x}$ is a position vector and t is time, are prescribed functions of $\mathbf{x}$ and t. The entropic, $\tilde{s}_{-\infty}(\mathbf{x}, t)$, vortical, $\tilde{\boldsymbol{\zeta}}_{-\infty}(\mathbf{x}, t)$, and acoustic, $\tilde{p}_{I,\mp\infty}(\mathbf{x}, t)$, excitations, where the subscripts $-\infty$ and $+\infty$ refer to the far upstream and far downstream flow regions, respectively, are also prescribed functions of $\mathbf{x}$ and t. However, a prescribed far-field behavior must be a solution of the fluid-dynamic field equations, and the incident pressure disturbances must satisfy the requirement that acoustic energy travels toward the blade row. Since the unsteady aerodynamic excitations are periodic in η and t, it is often useful to describe them via Fourier series representations. In this case the complex amplitudes, fundamental frequencies and fundamental circumferential wave numbers of the various excitations are the prescribed quantities.

We assume that far upstream (say $\xi < \xi_-$) and far downstream ($\xi > \xi_+$) from the blade row, the mean flow in the inviscid region is at most a small irrotational perturbation from a uniform free stream. In addition, any shocks that might occur are assumed to be of weak to moderate strength. Finally, blade shape and orientation relative to the inlet freestream direction, the inlet to exit mean static pressure ratio and the amplitudes, modes, frequencies and wave numbers of the unsteady excitations are such that viscous effects are confined within thin layers, which remain essentially attached to the blade surfaces, and extend downstream from the blade trailing edges.

In the present discussion all physical variables are dimensionless. Lengths are scaled with respect to blade chord, time with respect to the ratio of blade chord to upstream freestream flow speed, density and viscosity with respect to their upstream freestream values, respectively, velocity with respect to the upstream freestream flow speed, normal and shear stresses with respect to the product of the upstream freestream density and the square of the upstream freestream speed, temperature with respect to the square of the upstream freestream speed divided by the fluid specific heat at constant pressure, and entropy with respect to the fluid specific heat at constant pressure.

2.1 Mathematical Model

The field equations that govern the fluid motion follow from the mass, momentum and energy conservation laws and the thermodynamic relations for a perfect gas. After ensemble averaging the resulting equations, equations for the (statistical) mean values of the flow variables are determined. These contain turbulent correlations, which must be estimated empirically. As a consequence of the high Reynolds number assumption, separate sets of equations can be constructed to describe the flow in the "outer" inviscid region and in the "inner" viscous-layer regions. The flow in the inviscid region is governed by a coupled set of nonlinear differential equations (i.e., the Euler equations) along with jump conditions at shocks and at vortex-sheet unsteady wakes. In continuous subregions the energy equation can be replaced by the requirement that the entropy following a fluid particle must remain constant. In addition, the attached flow assumption requires that the inviscid unsteady flow must be tangential to the moving blade surfaces, and the uniform flow conditions at inlet and exit, the entropic and vortical fluctuations at inlet, and the static pressure disturbances at inlet and exit that carry energy towards the blade row must be specified. The flows in the viscous layers are governed by Prandtl's equations and are subject to no-slip conditions at the moving blade surfaces. In addition, the streamwise velocity and the thermodynamic properties of the fluid at the edges of the viscous layers must be matched to the corresponding inviscid quantities at the blade surfaces and along the reference wake streamline.

Even with the simplifications resulting from the high Reynolds number approximation, the unsteady aerodynamic problem still involves prohibitive computational times. Because of this, the traditional approach has been to examine linearized forms of the governing inviscid equations with the intention of providing useful theoretical predictions of the unsteady aerodynamic response information required for turbomachinery aeroelastic and aeroacoustic applications. In one such approach, the unsteady flow in the inviscid region is regarded as a small perturbation of a nonlinear mean or steady background flow. In this case the first-order unsteady fluid motions are governed by linear equations with variable coefficients that depend upon the steady background flow. In addition, the first-order motions that arise from the various Fourier modes of unsteady excitation are not coupled. Hence, they can be determined independently. Indeed, it is sufficient to develop solution procedures for a single harmonic (in t and η) component of a given disturbance. Solutions for arbitrary disturbances and arbitrary combinations of various disturbances can then be obtained by superposition.

Thus, in linearized inviscid analyses we consider small-amplitude blade motions of the form

$$\mathcal{R}_{\mathrm{B}_m}(\mathbf{x} + m\mathbf{G}, t) = \mathrm{Re}\{\mathbf{r}_{\mathrm{B}}(\mathbf{x}) \exp[i(\omega t + m\sigma)]\}, \quad \mathbf{x} \in \mathrm{B}\,, \tag{2.1}$$

where $\mathbf{r}_{\mathrm{B}}$ is the complex amplitude of the blade displacement, σ is the phase angle between the motions of adjacent blades, Re{ } denotes the real part of { } and B denotes the reference ($m = 0$) blade surface. The external aerodynamic excitations are small-amplitude, harmonic perturbations of a uniform freestream flow, and therefore must be of the form

$$\tilde{s}(\mathbf{x}, t) = \tilde{s}_{-\infty}(\mathbf{x} - \mathbf{V}_{-\infty} t) = \mathrm{Re}\{s_{-\infty} \exp[i(\boldsymbol{\kappa}_{-\infty} \cdot \mathbf{x} + \omega t)]\} \ldots\,, \quad \xi < \xi_-\,, \tag{2.2}$$

$$\tilde{\boldsymbol{\zeta}}(\mathbf{x}, t) = \tilde{\boldsymbol{\zeta}}_{-\infty}(\mathbf{x} - \mathbf{V}_{-\infty} t) = \mathrm{Re}\{\boldsymbol{\zeta}_{-\infty} \exp[i(\boldsymbol{\kappa}_{-\infty} \cdot \mathbf{x} + \omega t)]\} \ldots\,, \quad \xi < \xi_-\,, \tag{2.3}$$

and

$$\tilde{p}_I(\mathbf{x},t) = \tilde{p}_{I,\mp\infty}(\mathbf{x},t) = \mathrm{Re}\{p_{I,\mp\infty}\exp[-\beta_{\mp\infty}\xi + i(\boldsymbol{\kappa}_{\mp\infty}\cdot\mathbf{x}+\omega t)]\}\ldots\ , \quad \xi \lesseqgtr \xi_{\mp}\ . \tag{2.4}$$

Here $s_{-\infty}$, $\boldsymbol{\zeta}_{-\infty}$ and $p_{I,\mp\infty}$ are the complex amplitudes of the entropic, vortical and acoustic excitations, ω is the temporal frequency, $\boldsymbol{\kappa}_{\mp\infty}$ is the wave number with $\kappa_{\eta,\mp\infty} = \sigma G^{-1}$, and the $\beta_{\mp\infty}$ are attenuation constants. It follows from the governing equations that the temporal frequency and wave number of an entropic or vortical excitation are related by $\omega = -\boldsymbol{\kappa}_{-\infty}\cdot\mathbf{V}_{-\infty}$, where $\mathbf{V}_{-\infty}$ is the uniform relative inlet velocity, but more complicated relationships exist between ω and $\boldsymbol{\kappa}_{\mp\infty}$ for pressure excitations [17].

As a consequence of the foregoing unsteady aerodynamic linearization, the first-order inviscid flows arising from excitations of the form (2.1) through (2.4) will be harmonic in time, and they will satisfy a blade-to-blade periodicity condition. Therefore, these flows can be determined by solving a time-independent, linear, boundary-value problem, over a single extended blade-passage solution domain, for the complex amplitudes of the linearized unsteady flow variables. Also, because of our assumptions regarding shocks and the steady flow far upstream of the blade row, the steady background flow will be isentropic and irrotational. In this case, closed form solutions can be determined for the unsteady entropic and vortical perturbations. Therefore, numerical field methods are required only for determining the first-order unsteady pressure fluctuations.

3. The Flow in the Inviscid Region

3.1 Unsteady Perturbations of a Potential Mean Flow

For small amplitude unsteady excitations, i.e., $|s_{-\infty}|$, $|\zeta_{-\infty}|$, etc., $\sim \mathcal{O}(\epsilon) << 1$, the time-dependent flow can be regarded as a small perturbation of an underlying nonlinear mean or steady background flow. Thus, for example, we can express the time-dependent velocity in the form

$$\tilde{\mathbf{V}}(\mathbf{x},t) = \mathbf{V}(\mathbf{x}) + \tilde{\mathbf{v}}(\mathbf{x},t) + \dots \ , \tag{3.1}$$

where $\mathbf{V}(\mathbf{x})$ is the local mean velocity and $\tilde{\mathbf{v}}(\mathbf{x},t)$ is the first-order (in ϵ) unsteady velocity. In addition, Taylor series expansions, e.g.,

$$\tilde{\mathbf{V}}_{\mathcal{S}} = (\tilde{\mathbf{V}} + \boldsymbol{\mathcal{R}} \cdot \boldsymbol{\nabla}\tilde{\mathbf{V}} \ + \dots)|_{\mathrm{S}} \ , \tag{3.2}$$

and surface-vector relations, i.e.,

$$\boldsymbol{\tau}_{\mathcal{S}} = \boldsymbol{\tau}_{\mathrm{S}} + \left(\frac{\partial \boldsymbol{\mathcal{R}}}{\partial \tau_{\mathrm{S}}} \cdot \mathbf{n}_{\mathrm{S}}\right) \mathbf{n}_{\mathrm{S}} + \ \dots \quad \text{and} \quad \mathbf{n}_{\mathcal{S}} = \mathbf{n}_{\mathrm{S}} - \left(\frac{\partial \boldsymbol{\mathcal{R}}}{\partial \tau_{\mathrm{S}}} \cdot \mathbf{n}_{\mathrm{S}}\right) \boldsymbol{\tau}_{\mathrm{S}} + \ \dots \tag{3.3}$$

can be applied to refer information at a moving blade, wake or shock surface to the corresponding mean surface. Here $\boldsymbol{\mathcal{R}}(\mathbf{x},t) = \mathbf{x}_{\mathcal{S}} - \mathbf{x}_{\mathrm{S}}$ is the displacement of a point on the moving surface relative to its mean position, the subscripts $\mathcal{S}$ and S refer to the moving and mean surface locations, respectively, and the unit tangent, $\boldsymbol{\tau}$, and normal, $\mathbf{n}$, vectors are oriented such that $\mathbf{n} \times \boldsymbol{\tau}$ points out from the page

The equations that govern the steady and first-order unsteady flow properties are determined by substituting the foregoing expansions into the full time-dependent, nonlinear governing equations, collecting terms of like power in ϵ and neglecting terms of $\mathcal{O}(\epsilon^2)$ or higher. This procedure provides a nonlinear boundary-value problem for a steady background flow and a linear variable-coefficient problem for the first-order unsteady flow in which the coefficients depend on the underlying steady flow. The first-order or linearized unsteady fluctuations caused by a periodic harmonic unsteady excitation will be harmonic in time, e.g.,

$$\tilde{\mathbf{v}}(\mathbf{x},t) = \mathrm{Re}\{\mathbf{v}(\mathbf{x}) \exp(i\omega t)\} \ . \tag{3.4}$$

In addition, the steady and, for an excitation at wave number $\kappa_\eta = \sigma G^{-1}$, the linearized unsteady flow properties will satisfy the following circumferential conditions, e.g.,

$$\mathbf{V}(\mathbf{x} + m\mathbf{G}) = \mathbf{V}(\mathbf{x}) \quad \text{and} \quad \mathbf{v}(\mathbf{x} + m\mathbf{G}) = \mathbf{v}(\mathbf{x}) \exp(im\sigma) \ . \tag{3.5}$$

Thus, solutions to time-independent nonlinear steady and linearized unsteady flow problems are required only over a single extended blade-passage region of the cascade. In addition, since analytic far-field solutions can be determined [17], the numerical solution domain can be restricted further to a single extended blade-passage region of finite extent in the axial direction.

The Steady Background Flow

Because of our assumptions regarding shocks and the flow far upstream of the blade row, the steady background flow is isentropic and irrotational; i.e., $\mathbf{V} = \nabla\Phi$, where Φ is the steady velocity potential. Thus, the field equations that govern this flow are

$$\nabla \cdot (\bar{\rho}\nabla\Phi) = 0 \tag{3.6}$$

and

$$\begin{aligned}(M_{-\infty}V/M)^2 = (M_{-\infty}A)^2 = \bar{\rho}^{\,\gamma-1} = (\gamma M_{-\infty}^2 P)^{(\gamma-1)/\gamma} = (\gamma-1)M_{-\infty}^2 T \\ = 1 - \frac{\gamma-1}{2}M_{-\infty}^2[(\nabla\Phi)^2 - 1] = \frac{2+(\gamma-1)M_{-\infty}^2}{2+(\gamma-1)M^2}\ ,\end{aligned} \tag{3.7}$$

where M, A, $\bar{\rho}$, P and T are the local Mach number, speed of sound propagation, density, pressure and temperature, respectively, in the mean or steady background flow and γ is the specific heat ratio of the fluid. Surface conditions for the zeroth-order or steady flow apply at the mean positions, B_m, W_m and $\mathrm{Sh}_{m,n}$, of the blade, wake and shock surfaces, where the subscript n refers to the nth shock associated with the mth blade. Since, by assumption, the flow remains attached to the blade surfaces, a flow tangency condition applies at such surfaces. In addition, mass and tangential momentum must be conserved across shocks, and the steady pressure and normal velocity component must be continuous across blade wakes.

Numerical procedures for determining two-dimensional steady potential flows through cascades have been developed extensively, e.g., see [3, 18], particularly for flows with subsonic relative inlet and exit Mach numbers (i.e., $M_{\mp\infty} < 1$). In such calculations far-field boundary conditions are imposed at axial stations placed at finite distances upstream and downstream (i.e., at $\xi = \xi_{\mp}$) from the blade row, where linearized solutions describing the behavior of the steady potential can be matched to a nonlinear near-field solution. In addition, a Kutta condition is usually imposed at blade trailing edges in lieu of prescribing an exit freestream property. Finally, the usual practice is to solve the conservative form of the mass-balance equation (3.6) throughout the entire fluid domain. Thus, the shock- and wake-jump conditions are not imposed explicitly. Instead, shock phenomena are captured through the use of special differencing techniques. Wake conditions are satisfied implicitly, because the fluid properties are continuous and differentiable across wakes. If needed, mean shock and wake locations can be determined *a posteriori* from the resulting steady solution.

3.2 Linearized Unsteady Equations

The field equations that govern the first-order unsteady perturbation of an isentropic and irrotational steady flow can be expressed as a system of coupled differential equations for the complex amplitudes of the first-order entropy ($\tilde{s}$), velocity ($\tilde{\mathbf{v}}$) and pressure ($\tilde{p}$), respectively (see [8, 19]). In general, we require a solution to this system subject to prescribed flow conditions far upstream and far downstream from the blade row, the flow tangency condition at moving blade surfaces, and, since the inviscid field equations apply only in continuous regions of the flow, jump conditions at moving shocks and blade wakes.

As indicated by Goldstein [8, 9] the system of field equations that govern the linearized unsteady flow can be recast into a very convenient form by decomposing the unsteady velocity

into rotational ($\mathbf{v}_R$) and irrotational ($\nabla\phi$) parts. Under this decomposition the rotational velocity, $\mathbf{v}_R$, is divergence-free far upstream of the blade row, i.e., $\nabla \cdot \mathbf{v}_R \equiv 0$ for $\xi < \xi_-$, and the unsteady pressure depends only upon the potential ϕ through the relation $p = -\bar{\rho}\bar{D}\phi/Dt$, where $\bar{D}/Dt = i\omega + \nabla\Phi \cdot \nabla$ is a convective derivative operator based on the mean flow velocity. The unsteady vorticity is given by $\boldsymbol{\zeta} = \nabla \times \mathbf{v}_R$. Here we apply a modified form of the Goldstein decomposition, which was introduced by Atassi and Grzedzinski [10], to facilitate the numerical resolution of the velocity potential, i.e., we set

$$\mathbf{v} = \mathbf{v}_* + \nabla\phi = \mathbf{v}_R + \nabla\phi_* + \nabla\phi \,, \tag{3.8}$$

where ϕ_* is a convected or pressure-less potential ($\bar{D}\phi_*/Dt = 0$), which renders $\mathbf{v}_* \cdot \mathbf{n} = (\mathbf{v}_R + \nabla\phi_*) \cdot \mathbf{n} \equiv 0$ at blade and wake mean positions.

With the decomposition (3.8) the system of field equations that governs the unsteady flow variables s, $\mathbf{v}_R$ and ϕ can be written in the form

$$\frac{\bar{D}s}{Dt} = 0 \tag{3.9}$$

$$\frac{\bar{D}}{Dt}(\mathbf{v}_R - s\nabla\Phi/2) + [(\mathbf{v}_R - s\nabla\Phi/2) \cdot \nabla]\nabla\Phi = 0 \tag{3.10}$$

and

$$\frac{\bar{D}}{Dt}(A^{-2}\frac{\bar{D}\phi}{Dt}) - \bar{\rho}^{-1}\nabla \cdot (\bar{\rho}\nabla\phi) = \bar{\rho}^{-1}\nabla \cdot [\bar{\rho}(\mathbf{v}_R + \nabla\phi_*)] = \bar{\rho}^{-1}\nabla \cdot (\bar{\rho}\mathbf{v}_*) \,. \tag{3.11}$$

These equations are coupled only sequentially, i.e., they can be solved in order to determine the complex amplitudes s, $\mathbf{v}_R$ and ϕ. Moreover, since the entropy fluctuation is governed by a convection equation, it can be determined as a solution of Eq. (3.9) in terms of the prescribed upstream entropy field. The rotational velocity fluctuation, $\mathbf{v}_R$, is governed by a modified convection equation and can be determined as a solution of Eq. (3.10) in terms of the prescribed upstream entropy and rotational velocity fields. The velocity potential, ϕ, is governed by a second-order partial differential equation with source term $\bar{\rho}^{-1}\nabla \cdot (\bar{\rho}\mathbf{v}_*)$ and depends, therefore, upon the rotational velocity, the convected potential, and boundary condition information both far upstream and far downstream of the blade row as well as on the blade, wake and shock surfaces.

Far-Field Behavior

We have assumed that the mean or steady flow is at most a small (i.e., of $\mathcal{O}(\epsilon)$) perturbation from a uniform stream both far upstream ($\xi < \xi_-$) and far downstream ($\xi > \xi_+$) from the blade row. Therefore, in these regions, the first-order (in ϵ) unsteady field equations can be reduced to constant coefficient equations for which analytical solutions can be determined (see [17]). For example, it follows after replacing $\nabla\Phi$ by $\mathbf{V}_{-\infty}$ in (3.9) and (3.10) that the complex amplitudes of the entropy and rotational velocity fluctuations far upstream of the blade row are given by

$$s(\mathbf{x}) = s_{-\infty}\exp(i\boldsymbol{\kappa}_{-\infty} \cdot \mathbf{x}), \quad \xi < \xi_- \,, \tag{3.12}$$

and

$$\mathbf{v}_R(\mathbf{x}) = \mathbf{v}_{R,-\infty} \exp(i\boldsymbol{\kappa}_{-\infty} \cdot \mathbf{x}), \quad \xi < \xi_- \ , \tag{3.13}$$

where $s_{-\infty}$ and $\boldsymbol{\zeta}_{-\infty} = (\boldsymbol{\nabla} \times \mathbf{v}_R)_{-\infty} = i\boldsymbol{\kappa}_{-\infty} \times \mathbf{v}_{R,-\infty}$, the complex amplitudes (at $\mathbf{x} = 0$) of the incident entropic and vortical gusts, are prescribed. The circumferential wave number, $\kappa_{\eta,\mp\infty}$, is σ/G and it follows from (3.9) and (3.10) that $\boldsymbol{\kappa} \cdot \mathbf{V}_{-\infty} = -\omega$. Since the rotational velocity is divergence-free far upstream of the blade row, the vectors $\boldsymbol{\kappa}_{-\infty}$ and $\mathbf{v}_{R,-\infty}$ are orthogonal, and therefore,

$$\mathbf{v}_{R,-\infty} = i(\boldsymbol{\kappa}_{-\infty} \times \boldsymbol{\zeta}_{-\infty})/|\boldsymbol{\kappa}_{-\infty}|^2 \ . \tag{3.14}$$

The velocity potential fluctuations in the far upstream and far downstream regions depend upon the acoustic excitation as well as the response of the cascade to the imposed unsteady excitations. We can set

$$\phi(\mathbf{x}) = \phi_E(\mathbf{x}) + \phi_R(\mathbf{x}) \quad \text{for } \xi \lesseqgtr \xi_\mp \ , \tag{3.15}$$

where the potential component ϕ_E accounts for acoustic excitations, i.e., pressure disturbances that either attenuate as they approach the blade row or propagate and carry energy towards the blade row. In particular, it follows from (3.11) with $\boldsymbol{\nabla}\Phi = \mathbf{V}_{\mp\infty}$ that for an acoustic excitation at temporal frequency ω,

$$\phi_E(\mathbf{x}) = \phi_{I,\mp\infty} \exp[\beta_{\mp\infty}\xi + i\boldsymbol{\kappa}_{\mp\infty} \cdot \mathbf{x}], \quad \xi \lesseqgtr \xi_\mp \ , \tag{3.16}$$

where

$$\phi_{I,\mp\infty} = \bar{\rho}^{-1}_{\mp\infty}\{\beta_{\mp\infty}V_{\mp\infty}\cos\Omega_{\mp\infty} - i[\omega + (\boldsymbol{\kappa}_{\mp\infty} \cdot \mathbf{V}_{\mp\infty})]\}^{-1} p_{I,\mp\infty} \ , \tag{3.17}$$

the complex amplitudes $p_{I,\mp\infty}$ are prescribed, $\kappa_{\eta,\mp\infty} = \sigma/G$, and $\beta_{\mp\infty}$ and $\kappa_{\xi,\mp\infty}$ depend upon the inlet/exit freestream conditions, and the temporal frequency (ω) and interblade phase angle (σ) of the acoustic excitation. The potential component ϕ_R is associated with the acoustic and vortical response of the blade row and therefore, must be determined as part of the unsteady solution.

3.3 Entropy and Rotational Velocity

Closed form solutions for the linearized entropy and rotational velocity fluctuations can be determined in terms of independent variables that describe the steady background flow [8, 12]. For this purpose we introduce the Lagrangian coordinate vector

$$\mathbf{X} = \Delta\mathbf{e}_T + \Psi\mathbf{e}_N \ . \tag{3.18}$$

Here,

$$\Delta(\mathbf{x}) = \mathbf{x}_- + \int_{\mathbf{x}_- + [\Psi(\mathbf{x}) - \Psi(\mathbf{x}_-)]\mathbf{e}_N}^{\mathbf{x}} V^{-1} d\tau_\Psi \ , \tag{3.19}$$

and

$$\Psi(\mathbf{x}) = \mathbf{x}_- + \int_{\mathbf{x}_- + \mathbf{e}_N}^{\mathbf{x}} \bar{\rho}(\mathbf{e}_z \times \mathbf{V}) \cdot d\boldsymbol{\tau} \tag{3.20}$$

are the drift and stream functions, respectively, of the steady background flow. Also, the unit vectors $\mathbf{e}_T$, $\mathbf{e}_N (= \mathbf{e}_z \times \mathbf{e}_T)$ and $\mathbf{e}_z$ point in the inlet freestream direction, normal to

the inlet freestream direction, and out from the page, respectively, $\mathbf{x}_-$ is the position vector to the point of intersection (ξ_-, η_-) of the reference blade stagnation streamline and the axial line $\xi = \xi_-$, $d\tau_\Psi$ is a differential element of arc length along a streamline, and $d\boldsymbol{\tau}$ is a differential vector tangent to the path of integration.

Note that $\bar{D}\mathbf{X}/Dt = (\mathbf{V}\cdot\boldsymbol{\nabla})\mathbf{X} = \mathbf{V}_{-\infty} = \mathbf{e}_T$ and $\mathbf{X} \to \mathbf{x}$, as $\xi \to -\infty$. Thus, the solution to the entropy transport equation (3.9), which satisfies the upstream condition (3.12), is

$$s(\mathbf{x}) = s_{-\infty}\exp(i\boldsymbol{\kappa}_{-\infty}\cdot\mathbf{X}) \ , \tag{3.21}$$

and the solution to the rotational velocity transport equation (3.10) , which satisfies the condition (3.13), is

$$\mathbf{v}_R(\mathbf{x}) = [\boldsymbol{\nabla}(\mathbf{X}\cdot\boldsymbol{\mathcal{A}}_{-\infty}) + s_{-\infty}\boldsymbol{\nabla}\Phi/2]\exp(i\boldsymbol{\kappa}_{-\infty}\cdot\mathbf{X}) \ , \tag{3.22}$$

where

$$\boldsymbol{\mathcal{A}}_{-\infty} = \mathbf{v}_{R,-\infty} - s_{-\infty}\mathbf{V}_{-\infty}/2 \ . \tag{3.23}$$

The complex amplitude of the unsteady vorticity is

$$\boldsymbol{\zeta} = \boldsymbol{\nabla}\times\mathbf{v}_R = \boldsymbol{\nabla}(i\boldsymbol{\kappa}_{-\infty}\cdot\mathbf{X})\times[\boldsymbol{\nabla}(\boldsymbol{\mathcal{A}}_{-\infty}\cdot\mathbf{X}) + s_{-\infty}\boldsymbol{\nabla}\Phi/2]\exp(i\boldsymbol{\kappa}_{-\infty}\cdot\mathbf{X}) \ , \tag{3.24}$$

and $\boldsymbol{\zeta} \to \boldsymbol{\zeta}_{-\infty} = i\boldsymbol{\kappa}\times\mathbf{v}_{R,-\infty}$ as $\mathbf{X} \to \mathbf{x}$.

If the steady background flow stagnates at blade leading edges, as it will for realistic configurations, the drift function will have a logarithmic singularity at the mean blade and wake surfaces, i.e., $\Delta \to a_0 \ln n$ as $n \to 0$, where n is the normal distance from the surface and a_0 is a real constant. As a result, the exponential function $\exp(i\boldsymbol{\kappa}_{-\infty}\cdot\mathbf{X})$ will be indeterminate, and the normal component of the rotational velocity will be singular, i.e., $\mathbf{v}_R\cdot\mathbf{n} \to a_1 n^{-1}\exp(i\boldsymbol{\kappa}_{-\infty}\cdot\mathbf{X})$, where a_1 is a complex constant, at such surfaces. We can remove this singular behavior from the blade and wake surface conditions that determine the unsteady potential, ϕ, by prescribing a convected potential of the form [10]

$$\phi_* = \left[-i\omega^{-1}\boldsymbol{\mathcal{A}}_{-\infty}\cdot\mathbf{V}_{-\infty} + F(\Psi)\right]\exp(i\boldsymbol{\kappa}_{-\infty}\cdot\mathbf{X}) \ , \tag{3.25}$$

where

$$F(\Psi) = \frac{\omega^{-1}(\boldsymbol{\kappa}_{-\infty}\times\boldsymbol{\mathcal{A}}_{-\infty})\cdot\mathbf{e}_z G\cos\Omega_{-\infty}}{2\pi(1-ia_0\omega)}\sin\left[\frac{2\pi[\Psi(\mathbf{x})-\Psi(\mathbf{x}_-)]}{G\cos\Omega_{-\infty}}\right] \tag{3.26}$$

is a complex function that depends upon, among other things, the behavior of the mean flow in the vicinity of a leading-edge stagnation point. This choice of ϕ_* ensures that $\mathbf{v}_*\cdot\mathbf{n} = (\mathbf{v}_R + \boldsymbol{\nabla}\phi_*)\cdot\mathbf{n} = 0$ at blade and wake mean positions.

After combining (3.22), (3.25) and (3.26), we find that the complex amplitude of the source-term velocity, $\mathbf{v}_* = \mathbf{v}_R + \boldsymbol{\nabla}\phi_*$, is given by

$$\mathbf{v}_* = \left[F\boldsymbol{\nabla}(i\boldsymbol{\kappa}_{-\infty}\cdot\mathbf{X}) + \left(\frac{dF}{d\Psi} - \omega^{-1}(\boldsymbol{\kappa}_{-\infty}\times\boldsymbol{\mathcal{A}}_{-\infty})\cdot\mathbf{e}_z\right)\boldsymbol{\nabla}\Psi + s_{-\infty}\boldsymbol{\nabla}\Phi/2\right]\exp(i\boldsymbol{\kappa}_{-\infty}\cdot\mathbf{X}) \ . \tag{3.27}$$

Note that $\mathbf{v}_*$ behaves like $s_{-\infty}\boldsymbol{\nabla}\Phi\exp(i\boldsymbol{\kappa}_{-\infty}\cdot\mathbf{X})/2$ in the immediate vicinity of the mean blade and wake surfaces, i.e., as $n \to 0$. Thus, $\mathbf{v}_*\cdot\mathbf{n} = 0$, but, if $s_{-\infty} \neq 0$, the tangential component of the source-term velocity will be indeterminate at such surfaces.

The velocities $\mathbf{v}_R$ and $\mathbf{v}_*$ depend upon Δ and Ψ and the first partial derivative of these functions. Therefore, the complex amplitudes of the unsteady vorticity, $\boldsymbol{\zeta} = \boldsymbol{\nabla} \times \mathbf{v}_R = \boldsymbol{\nabla} \times \mathbf{v}_*$, and the source term, $\bar{\rho}^{-1} \boldsymbol{\nabla} \cdot (\bar{\rho} \mathbf{v}_*)$, in (3.11) depend also upon the second partial derivatives of Δ and Ψ. Thus, an accurate solution for the nonlinear steady background flow is critical for determining the unsteady effects associated with entropic and vortical excitations.

Numerical Evaluation

The complex amplitudes of the entropy, rotational velocity, vorticity, and source term velocity are readily determined once the values of the drift and stream functions and their spatial derivatives are specified over the single extended blade-passage solution domain. For this purpose it is convenient to use an H-grid in which one set of mesh lines are the streamlines of the steady background flow. An H- grid which covers the solution domain, i.e., which is bounded by the upstream and downstream axial lines $\xi = \xi_{\mp}$ and two neighboring mean-flow stagnation streamlines, is appropriate. The locations of the latter are determined *a posteriori* from the solution for the nonlinear steady background flow. Once the boundaries of the H-grid established, the locations of the interior grid points can be determined using an elliptic grid generation technique as described in Ref. [12].

Because a streamline mesh is used, the drift function can be evaluated at each point in the computational domain by a straightforward numerical integration of Eq. (3.19). The procedure used in Ref. [12] is simply to specify the drift function along the far upstream boundary $\xi = \xi_-$, and then to evaluate this function along each streamline using a second-order accurate difference approximation. The derivatives of the drift and stream functions at a given grid point are determined using the finite difference operators developed by Caspar and Verdon [20]. Because the drift function is singular at blade and wake surfaces, one-sided difference approximations are used to evaluate the derivatives of this function at points on the mesh streamlines adjacent to these surfaces.

3.4 Velocity Potential

The unsteady potential (ϕ) is determined as a solution of the field equation (3.11) subject to conditions at the mean blade and wake surfaces and in the far field. Flow tangency applies at the blade surfaces, $\mathcal{B}_m$, the fluid pressure and normal velocity must be continuous across blade wakes, $\mathcal{W}_m$, and mass and tangential momentum must be conserved across shocks, $\mathcal{S}h_{m,n}$. As a consequence of the small unsteady-disturbance approximation, the conditions on the linearized unsteady perturbation at the moving blade, shock and wake surfaces can be imposed at the mean positions of these surfaces (see Ref. [19]), with the mean wake (W_m), i.e., the downstream stagnation streamlines, and shock ($\mathrm{Sh}_{m,n}$) locations being determined from the nonlinear steady solution. Thus, the flow tangency condition can be written as

$$\mathbf{v} \cdot \mathbf{n} = \boldsymbol{\nabla}\phi \cdot \mathbf{n} = [i\omega \mathbf{r} + (\boldsymbol{\nabla}\Phi \cdot \boldsymbol{\tau})(\boldsymbol{\tau} \cdot \boldsymbol{\nabla})\mathbf{r} - (\mathbf{r} \cdot \boldsymbol{\nabla})\boldsymbol{\nabla}\Phi] \cdot \mathbf{n}, \quad \mathbf{x} \in B_m \tag{3.28}$$

In addition, since the irrotational steady velocity and pressure are continuous and have continuous derivatives across the mean-flow downstream stagnation streamlines, the wake conditions reduce to

$$[\![p]\!] = [\![\bar{D}\phi/Dt]\!] = 0 \quad \text{and} \quad [\![\mathbf{v} \cdot \mathbf{n}]\!] = [\![\boldsymbol{\nabla}\phi]\!] \cdot \mathbf{n} = 0, \quad \mathbf{x} \in W_m \,, \tag{3.29}$$

where the symbol $[\![\ ]\!]$ indicates the jump or change in a quantity at a surface at which the flow variables are discontinuous. Finally, if we neglect changes in entropy and rotational velocity across shocks, the conservation laws for mass and tangential momentum yield the following linearized shock-jump condition for a shock that terminates in the fluid

$$\begin{aligned}[\![\bar{\rho}(\nabla\phi + \mathbf{v}_R - A^{-2}\frac{\bar{D}\phi}{Dt}\nabla\Phi)]\!]\cdot\mathbf{n} = -[\![\bar{\rho}]\!][i\omega + (\nabla\Phi\cdot\boldsymbol{\tau})\boldsymbol{\tau}\cdot\nabla][([\![\nabla\Phi]\!]\cdot\mathbf{n})^{-1}[\![\phi]\!]\,] \\ -(\nabla\Phi\cdot\mathbf{n})^{-1}[\![\phi]\!]\,\boldsymbol{\tau}\cdot\nabla([\![\bar{\rho}]\!]\nabla\Phi\cdot\boldsymbol{\tau})\,,\quad \mathbf{x}\in \mathrm{Sh}_{m,n}\,.\end{aligned} \tag{3.30}$$

Equation (3.30) provides a relation for determining the jump in the unsteady potential, $[\![\phi]\!]$, at the mean position of a shock. The shock displacement normal to the mean shock locus is then given by $\mathbf{r}_{\mathrm{Sh}}\cdot\mathbf{n} = -([\![\nabla\Phi]\!]\cdot\mathbf{n})^{-1}[\![\phi]\!]$.

The velocity potential in the far field is given by (3.15); the potential due to an acoustic excitation at frequency ω and circumferential wave number $\kappa_{\eta,\mp\infty} = \sigma/G$, by (3.16). Usually only acoustic excitations that are of propagating type are considered. For subsonic inlet and exit conditions ($M_{\mp\infty} < 1$) the velocity potential corresponding to a propagating acoustic excitation at temporal frequency $\omega > 0$ has the form (3.16) with $\beta_{\mp\infty} = 0$, and

$$\kappa^{(-)}_{\eta,\mp\infty} \le \kappa_{\eta,\mp\infty} = \sigma G^{-1} \le \kappa^{(+)}_{\eta,\mp\infty}\,, \tag{3.31}$$

where the circumferential wave numbers at which cut-off occurs, $\kappa^{(\mp)}_{\eta,\mp\infty}$, are given by

$$\kappa^{(\mp)}_{\eta,\mp\infty} = \omega V^{-1}_{\mp\infty} M_{\mp\infty}(1-M^2_{\mp\infty})^{-1}(M_{\mp\infty}\sin\Omega_{\mp\infty} \pm \sqrt{1-M^2_{\mp\infty}\cos^2\Omega_{\mp\infty}})\,. \tag{3.32}$$

The axial wave number of the propagating acoustic excitation is

$$\kappa_{\xi,\mp\infty} = i(\mp|d_{\mp\infty}| + M^2_{\mp\infty}\delta_{\mp\infty}\cos\Omega_{\mp\infty})\,, \tag{3.33}$$

where

$$|d_{\mp\infty}| = |(1-M_{\mp\infty}\cos^2\Omega_{\mp\infty})^{-1}\kappa^2_\eta - M^2_{\mp\infty}\delta^2_{\mp\infty}|^{1/2}\,, \tag{3.34}$$

and

$$\delta_{\mp\infty} = (\omega V^{-1}_{\mp\infty} + \kappa_\eta\sin\Omega_{\mp\infty})/(1-M^2_{\mp\infty}\cos^2\Omega_{\mp\infty})\,. \tag{3.35}$$

Analytic solutions to (3.11), with $\nabla\Phi = \mathbf{V}_{\mp\infty}$, for the far-field potential component ϕ_R which satisfy the requirements that acoustic response disturbances either attenuate with increasing axial distance from the blade row or propagate carrying energy away from or parallel to the blade row, and that vorticity must be convected downstream are given in Ref. [17]. These solutions contain arbitrary constants that are determined by matching the far-field analytic solutions for the velocity potential to near field numerical solutions.

Numerical Evaluation

A numerical resolution of the foregoing linear, variable-coefficient, boundary-value problem for ϕ is required over a single, extended, blade-passage region of finite extent. The field equation, Eq. (3.11), must be solved in continuous regions of the flow subject to surface conditions, Eqs. (3.28–3.30), at the mean blade, wake and shock surfaces. In addition, the

near-field numerical solution for the potential must be matched to far-field analytical solutions at finite distances ($\xi = \xi_{\mp}$) upstream and downstream from the blade row. Numerical methods for determining ϕ for subsonic and transonic flows have been reported in Refs. [2], [11], [20] and [21]. To date, transonic solutions have been determined only for flows in which only a single normal shock occurs in each blade passage and for unsteady flows in which $s \equiv \zeta \equiv 0$. Thus, numerical solution procedures, see [12] and [16], for the entropic and vortical gust problems have only been developed and implemented for subsonic flows. The development of such procedures for the transonic gust response problem remains, therefore, as a subject for future research.

Because of the stringent and conflicting requirements placed on computational meshes for cascade flows, a composite-mesh, which is constructed by overlaying a polar-type local mesh and an H-type cascade mesh, has been adopted for determining the unsteady potential. The H mesh is used to resolve unsteady phenomena over the entire solution domain; the local surface-fitted mesh, to resolve phenomena in the vicinities of a rounded blade leading edge and/or a shock. The cascade mesh facilitates the imposition of the cascade periodicity conditions (3.5) and the matching of the analytic and numerical unsteady solutions at the far upstream ($\xi = \xi_-$) and far downstream ($\xi = \xi_+$) boundaries. Use of this mesh alone is often sufficient for resolving unsteady subsonic flows. The local mesh allows an accurate modeling of unsteady leading-edge and shock phenomena. It is constructed so that two "radial" lines coincide with the predicted mean shock locus to provide upstream and downstream shock mesh lines for the accurate imposition of shock-jump conditions.

Since the cascade and local body-fitted meshes differ topologically, a zonal solution procedure for overlapping meshes has been adopted in Ref. [11] for determining the unsteady potential. In the region of intersection between the two meshes, i.e., the region covered by the local mesh, certain cascade mesh points are eliminated depending upon their location within the local mesh domain. The discrete equations are written separately for the cascade and local meshes and coupled implicitly through special interface conditions, resulting in a single composite system of finite-difference equations that describe the unsteady flow over the entire solution domain.

The finite-difference model used to approximate the unsteady equations on the cascade and local meshes has been described in detail in Ref. [20]. Algebraic approximations to the various linear operators, which make up the unsteady boundary-value problem, are obtained using an implicit, least-squares, interpolation procedure that is applicable on arbitrary grids. This procedure employs a nine point "centered" difference star at subsonic field points, and a twelve point difference star at supersonic points. At a blade boundary point a nine point one-sided difference star is used on the cascade mesh, while nine- or six-point one-sided stars are used on the local mesh. Shocks are fitted in the local-mesh calculation by approximating the shock-jump condition (3.30) using one-sided difference expressions to evaluate the normal derivatives of the unsteady potential on the upstream (supersonic) and downstream (subsonic) sides of the shock. At those points along the shock mesh lines at which the steady flow is continuous (i.e., at points lying beyond the end of the shock), the condition $[\![\phi]\!] = 0$ is imposed.

The systems of linear algebraic equations that approximate the unsteady boundary-value problem on the cascade and local meshes are block-tridiagonal for subsonic flow and block-pentadiagonal for transonic flow. A subsonic solution on the H-mesh alone is determined

using a direct block inversion scheme. Composite (cascade/local) mesh subsonic or transonic solutions are determined using a different scheme. Because of the cascade/local mesh coupling conditions, the composite system of discrete equations contains a sparse coefficient matrix of large band width. Consequently, special storage and inversion techniques must be applied to achieve an efficient solution. Once the composite system of unsteady equations is cast into an appropriate format, it can be solved using Gaussian elimination [11].

3.5 The Inviscid Response

At this point we have presented a linearized unsteady aerodynamic formulation that describes the general first-order fluid-dynamic perturbation of an isentropic and irrotational subsonic or discontinuous transonic steady background flow. We have also outlined the numerical procedures used to evaluate the unsteady entropy, rotational velocity and velocity potential. Solutions to the linearized unsteady problem are required to determine the aerodynamic response information needed for aeroacoustic and aeroelastic predictions, i.e., the unsteady pressure field and the unsteady pressures acting at the moving blade surfaces. In particular, we refer the reader to Refs. [7, 22] for a description of the various local and global unsteady aerodynamic response parameters that are used in aeroelastic investigations.

Approximate solutions for the full time-dependent flow properties are constructed by superposing the results for the steady and the unsteady flow properties, e.g.,

$$\tilde{P}(\mathbf{x},t) = P(\mathbf{x}) + \tilde{p}(\mathbf{x},t) + \sum \tilde{P}_{\mathcal{S}h_{m,n}}(\mathbf{x},t) + \dots \,, \tag{3.36}$$

where $\tilde{p}(\mathbf{x}) = \mathrm{Re}\{p(\mathbf{x})\exp(i\omega t)\}$. The first two terms on the right-hand-side of Eq. (3.36) account for the steady and the first-harmonic contributions to the time-dependent fluid pressure acting at the point $\mathbf{x}$. The third term accounts for the anharmonic contribution to the time-dependent pressure caused by the motions of shocks, and is determined by analytically continuing the steady solution from the mean to the instantaneous shock locations [22, 23]. Thus, the first-order anharmonic response depends on the steady values of the fluid properties and the unsteady shock displacements normal to the mean shock loci, $(\mathcal{R}\cdot\mathbf{n})_{\mathrm{Sh}_{m,n}}$. The regions of anharmonicity are confined to thin strips containing the mean shock loci.

The steady background flow is described by the velocity potential, Φ, which is determined in terms of a prescribed inlet Mach number ($M_{-\infty}$), flow angle ($\Omega_{-\infty}$), and cascade geometry. The steady velocity, $\mathbf{V} = \boldsymbol{\nabla}\Phi$, is determined from this potential, as are the steady values of the thermodynamic properties of the fluid [cf. (3.7)]. The total enthalpy, $H = T + V^2/2$, of the steady background flow is constant and is given by

$$H = H_{-\infty} = (\gamma-1)^{-1}M_{-\infty}^{-2} + \frac{1}{2} \tag{3.37}$$

The linearized unsteady flow is described by the dependent variables $\tilde{s}$, $\tilde{\mathbf{v}}_*$, $\tilde{\phi}$ and $\mathcal{R}_{\mathrm{Sh}}\cdot\mathbf{n}$, which are determined in terms of prescribed values of the frequency (ω), interblade phase angle (σ), and the complex amplitudes, $\mathbf{r}_{\mathrm{B}}$, $s_{-\infty}$, $\zeta_{-\infty}$ and $p_{I,\mathcal{F}\infty}$, of the imposed unsteady excitation. The first-harmonic unsteady velocity is $\tilde{\mathbf{v}} = \tilde{\mathbf{v}}_* + \boldsymbol{\nabla}\tilde{\phi}$, and the first-harmonic thermodynamic properties of the fluid can be determined in terms of the independent variables $\tilde{s}$ and $\tilde{\phi}$.

It follows from the equation of state for a perfect gas and the fundamental thermodynamic identity relating entropy, pressure and density that

$$\tilde{p} = \gamma^{-1}(\gamma - 1)(\bar{\rho}\tilde{t} + \tilde{\rho}T) \ , \tag{3.38}$$

and

$$\tilde{s} = \gamma^{-1}\tilde{p}/P - \tilde{\rho}/\bar{\rho} \ , \tag{3.39}$$

respectively, where $\tilde{t}$ is the linearized unsteady component of the fluid temperature. After combining (3.38) and (3.39) and recalling that $\tilde{p} = -\bar{\rho}\bar{D}\tilde{\phi}/Dt = -\bar{\rho}(\partial/\partial t + \boldsymbol{\nabla}\Phi \cdot \boldsymbol{\nabla})\tilde{\phi}$, we find that the first-harmonic flow properties are related by

$$\tilde{\rho}/\bar{\rho} + \tilde{s} = \gamma^{-1}\tilde{p}/P = (\gamma - 1)^{-1}(\tilde{t}/T - \tilde{s}) = -A^{-2}\bar{D}\tilde{\phi}/Dt \ . \tag{3.40}$$

The first-harmonic total enthalpy $\tilde{h}$, is given by

$$\tilde{h} = T\tilde{s} \quad \mathcal{L}\tilde{\phi}/Dt + \boldsymbol{\nabla}\Phi \cdot [\tilde{\mathbf{v}}_* + \boldsymbol{\nabla}\tilde{\phi}] + \ \ldots \ . \tag{3.41}$$

The Inviscid Flow Along Moving Blade and Wake Surfaces

The values of the inviscid flow quantities along the moving blade and wake surfaces must be available to perform an analysis of the unsteady flows in the viscous layers. These can be determined in terms of their values at the mean surface locations and the blade and wake displacements via Taylor series expansions, e.g.,

$$\tilde{P}_{\mathcal{S}} = P_{\mathrm{S}} + \tilde{p}_{\mathrm{S}} + \boldsymbol{\mathcal{R}} \cdot \boldsymbol{\nabla}P|_{\mathrm{S}} + \sum \tilde{P}_{\mathcal{S}h_n} + \ \ldots \ , \tag{3.42}$$

where $\boldsymbol{\mathcal{R}}$ is the surface displacement vector. In addition, relations between the unit tangent and normal vectors at the instantaneous and mean surface positions, cf. (3.3), are needed to determine the velocity components at the moving surface from information available at the mean surface. Here, the subscript $\mathcal{S}$ refers to points $\mathbf{x}_{\mathcal{S}} = \mathbf{x}_{\mathrm{S}} + \boldsymbol{\mathcal{R}}_{\mathrm{S}}$ on the moving surface, and S, to the points $\mathbf{x}_{\mathrm{S}}$ on the mean surface.

If we now restrict our consideration to continuous, i.e., shock-free steady background flows, the unsteady velocity at a moving blade or wake surface is given by

$$\begin{aligned} \tilde{\mathbf{V}}_{\mathcal{S}} &= [\mathbf{V} + \tilde{\mathbf{v}} + (\boldsymbol{\mathcal{R}} \cdot \boldsymbol{\nabla})\mathbf{V}]_{\mathrm{S}} + \ \ldots \\ &= [\boldsymbol{\nabla}\Phi + \tilde{\mathbf{v}}_* + \boldsymbol{\nabla}\tilde{\phi} + (\boldsymbol{\mathcal{R}} \cdot \boldsymbol{\nabla})\boldsymbol{\nabla}\Phi]_{\mathrm{S}} + \ \ldots \end{aligned} \tag{3.43}$$

Expressions for the tangential and normal components of the fluid velocity at a moving blade and wake surface follow from (3.3), (3.43) and the conditions $\boldsymbol{\nabla}\Phi \cdot \mathbf{n}_{\mathrm{S}} = 0$ and $\tilde{\mathbf{v}}_* \cdot \mathbf{n}_{\mathrm{S}} = 0$. We find that

$$\tilde{\mathbf{V}}_{\mathcal{S}} \cdot \boldsymbol{\tau}_{\mathcal{S}} = [\boldsymbol{\nabla}\Phi + \tilde{\mathbf{v}}_* + \boldsymbol{\nabla}\tilde{\phi} + (\boldsymbol{\mathcal{R}} \cdot \boldsymbol{\nabla})\boldsymbol{\nabla}\Phi]_{\mathrm{S}} \cdot \boldsymbol{\tau}_{\mathrm{S}} + \ \ldots \tag{3.44}$$

and

$$\tilde{\mathbf{V}}_{\mathcal{S}} \cdot \mathbf{n}_{\mathcal{S}} = [\boldsymbol{\nabla}\tilde{\phi} + (\boldsymbol{\mathcal{R}} \cdot \boldsymbol{\nabla})\boldsymbol{\nabla}\Phi]_{\mathrm{S}} \cdot \mathbf{n}_{\mathrm{S}} + \ \ldots \ = \frac{\partial \boldsymbol{\mathcal{R}}}{\partial t} \cdot \mathbf{n}_{\mathrm{S}} \ . \tag{3.45}$$

The thermodynamic properties at the moving blade and wake surfaces are determined using Taylor series expansions along with the thermodynamic property relations for the

steady (3.7) and linearized unsteady (3.40) flows. After performing the necessary algebra, we find that for shock-free flows

$$\frac{\tilde{\rho}_S}{\bar{\rho}_S} + \tilde{s}_S = \frac{\gamma^{-1}\tilde{p}_S}{P_S} = (\gamma-1)^{-1}\left(\frac{\tilde{t}_S}{T_S} - \tilde{s}_S\right) = -A_S^{-2}\left(\frac{\bar{D}\tilde{\phi}}{Dt} + \boldsymbol{\mathcal{R}}\cdot\boldsymbol{\nabla}[(\boldsymbol{\nabla}\Phi)^2/2]\right)_S + \ldots . \quad (3.46)$$

Finally, the total enthalpy of the fluid at a moving blade or wake surface is given by

$$\tilde{H}_S = [H + \tilde{h} + \boldsymbol{\mathcal{R}}\cdot\boldsymbol{\nabla}\dot{H}]_S + \ \ldots \ . \quad (3.47)$$

Since the total enthalpy is constant in the steady background flow, i.e., $H = H_{-\infty}$, and $[\boldsymbol{\nabla}\Phi\cdot\tilde{\mathbf{v}}_*]_S = \tilde{s}(\boldsymbol{\nabla}\Phi\cdot\boldsymbol{\tau})^2/2$ at blade and wake mean positions, we can write

$$\begin{aligned}\tilde{H}_S &= H_{-\infty} + T_S\tilde{s}_S - [\bar{D}\tilde{\phi}/Dt]_S + \boldsymbol{\nabla}\Phi\cdot(\boldsymbol{\nabla}\tilde{\phi} + \tilde{\mathbf{v}}_*)_S + \ \cdots \\ &= [H_{-\infty}(1+\tilde{s}) - \bar{D}\tilde{\phi}/Dt + \boldsymbol{\nabla}\Phi\cdot\boldsymbol{\nabla}\tilde{\phi}]_S + \ldots .\end{aligned} \quad (3.48)$$

Expressions for the anharmonic values of the time-dependent flow properties in the field and at moving blade and wake surfaces can be readily determined following the methods of Refs. [22] and [23]. However, in the present effort only subsonic inviscid and viscous-layer flows will be calculated, and therefore, only the steady and first-harmonic values of the time-dependent inviscid flow properties will be required.

4. The Flow in the Viscous Layer

4.1 Governing Equations

The viscous region consists of thin boundary layers that lie along the upper and lower surfaces of each blade and thin wakes which extend downstream from the blade trailing edges, as indicated in Figure 3. We assume the blade motions to be of sufficiently small amplitude, i.e., on the order of the viscous-layer displacement thickness ($\tilde{\bar{\delta}}$), that the system of field equations that governs the flow in a viscous layer is invariant under a transformation from space- to blade-fixed coordinates. Thus, in terms of the blade-fixed τ, n coordinates we can write

$$\frac{\partial \tilde{\rho}}{\partial t} + \frac{\partial(\tilde{\rho}\tilde{U})}{\partial \tau} + \frac{\partial(\tilde{\rho}\tilde{V})}{\partial n} = 0 \,, \tag{4.1}$$

$$\tilde{\bar{\rho}}\frac{\tilde{D}\tilde{U}}{Dt} = -\frac{\partial \tilde{P}}{\partial \tau} + (\mathrm{Re})^{-1}\frac{\partial}{\partial n}\left(\tilde{\bar{\mu}}\frac{\partial \tilde{U}}{\partial n} - \tilde{\bar{\rho}}\overline{u'v'}\right) \tag{4.2}$$

and

$$\tilde{\bar{\rho}}\frac{\tilde{D}\tilde{H}}{Dt} = \frac{\partial \tilde{P}}{\partial t} + (\mathrm{Re})^{-1}\frac{\partial}{\partial n}\left[\tilde{\bar{\mu}}\left(1-(Pr)^{-1}\right)\tilde{U}\frac{\partial \tilde{U}}{\partial n} + \frac{\tilde{\bar{\mu}}}{Pr}\frac{\partial \tilde{H}}{\partial n} - \tilde{\bar{\rho}}\overline{h'v'}\right] \,. \tag{4.3}$$

Here, $\tilde{U}$ and $\tilde{V}$ are the velocity components, relative to the blade-fixed frame, in the positive τ- and n-directions, respectively, and $\tilde{\bar{\mu}}$ is the molecular viscosity of the fluid. The terms that account for the acceleration of the blade-fixed frame are assumed to be small and have therefore been neglected in reducing the Navier-Stokes equations to viscous-layer equations.

In equations (4.1)–(4.3) the coordinates τ and n measure distances along and normal to, respectively, a blade surface or a reference wake streamline, and $\tilde{D}/Dt \equiv \partial/\partial t + \tilde{\mathbf{V}} \cdot \boldsymbol{\nabla}$ is the convective derivative operator in the blade-fixed frame. The reference wake streamline emanates from a blade trailing edge and is entirely contained within the viscous wake. A distinction should be made between the independent variables that describe the flows in the upper and lower surface boundary layers and in the wakes, e.g., by attaching subscripts to τ and n. However, as a convenience, we are neglecting to make this distinction explicitly.

The symbols $\tilde{\bar{\rho}}$, $\tilde{U}$, $\tilde{V}$, $\tilde{P}$, $\tilde{H}$, and $\tilde{\bar{\mu}}$ in Eqs. (4.1)—(4.3) refer to ensemble (or Reynolds) averaged values of the fluid dynamic variables; u', v' and h' are the values associated with random turbulent fluctuations, and the overbar indicates a turbulent correlation, which must be determined empirically. As a consequence of the high Re and small-amplitude approximations, the pressure in the thin viscous layer is a function only of τ and t, and $\tilde{H} = \tilde{T} + \tilde{U}^2/2$. Since the interaction between the flows in the viscous layer and the external inviscid stream is assumed to be weak, the pressure and the flow properties at the edge of the viscous layer are determined by the inviscid values of these variables at the blade and wake surfaces.

In addition to the foregoing conservation equations, the equation of state for a perfect gas, i.e.,

$$\tilde{P} = \frac{\gamma - 1}{\gamma}\tilde{\bar{\rho}}\tilde{T} \,, \tag{4.4}$$

a law relating the molecular viscosity to the temperature, e.g.,

$$\frac{\tilde{\bar{\mu}}}{\bar{\mu}_{-\infty}} = \left(\frac{\tilde{T}}{T_{-\infty}}\right)^{3/2} \frac{T_{-\infty} + T_C}{\tilde{T} + T_C} , \tag{4.5}$$

and equations relating the turbulent correlations $\overline{u'v'}$ and $\overline{h'v'}$ to the ensemble-averaged flow quantities, i.e.,

$$\tilde{\bar{\rho}}\overline{u'v'} = -\epsilon\frac{\partial \tilde{U}}{\partial n} \quad \text{and} \quad \tilde{\bar{\rho}}\overline{h'v'} = -\epsilon_{\tilde{H}}\frac{\partial \tilde{H}}{\partial n} = \frac{\epsilon}{Pr_T}\frac{\partial \tilde{H}}{\partial n} , \tag{4.6}$$

are also required. Equation (4.5) is a form of Sutherland's Law. Here $\bar{\mu}_{-\infty}$ is the molecular viscosity at the temperature $T_{-\infty}$ and T_C is a constant, which for air has a dimensional value of 110°K [24]. The turbulent correlations $\overline{u'v'}$ and $\overline{h'v'}$ have been related to mean flow gradients, using Prandtl's mixing-length hypothesis. Here ϵ and $\epsilon_{\tilde{H}}$ are the eddy viscosity and eddy diffusivity, respectively, and play roles similar to their molecular counterparts. The eddy diffusivity is related to the molecular diffusivity through the introduction of the turbulent Prandtl number, Pr_T.

Initial and Boundary Conditions

The foregoing system of field equations is parabolic in time and in the streamwise direction. Therefore, the streamwise component of the velocity and the total enthalpy must be known for all time at some upstream streamwise location, and these variables, along with the normal velocity, must be known throughout the solution domain at some initial time. Also, conditions on the fluid properties at the edge(s) of the viscous layer, i.e.,

$$\tilde{U} \to \tilde{U}_e(\tau, t) \quad \text{and} \quad \tilde{H} \to \tilde{H}_e(\tau, t) \quad \text{for} \quad n \to \pm\infty , \tag{4.7}$$

where the limits $+\infty$ and $-\infty$ refer to the edges of the upper (+) and lower (−) surface boundary layers and the upper and lower edges of a wake, a no-slip condition and either a prescribed temperature or heat flux condition at a solid blade surface, i.e.,

$$\tilde{U} = \tilde{V} = 0 \quad \text{and} \quad \tilde{H} = \tilde{H}_w(\tau, t) \quad \text{or} \quad \frac{\partial \tilde{H}}{\partial n} = \tilde{Q}_w(\tau, t) \quad \text{for} \quad n = 0 , \quad \tau \le \tau_{te} ; \tag{4.8}$$

and a condition on the fluid velocity normal to a reference wake streamline, i.e.,

$$\tilde{V} = 0 \quad \text{for} \quad n = 0 , \quad \tau > \tau_{te} , \tag{4.9}$$

must be enforced. Here the subscripts w and e denote the values of the fluid properties at a solid wall and at the edge of the viscous layer, respectively, and the subscript te refers to the airfoil trailing-edge point. The fluid velocity, $\tilde{U}_e$, and total enthalpy, $\tilde{H}_e$, at the edges of the viscous layers are determined by the inviscid solution along the blade surfaces and reference wake streamlines [c.f. Eqs. (3.44) and (3.48)].

Turbulence and Transition Models

The models used here and in Ref. [13] to simulate the effects of turbulence and transition on the flow in the viscous layer are the algebraic eddy-viscosity model proposed by Cebeci and Smith [25], the transition length correlation proposed by Dhawan and Narashima [26], and the wake turbulence model proposed by Chang *et al* [27]. Also, since flows in turbomachines are known to be characterized by high freestream turbulence levels, a simple modification developed by Yuhas [28] has been incorporated into the turbulence model to account for the effects of freestream turbulence on the viscous layer. These models are easy to implement, and are known to be reasonably accurate for steady flows with mild pressure gradients. Their ability to accurately represent turbulence and transition in unsteady flows is not known, however; therefore, results must be interpreted with some caution.

The Cebeci-Smith algebraic model divides a solid-surface boundary layer into inner and outer regions, where $\epsilon = \epsilon_i$ and $\epsilon = \epsilon_o$, respectively. The inner model is applied from the wall out to the point at which $\epsilon_i = \epsilon_o$; the outer model, from this point to the edge of the boundary layer. The eddy viscosity in the inner region is given by

$$\epsilon_i = \gamma_{tr}\tilde{\bar{\rho}}(0.41n)^2[1-\exp(-n/\tilde{A}_T)]^2\mathrm{Re}\left|\frac{\partial\tilde{U}}{\partial n}\right| , \tag{4.10}$$

where

$$\tilde{A}_T = \frac{26\tilde{\bar{\mu}}}{\tilde{\bar{\rho}}\sqrt{\mathrm{Re}}}\left\{\left(\tilde{\bar{\rho}}^{-1}\tilde{\bar{\mu}}\frac{\partial\tilde{U}}{\partial n}\right)_w\left[1-11.8\tilde{P}^+\left(\frac{\tilde{\bar{\mu}}_w}{\tilde{\bar{\mu}}_e}\right)\left(\frac{\tilde{\bar{\rho}}_e}{\tilde{\bar{\rho}}_w}\right)^2\right]\right\}^{-\frac{1}{2}} ,$$

$$\tilde{P}^+ = \sqrt{\mathrm{Re}}\frac{\tilde{\bar{\mu}}_e}{\tilde{\bar{\rho}}_e}\left(\frac{\partial\tilde{U}_e}{\partial t}+\tilde{U}_e\frac{\partial\tilde{U}_e}{\partial\tau}\right)\left(\tilde{\bar{\rho}}^{-1}\tilde{\bar{\mu}}\frac{\partial\tilde{U}}{\partial n}\right)_w^{-\frac{3}{2}} , \tag{4.11}$$

and γ_{tr} is a longitudinal intermittency factor which models transitional flow.

The eddy viscosity in the outer region is given by

$$\epsilon_o = \gamma_{tr}\mathrm{Re}\tilde{\bar{\rho}}\tilde{U}_e\chi\int_0^\infty(1-\tilde{U}/\tilde{U}_e)dn , \tag{4.12}$$

where

$$\chi = 1.55\chi_0(1+\pi)^{-1} , \quad \pi = 0.55[1-\exp(-.243z_1^{1/2}-.298z_1)] ,$$
$$z_1 = \begin{cases} \mathrm{Re}_\theta/425-1 & \text{for } \mathrm{Re}_\theta > 425 \\ 0 & \text{for } \mathrm{Re}_\theta \le 425 , \end{cases} \tag{4.13}$$

and

$$\mathrm{Re}_\theta = \frac{\tilde{\bar{\rho}}_w\tilde{U}_e\mathrm{Re}}{\tilde{\bar{\mu}}_w}\int_0^\infty\frac{\tilde{U}}{\tilde{U}_e}(1-\frac{\tilde{U}}{\tilde{U}_e})dn .$$

The parameter π has been defined to account for low momentum thickness Reynolds number. The Clauser constant, χ_0, is usually set equal to 0.0168, but following Yuhas [28] we set

$$\chi_0 = 0.0168[1.0+18.4(\overline{\mathbf{v}'\cdot\mathbf{v}'})_{-\infty}^{\frac{1}{2}}+99.6(\overline{\mathbf{v}'\cdot\mathbf{v}'})_{-\infty}] , \tag{4.14}$$

where $(\overline{\mathbf{v}' \cdot \mathbf{v}'})_{-\infty}$ is the mean-square of the freestream turbulence velocity, to account for the effects of freestream turbulence on the development of the turbulent boundary layer.

Blade boundary layers can contain transitional regions of significant extent. Therefore, a transition model is needed to properly predict boundary-layer flows. Several models have been proposed, based on correlations with experimental data, for steady transitional flows. One of these is the Dhawan-Narashima forced transition model [26] in which the intermittency factor is given by

$$\gamma_{tr} = 1 - \exp\left[-4.6513\left(\frac{\tau - \tau_1}{\tau_2 - \tau_1}\right)^2\right] . \tag{4.15}$$

Here τ_1 and τ_2 are the streamwise locations at the beginning and end of the transition region, respectively. These locations can be specified as functions of time to model unsteady flows.

The eddy viscosity in the wake is based on the model developed by Chang *et al* [27]. At each streamwise station in the wake Equation (4.13) is evaluated twice: once for $-\infty < n \leq n_{\min}$, where $n_{\min}$ is the location at which the streamwise velocity reaches a minimum value, and once for $n_{\min} \leq n < \infty$. The maximum of these two values, $\epsilon_{\max}$, is then used to set the eddy viscosity, $\epsilon_{\mathcal{W}}$, at each streamwise position in the wake, i.e.,

$$\epsilon_{\mathcal{W}} = \epsilon_{\max} - [\epsilon_{\max} - \epsilon_{\max,te}] \exp\left[-\frac{\tau - \tau_{te}}{20\tilde{\bar{\delta}}_{te}}\right] . \tag{4.16}$$

In this equation $\tau - \tau_{te}$ is the distance measured along the reference wake streamline from the trailing edge point, and $\tilde{\bar{\delta}}_{te}$ is the sum of the upper and lower surface boundary-layer thicknesses at the trailing edge. The boundary-layer thickness is defined to be the normal distance from a blade surface to the point at which $\tilde{U}/\tilde{U}_e = 0.995$.

4.2 Transformed Equations

For laminar flows, the Levy-Lees transformation (see Blottner [29]) provides independent variables that effectively capture the growth of the viscous layer with increasing streamwise distance. In addition, the transformed equations reduce to similarity equations at an airfoil leading edge. These features facilitate the determination of a numerical solution. Thus, an extension of the Levy-Lees transformation, in which the laminar edge viscosity is replaced by an effective turbulent viscosity [30], is applied herein to accommodate unsteady turbulent flows.

We define new independent variables ξ and η according to

$$\xi = \int_0^\tau \bar{\mathcal{Q}} d\tau \quad \text{and} \quad \eta = \frac{\tilde{U}_e\sqrt{\mathrm{Re}}}{\sqrt{2\xi}} \int_0^n \tilde{\bar{\rho}} dn , \tag{4.17}$$

where $\bar{\mathcal{Q}} = \bar{\rho}_e U_e \bar{\mu}_e[1 + (\bar{\epsilon}_o/\bar{\mu})_e]$ and $\bar{\epsilon}$ and $\bar{\mu}$ are the turbulent eddy and molecular viscosities in the steady background flow. In Ref. [13] the temporal mean values of the fluid properties, $\tilde{\bar{\rho}}_e$, $\tilde{U}_e$, and $\tilde{\bar{\mu}}_e$, at the edge of the viscous layer were used to define $\bar{\mathcal{Q}}$; however, in the present effort in which the unsteady inviscid flow is regarded as a small perturbation of a nonlinear mean flow, we can replace the temporal mean values of these variables by their values in the

steady background flow to avoid introducing additional nomenclature. The coordinate ξ in (4.17) is a function of τ alone; the coordinate η, by contrast, is a function of τ, n, and t.

We also introduce the new dependent variables

$$\mathcal{F} = \frac{\tilde{U}}{\tilde{U}_e}, \quad \mathcal{V} = \frac{2\xi}{\mathcal{Q}}\left(\frac{1}{\tilde{U}_e}\frac{\partial \eta}{\partial t} + \mathcal{F}\frac{\partial \eta}{\partial \tau} + \sqrt{\frac{\mathrm{Re}}{2\xi}}\tilde{\rho}\tilde{V}\right) \quad \text{and} \quad \mathcal{G} = \frac{\tilde{H}}{\tilde{H}_e}, \tag{4.18}$$

where $\tilde{\mathcal{Q}} = \tilde{\bar{\rho}}_e \tilde{U}_e \tilde{\bar{\mu}}_e [1 + (\epsilon/\tilde{\bar{\mu}})_e]$. After substituting Eqs. (4.17) and (4.18) into the viscous-layer field equations, (4.1), (4.2) and (4.3), and performing some algebra, we find that

$$2\xi \frac{\bar{\mathcal{Q}}}{\tilde{\mathcal{Q}}}\frac{\partial \mathcal{F}}{\partial \xi} + \frac{\partial \mathcal{V}}{\partial \eta} + \frac{\bar{\mathcal{Q}}}{\tilde{\mathcal{Q}}}\mathcal{F} - \alpha_1\alpha_3 = 0, \tag{4.19}$$

$$\frac{2\xi}{\tilde{\mathcal{Q}}\tilde{U}_e}\frac{\partial \mathcal{F}}{\partial t} + 2\xi\frac{\bar{\mathcal{Q}}}{\tilde{\mathcal{Q}}}\mathcal{F}\frac{\partial \mathcal{F}}{\partial \xi} + \mathcal{V}\frac{\partial \mathcal{F}}{\partial \eta} + \alpha_3(\alpha_1\mathcal{F} + \frac{\alpha_2}{2}\mathcal{F}^2 - \mathcal{G}) + \alpha_4(\mathcal{F}^2 - \mathcal{G}) - \frac{\partial}{\partial \eta}\left(l\frac{\partial \mathcal{F}}{\partial \eta}\right) = 0 \tag{4.20}$$

and

$$\begin{aligned}\frac{2\xi}{\tilde{\mathcal{Q}}\tilde{U}_e}\frac{\partial \mathcal{G}}{\partial t} + 2\xi\frac{\bar{\mathcal{Q}}}{\tilde{\mathcal{Q}}}\mathcal{F}\frac{\partial \mathcal{G}}{\partial \xi} + \mathcal{V}\frac{\partial \mathcal{G}}{\partial \eta} + \alpha_5(\mathcal{F}^2 - \mathcal{G}) + \alpha_6(\alpha_1\mathcal{F}\mathcal{G} + \frac{\alpha_2}{2}\mathcal{F}^2 - \mathcal{G}) \\ + \alpha_2\frac{\partial}{\partial \eta}\left[(\hat{l} - l)\mathcal{F}\frac{\partial \mathcal{F}}{\partial \eta}\right] - \frac{\partial}{\partial \eta}\left(\hat{l}\frac{\partial \mathcal{G}}{\partial \eta}\right) = 0\,,\end{aligned} \tag{4.21}$$

where the following parameters have been introduced:

$$\begin{aligned}
\alpha_1 &= \left(1 + \frac{\tilde{U}_e^2}{2\tilde{T}_e}\right)^{-1}, & \alpha_2 &= \tilde{U}_e^2\tilde{T}_e^{-1}\alpha_1\,, \\
\alpha_3 &= 2\xi(\tilde{\mathcal{Q}}\alpha_1\tilde{U}_e^2)^{-1}\frac{\partial \tilde{U}_e}{\partial \tau}\,, & \alpha_4 &= 2\xi\bar{\mathcal{Q}}(\tilde{\mathcal{Q}}\alpha_1\tilde{U}_e)^{-1}\frac{\partial \tilde{U}_e}{\partial \xi}\,, \\
\alpha_5 &= 2\xi(\tilde{\mathcal{Q}}\tilde{U}_e\tilde{H}_e)^{-1}\frac{\partial \tilde{H}_e}{\partial \tau}\left(\frac{\tilde{U}_e^2}{2\tilde{T}_e}\right), & \alpha_6 &= 2\xi\bar{\mathcal{Q}}(\tilde{\mathcal{Q}}\alpha_1\tilde{H}_e)^{-1}\frac{\partial \tilde{H}_e}{\partial \xi}\,, \\
l &= \frac{\tilde{\bar{\rho}}\tilde{\bar{\mu}}(1 + \epsilon/\tilde{\bar{\mu}})}{\tilde{\bar{\rho}}_e\tilde{\bar{\mu}}_e[1 + (\bar{\epsilon}/\bar{\mu})_e]}\,, & \text{and} \quad \hat{l} &= \frac{\tilde{\bar{\rho}}\tilde{\bar{\mu}}[1 + \epsilon Pr/(\tilde{\bar{\mu}}Pr_T)]}{\tilde{\bar{\rho}}_e\tilde{\bar{\mu}}_e[1 + (\bar{\epsilon}/\bar{\mu})_e]Pr}\,.
\end{aligned} \tag{4.22}$$

Special attention must be exercised in applying the foregoing transformation to unsteady wakes. In the present analysis all quantities on the upper (i.e., $n > 0$) and lower ($n < 0$) sides of a wake are referenced to their respective edge conditions, i.e., we set $\mathcal{F} = \tilde{U}/\tilde{U}_e^+$ for $n > 0$ and $\mathcal{F} = \tilde{U}/\tilde{U}_e^-$ for $n < 0$. In general, the inviscid streamwise velocity, $\tilde{U}_e$, and total enthalpy, $\tilde{H}_e$, will be discontinuous across unsteady wakes. As a consequence, the dependent variables $\mathcal{F}$ and $\mathcal{G}$ are discontinuous across reference ($n = 0$) wake streamlines. These discontinuities must be taken into account in developing a numerical solution procedure, to ensure that the physical variables ($\tilde{U}$, $\tilde{V}$ and $\tilde{H}$) are continuous across viscous wakes.

Also, the upper- and lower-surface values of the independent variable ξ will generally differ at a blade trailing edge. Therefore, in the present effort the upper-surface ξ-variable is used to continue the viscous calculation into the wake, i.e.,

$$\xi_W = \xi_{te}^+ + \int_{\tau_{te}}^{\tau} \bar{Q}^+ d\tau_W \ . \tag{4.23}$$

However, two different η-coordinates, i.e.,

$$\eta_W^{\pm} = \frac{\tilde{U}_e^{\pm}\sqrt{\mathrm{Re}}}{\sqrt{2\xi_W}} \int_0^n \tilde{\rho} dn, \quad n \gtrless 0 \ , \tag{4.24}$$

are used for the wake calculation. Thus, at the trailing edge, the lower-surface boundary-layer solution must be interpolated onto the wake η mesh before continuing the viscous calculation into the wake.

Boundary and Initial Conditions on $\mathcal{F}$ and $\mathcal{G}$

In addition to satisfying the field equations (4.19)—(4.21), the dependent variables $\mathcal{F}$ and $\mathcal{G}$ must be prescribed functions of ξ and η at some initial time, and prescribed functions of η and τ at initial or upstream streamwise locations on the upper and lower surfaces of each blade. Also, in terms of the transformed variables, the following conditions must be imposed at the edge(s) of the viscous layer, on the blade surface, and along the reference wake streamline, c.f. Eqs. (4.7), (4.8) and (4.9):

$$\mathcal{F} \to 1 \quad \text{and} \quad \mathcal{G} \to 1 \quad \text{for} \quad |\eta| \to \infty \ , \tag{4.25}$$

$$\mathcal{F} = 0, \ \mathcal{V} = 0, \ \text{and} \ \mathcal{G} = \mathcal{G}_w(\xi, \tau) \ \text{or}$$

$$(\partial \mathcal{G}/\partial \eta)_w = \frac{-(2\xi/Re)^{\frac{1}{2}} \tilde{Q}_w(\xi, \tau)}{\tilde{\rho}_e \tilde{U}_e \tilde{H}_e} \quad \text{for} \quad \eta = 0, \ \xi \leq \xi_{te} \ , \tag{4.26}$$

and

$$\mathcal{V} = 0 \quad \text{for} \quad \eta = 0, \ \xi > \xi_{te} \ , \tag{4.27}$$

respectively.

For the calculations reported herein, the condition at the initial time is the viscous-layer solution in the absence of unsteady excitation, i.e., the solution for steady background flow. The calculated transients resulting from this approximation have been found to die out with increasing time. The upstream profiles, required at each time step of the unsteady viscous-layer calculation, are obtained from a similarity analysis of the flow in the stagnation region, as described below.

4.3 Stagnation Region

We seek a similarity solution for the flow in the stagnation region, which can be used to set the instantaneous upstream profiles, $\mathcal{F}(\xi_I^{\pm}, \eta, t)$ and $\mathcal{G}(\xi_I^{\pm}, \eta, t)$, required to initiate a full viscous-layer calculation. The overall strategy is to develop a similarity solution for

a simple flow configuration and then, to adapt this result for application to the unsteady cascade problem. The present analysis for unsteady, compressible flow is modeled after the incompressible analyses developed independently by Rott [31] and Glauert [32]. Their analyses provided an exact solution to the Navier-Stokes equations for incompressible flow. This is not the case for compressible flow, however, because it is necessary to neglect the dissipation term in the energy equation to obtain a similarity solution. Fortunately, frictional heat dissipation is of limited importance for a wide range of practical flows.

We consider two-dimensional compressible flow around a flat plate, which is oriented normal to the stream direction and undergoes a harmonic motion at velocity $i\omega r_\tau \exp(i\omega t)$ in its own plane. As a convenience to this discussion, we use a complex-variable description for the unsteady flow properties. It is to be understood, however, that the real parts of the various complex parameters represent the actual physical variables. The flow in the viscous layer will be determined in terms of spaced-fixed Cartesian coordinates, τ_S and n_S. The resulting stagnation-region solution can then be expressed in terms of plate-fixed coordinates as a prerequisite to its implementation into the complete unsteady viscous-layer calculation. The τ_S and n_S axes are directed along and normal to the plate, respectively, and the coordinate origin lies at the point at which the dividing inviscid streamline impinges on the plate. The fluid velocity components in the τ_S- and n_S-directions are $\tilde{U}_S$ and $\tilde{V}_S$, respectively.

The inviscid flow is steady relative to the space-fixed frame, with velocity and pressure gradient at the edge of the viscous layer (i.e., at $n_S = 0$ in the inviscid region) given by

$$\tilde{\vec{V}}_{S,e} = \tilde{U}_{S,e}\mathbf{e}_{\tau_S} = c\tau_S \mathbf{e}_{\tau_S} \ , \tag{4.28}$$

and

$$\nabla \tilde{P} = \frac{\partial \tilde{P}}{\partial \tau_S}\mathbf{e}_{\tau_S} = -\tilde{\tilde{\rho}}_e \tilde{U}_{S,e}\frac{\partial \tilde{U}_{S,e}}{\partial \tau_S}\mathbf{e}_{\tau_S} = -\tilde{\tilde{\rho}}_e c^2 \tau_S \mathbf{e}_{\tau_S} \ . \tag{4.29}$$

The constant c in these equations is determined by the behavior of the inviscid solution in the vicinity of the mean stagnation-point location ($\tau_S = 0$). The total enthalpy at the edge of the viscous layer is constant, i.e., $\tilde{H}_e = \tilde{T}_e + \tilde{U}_{S,e}^2/2 = H_{-\infty}$.

The flow in the viscous layer is described by the field equations (4.1)–(4.5), the edge conditions (4.7) and the surface conditions (4.8), except that in the present case

$$\tilde{U}_S(\tau_S, n_S, t) = i\omega r_\tau \exp(i\omega t) \quad \text{for} \quad n_S = 0 \ . \tag{4.30}$$

We assume that this flow is laminar and that the heat generated by viscous dissipation is negligible, i.e., $\tilde{\tilde{\mu}}\partial^2 \tilde{U}_S/\partial n_S^2 \approx 0$. The streamwise velocity and temperature can be expressed in the forms

$$\tilde{U}_S(\tau_S, \eta, t) = c\tau_S f'(\eta) + i\omega r_\tau g(\eta) e^{i\omega t} \ , \tag{4.31}$$

and

$$\tilde{T}(\tau_S, \eta, t) = \tilde{T}_e(\tau_S, t)\theta(\eta) \ , \tag{4.32}$$

where

$$\eta = \left(\frac{c}{\tilde{\tilde{\rho}}_e \tilde{\tilde{\mu}}_e}\right)^{1/2} \int_0^{n_S} \tilde{\tilde{\rho}} dn_S \ . \tag{4.33}$$

Note that $\partial\tilde{P}/\partial n_S \approx 0$ and $\tilde{V}_S \ll \tilde{U}_S$; therefore, $\tilde{\tilde{\rho}}_e/\tilde{\tilde{\rho}} = \tilde{T}/\tilde{T}_e = \theta$ and $H = \tilde{T} + \tilde{U}_S^2/2$ in the viscous layer.

After substituting the foregoing results into the field equations that govern the flow in the viscous layer and performing the necessary algebra, we obtain an expression for the normal component of the fluid velocity, $\tilde{V}_S$, and the following set of ordinary differential equations for f, g and θ.

$$f'^2 - ff'' - (lf'')' - \theta = 0 \ , \tag{4.34}$$

$$(\frac{i\omega}{c} + f')g - fg' - (lg')' = 0 \ , \tag{4.35}$$

and

$$\left(\frac{l}{Pr}\theta'\right)' + f\theta' = 0 \ , \tag{4.36}$$

where $l = \tilde{\tilde{\rho}}\tilde{\tilde{\mu}}/(\tilde{\tilde{\rho}}_e\tilde{\tilde{\mu}}_e)$. The conditions on f, g and θ at the plate surface ($\eta = 0$) and at the edge of the viscous layer ($\eta \to \infty$) are

$$f(0) = f'(0) = 0 \ , \quad g(0) = 1 \quad \text{and} \quad \theta'(0) = 0 \quad \text{or} \quad \theta(0) = \tilde{T}_w/\tilde{T}_e \ ; \tag{4.37}$$

and

$$f'(\infty) = 1 \ , \quad g(\infty) = 0 \quad \text{and} \quad \theta(\infty) = 1 \ . \tag{4.38}$$

Note that for steady ($g \equiv 0$), incompressible ($\theta \equiv 1$) flow, we recover the classical stagnation-region problem studied by Hiemenz. Also, Eq. (4.36) is identical in form to the energy equation that describes steady compressible stagnation-point flow [33]. Finally, the present analysis can be readily extended to consider more general unsteady motions, e.g.,

$$\tilde{U}_S = c\tau_S f'(\eta) + \sum_{n=1}^{N} i\omega_n r_{\tau,n} g_n(\eta) \exp(i\omega_n t) \ . \tag{4.39}$$

In this case solutions for N uncoupled equations for the g_n, $n = 1, 2, 3, \ldots, N$, are required.

The set of nonlinear ordinary differential equations for f, θ and g can be solved using an implicit finite-difference technique similar to that used to obtain nonsimilar solutions to the full unsteady viscous equations (cf. §4.4). The functions f and θ must be determined simultaneously, but they are independent of g, which can be determined once f is known.

To provide the upstream profiles required for a complete viscous-layer calculation it is convenient to express the stagnation-region solution in terms of body- or plate-fixed coordinates. Thus, we consider Cartesian coordinates τ, n, where the τ- and n-axes are parallel to the spaced-fixed τ_S- and n_S-axes, respectively, and the mean position of the τ, n coordinate origin coincides with the origin of the spaced-fixed τ_S, n_S-frame. The streamwise positions and velocities of a fluid particle in the two coordinate frames are related by

$$\tau_S = \tau + r_\tau \exp(i\omega t) \tag{4.40}$$

and

$$\tilde{U}_S = \tilde{U} + i\omega r_\tau \exp(i\omega t) \ . \tag{4.41}$$

After combining (4.31), (4.40) and (4.41), we find that

$$\tilde{U} = c\tau f'(\eta) + b\lambda(\eta) \exp(i\omega t) \ , \tag{4.42}$$

where

$$b = c\tau_\tau(1 - i\omega/c) \ , \tag{4.43}$$

and

$$(1 - i\omega/c)\lambda(\eta) = f'(\eta) + (i\omega/c)[g(\eta) - 1] \ . \tag{4.44}$$

At the plate surface $\tilde{U} = 0$, and at the edge of the viscous layer

$$\tilde{U}(\eta \to \infty) = \tilde{U}_e = c\tau + b\exp(i\omega t) \ . \tag{4.45}$$

The total enthalpy $H = \tilde{U}_S^2/2 + \tilde{T}$ is given by

$$\begin{aligned} H = (c\tau f')^2/2 + c(1 - i\omega/c)^{-1} b\tau f'(f' + i\omega g/c)\exp(i\omega t) \\ +(1 - i\omega/c)^{-2} b^2 (f' + i\omega g/c)^2 \exp(2i\omega t)/2 + \tilde{T}_e\theta \ . \end{aligned} \tag{4.46}$$

The locations, i.e., $\tau = \pm|\tau_I|$, at which the stagnation-region solution can be applied as an initial condition for an unsteady viscous-layer calculation are determined by two criteria. First, the stagnation-point motion must be contained within the interval $[-|\tau_I|, |\tau_I|]$ and second, to avoid stability problems in the subsequent boundary-layer calculation, those points at which flow reversals, i.e., $(\partial\tilde{U}/\partial n)_w < 0$, occur must also be contained within this interval. Reverse flow is associated with the lag in the response of the low-momentum fluid near the wall to changes in the velocity at the edge of the viscous layer. The extent of the interval over which the stagnation point moves, i.e., $[-|\tau_M|, |\tau_M|]$, is determined from the inviscid velocity distribution (4.45) and is given by $[-c^{-1}|b|, c|b|]$. The extent of the reverse-flow interval, i.e., $[-|\tau_R|, |\tau_R|]$, is determined by the maximum and minimum values of τ for which $(\partial\tilde{U}/\partial\eta)_w = 0$. We find that

$$|\tau_R| \le c^{-1}|b| \left| \frac{1 + i\omega c^{-1} g'(0)/f''(0)}{1 - i\omega/c} \right| \ . \tag{4.47}$$

Thus, $|\tau_I| \ge \max(|\tau_M|, |\tau_R|)$. For our application to unsteady cascade flows, we have found that setting $|\tau_I| = 2c^{-1}|b|$ leads to reasonable results in the stagnation region and allows us to continue the viscous-layer calculation over blades and their wakes.

In applying the foregoing stagnation-region analysis to unsteady cascade flows, we use the inviscid velocity distribution along a blade surface, i.e.,

$$\tilde{U}_e(\tau, t) = U_e(\tau) + u_e(\tau)\exp(i\omega t) + \dots \ , \tag{4.48}$$

where $U_e(\tau)$ and $u_e(\tau)$ are the nonlinear steady and the complex amplitude of the linearized unsteady velocities, respectively, to determine the parameters c and b in (4.42) and (4.46). In particular, these parameters are determined by matching the analytical velocity profile (4.42) to the calculated inviscid velocities at $\pm|\tau_I|$, i.e., we set

$$c = (\partial U_e/\partial\tau)_{\tau=0} \quad \text{and} \quad b = u_e(\pm\tau_I) \tag{4.49}$$

Thus, with ω specified as an input quantity, the functions f θ and g determined by an implicit finite-difference procedure and the parameters b and c given by (4.49), the streamwise velocity (4.42) and total enthalpy (4.46) profiles needed to initiate the unsteady viscous-layer calculation can be specified.

4.4 Numerical Solution Procedure

The transformed form of the viscous-layer equations [Eqs. (4.19)-(4.21) and (4.25)-(4.27)] are solved by using a finite-difference approach to approximate the various partial derivatives and to convert the system of differential equations into a system of algebraic equations. Streamwise and temporal derivatives are approximated by first-order backward differences and normal derivatives are approximated by second-order central differences. The streamwise momentum and energy equations contain nonlinear terms, and therefore, they must be linearized to facilitate their solution at each point in space and time. This is accomplished by using a Newton iteration in which the initial guess for the profiles comes from the solution at the previous spatial or temporal step. The equations are solved using local iteration to remove the linearization error, and repeating the iteration until the values of the flow variables converge to within a specified tolerance level. The finite-difference approximation results in a block tridiagonal system of linear algebraic equations at each step, which is solved using the Thomas block inversion algorithm.

The analyses for surface boundary layers and wakes are almost identical, except for the implementation of different boundary conditions. In addition to replacing the surface no-slip condition with a zero normal velocity condition at the reference wake streamline, the possibility of jumps in the tangential velocity and total enthalpy across a viscous wake must be taken into account. As discussed previously, the transformed governing equations are written in terms of two different sets of variables, each applying on one side of the wake streamline, and scaled to the edge conditions for that side. For example, on the upper side of the wake, $F^+ = u/u_e^+$ and $G^+ = H/H_e^+$; on the lower side, $F^- = u/u_e^-$ and $G^- = H/H_e^-$. The discretized equations on either side of the reference wake streamline are written in terms of that side's variables. However, at the wake streamline, ($\eta = 0$), variables from both sides of the wake are used in the momentum and energy equations, due to the use of central-difference approximations for the η-derivatives. For consistency, the equations must be written in terms of a single set of variables. This is accomplished here by writing the equations in terms of the upper surface quantities. Thus, whenever a lower surface variable appears in the equations at $\eta = 0$, it is rewritten in terms of the upper surface edge conditions. For example, the variable F^- is written in upper variables as $F^- \cdot (u_e^-/u_e^+) = u^-/u_e^+$. Further details on the reference wake streamline procedure are given in the Appendix, where the finite-difference solution procedure for the viscous layer is discussed in detail.

The finite-difference approximation is implemented on a grid that is nonuniform in both spatial directions, and uniform in time. The grid distribution in the streamwise direction is chosen so as to cluster points near the blade leading and trailing edges, with each mesh interval being set equal to a constant times the previous one, according to the relation

$$\Delta\xi_{l+1} = K_\xi \Delta\xi_l \ , \quad l = 1,\ 2,\ \ldots\ , L \tag{4.50}$$

where l is the streamwise mesh point index ($l = 1$ at the blade leading edge and increases with distance downstream), $K_\xi > 1$ from the leading edge of the blade to midchord, and $K_\xi < 1$ from midchord to the trailing edge. The grid is then stretched (i.e., $K_\xi > 1$) aft of the trailing edge, and generally extends between one and two blade chords downstream of the trailing edge.

A stretched grid is also employed in the normal direction, with clustering near the surface to capture the large velocity gradients that occur near the wall, and to ensure that, for turbulent flow, there are enough points in the near-wall region to adequately resolve the laminar sublayer. Geometric stretching is again employed, with

$$\Delta\eta_{n+1} = K_\eta \Delta\eta_n \ , \quad n = 1,\ 2,\ \ldots\ , N \tag{4.51}$$

where n is a normal mesh point index ($n = 1$ at the blade surface or reference wake streamline and increases with increasing distance into the flow). Since the resolution requirements are a function of the solution, the normal grid stretching, K_η, and the spacing at the wall, $\Delta\eta_1$, must be determined for each case. For turbulent flow, this is accomplished by monitoring the value of Y^+ at the first mesh point from the wall (i.e., $Y^+_{n=2}$), where Y^+ is a Reynolds number based on the friction velocity, $(\tilde{\bar{\tau}}_w/\tilde{\bar{\rho}}_w)^{1/2}$ and the normal distance from the blade surface. For accuracy, Y_2^+ should be close to one, which can be achieved by adjusting $\Delta\eta_1$. The stretching parameter K_η is then adjusted to place the outer edge of the mesh, $\eta = \eta_N$, far enough from the surface to allow the edge conditions to be approached asymptotically. The number of points used in the normal direction is chosen to allow the flow over the entire viscous layer to be resolved accurately at all streamwise stations — generally, between 50 and 100 points are sufficient.

The constant value of the time-step used for the temporal discretization is chosen based on the frequency of the imposed unsteady excitation and the number of time-steps prescribed for each period of oscillation, generally between 20 and 50.

5. Numerical Results

Response predictions will be given below for two-dimensional blade rows operating at subsonic Mach numbers and subjected to external unsteady aerodynamic excitations to demonstrate the present capabilities of the linearized inviscid unsteady flow analysis, LINFLO, and the unsteady viscous-layer analysis, UNSVIS. The inviscid analysis will be applied to predict the response of compressor and turbine cascades, and their flat-plate counterparts, to vortical excitations; the unsteady viscous analysis, to study the viscous-layer responses of flat-plate and turbine cascades to incident acoustic excitations.

5.1 Inviscid Flow: Vortical Excitation

We consider two of the cascades studied in Ref. [16] — a compressor exit guide vane (EGV) and a turbine cascade proposed as the fourth standard cascade configuration for turbomachinery aeroelastic investigations by Fransson and Suter in Ref. [34]. In addition, we will compare the unsteady responses of these compressor and turbine configurations to those of corresponding flat-plate cascades, i.e., flat-plate cascades having the same blade spacing, G, and operating at the same inlet flow conditions, $M_{-\infty}$ and $\Omega_{-\infty}$, as the real-blade configuration. However, the flat-plate blades are staggered so that the blade mean positions are aligned with the mean inlet flow direction, i.e., $\Theta = \Omega_{-\infty}$. Therefore, the local steady Mach number, $M = M_{-\infty}$, and flow angle, $\Omega = \Omega_{-\infty}$, are constants throughout the flat-plate flow fields. The steady background flows through the EGV and turbine cascades have been determined using the methods of Ref. [18]. In each case a Kutta condition has been applied at blade trailing edges; therefore, only inlet uniform flow information, e.g., $M_{-\infty}$ and $\Omega_{-\infty}$, must be specified for the steady calculations.

First-harmonic unsteady solutions have been determined, using LINFLO, on a global H-type mesh and, for one EGV calculation, on a composite mesh constructed from this H-mesh and a polar-type local mesh. The H-mesh used here consists of 40 mean-flow streamlines and 155 "axial" lines and extends one axial chord upstream and downstream of the blade row. The mesh streamlines are packed near the blade and wake surfaces; the axial lines, near the blade edges. The local mesh used in the composite-mesh EGV calculation consisted of 100 radial lines and 11 "circumferential" lines, with the latter being tightly packed near the blade surface. As part of this study, classical linearized theory (CLT) response predictions have also been determined for the flat-plate cascades using the analysis of Smith (Ref. [35]).

The unsteady flows are excited by vortical gusts. The temporal frequency, ω, interblade phase angle, σ, and complex amplitude of the gust velocity component normal to the freestream direction, i.e., $\mathbf{v}_{R,-\infty} \cdot \mathbf{e}_N$, are prescribed quantities. The component of the gust velocity in the inlet freestream direction, $\mathbf{v}_{R,-\infty} \cdot \mathbf{e}_T$, is determined by the divergence-free condition, i.e., $i\boldsymbol{\kappa}_{-\infty} \cdot \mathbf{v}_{R,-\infty} \equiv 0$. The wave number $\boldsymbol{\kappa}_{-\infty}$ has a component $\kappa_{\eta,-\infty} = \sigma G^{-1}$ in the cascade- or η-direction and a component $\kappa_T = -\omega V_{-\infty}^{-1} = -\omega$ in the inlet freestream direction. Therefore,

$$\begin{aligned} \boldsymbol{\kappa}_{-\infty} &= -(\omega \sec\Omega_{-\infty} + \sigma G^{-1} \tan\Omega_{-\infty})\mathbf{e}_\xi + \sigma G^{-1}\mathbf{e}_\eta \\ &= -\omega \mathbf{e}_T + (\omega \tan\Omega_{-\infty} + \sigma G^{-1} \sec\Omega_{-\infty})\mathbf{e}_N \ . \end{aligned} \tag{5.1}$$

For a pure vortical excitation the rotational velocity field is given by

$$\mathbf{v}_R(\mathbf{x}) = \boldsymbol{\nabla}(\mathbf{X} \cdot \mathbf{v}_{R,-\infty}) \exp(i\boldsymbol{\kappa}_{-\infty} \cdot \mathbf{X}) \ , \tag{5.2}$$

where $\mathbf{X}$ is defined in Eq. (3.18). For the flat-plate cascades and far upstream of the EGV and turbine blade rows $\mathbf{v}_R(\mathbf{x}) = \mathbf{v}_{R,-\infty} \exp(i\boldsymbol{\kappa}_{-\infty} \cdot \mathbf{x})$, and the complex amplitudes of the gust vorticity is $\boldsymbol{\zeta}_{-\infty} = i\boldsymbol{\kappa}_{-\infty} \times \mathbf{v}_{R,-\infty}$.

Since the inlet and exit flows considered here are subsonic, a subresonant unsteady excitation produces an acoustic response in which all waves attenuate with increasing axial distance from the blade row. A superresonant (m,n) excitation produces a response in which m and n such waves persist far upstream and/or far downstream, respectively, and carry energy away from the blade row. An acoustic resonance occurs if at least one acoustic response wave persists in the far field and carries energy along the blade row.

We will examine the response of the compressor, turbine and corresponding flat-plate cascades to vortical gusts with $\mathbf{v}_{R,-\infty} \cdot \mathbf{e}_N = (1,0)$, $\omega = 5$ and $-3\pi \leq \sigma \leq -\pi$. It should be noted that ω and σ must be of opposite sign to model a realistic cascade/vortical gust interaction. In the present study we set $\omega > 0$, and therefore, σ must be less than zero. Theoretical predictions will be given for the Mach number, drift function and stream function in the steady background flows, and for the vorticity, source term, velocity potential and pressure in the linearized unsteady flows through the compressor and turbine cascades. We will also examine the behavior of the unsteady pressure differences $[\Delta p(x) = p(\mathbf{x}_B^-) - p(\mathbf{x}_B^+)]$ and unsteady aerodynamic moments (m) acting on the reference $(m = 0)$ blades of the compressor, turbine and corresponding flat-plate blade rows.

Compressor Exit Guide Vane

The blades of the compressor exit guide vane (EGV) are constructed by superimposing the thickness distribution of a NACA 0012 airfoil on a circular arc camber line with height at midchord of 0.13. This cascade has a stagger angle Θ of 15 deg, a blade spacing G of 0.6 and operates at an inlet Mach number and inlet flow angle of 0.3 and 40 deg, respectively. The calculated exit Mach number, exit flow angle and mean lift force, $F_y\mathbf{e}_y$, acting on each blade are 0.226, -7.4 deg and 0.36, respectively. The predicted steady Mach number field and Mach number distribution along a blade surface for the steady flow at $M_{-\infty} = 0.3$ and $\Omega_{-\infty} = 40\,\text{deg}$ through the EGV are shown in Figure 4; the drift and stream function contours, in Figure 5. Far upstream of the blade row, the drift function contours are parallel to each other and perpendicular to the inlet freestream direction, but as the flow proceeds downstream, gradients in the steady velocity produce distorted contours. These distortions are mild over most of the blade passage, but quite severe in the immediate vicinity of the mean blade and wake surfaces, where the drift function contours stretch downstream from the leading-edge stagnation point.

The meshes used to determine global- and composite-mesh solutions for the unsteady potential are depicted in Figure 6. The streamline global mesh shown here was also used to evaluate the rotational velocities, $\mathbf{v}_R$ and $\mathbf{v}_*$, the vorticity, $\boldsymbol{\zeta}$, and the potential-equation source term, $\bar{\rho}^{-1}\boldsymbol{\nabla} \cdot (\bar{\rho}\mathbf{v}_*)$, over the extended blade passage solution domain. For the composite-mesh potential calculations, the values of these quantities at the local-mesh points were determined by an interpolation from the global to the local mesh.

Global- and composite-mesh solutions for the in-phase component (real part) of the unsteady potential due to a vortical excitation at $\sigma = -2\pi$ are shown in Figure 7 the global- and composite-mesh results for the unsteady pressure-difference response, in Figure 8. The results in Figures 7 and 8 indicate that there are only slight differences between the global and composite-mesh unsteady flow solutions, and hence, that the streamline H-mesh of Ref. [12] and [16] is adequate for predicting low-speed unsteady cascade flows. The global mesh analysis is very efficient; for example, a complete unsteady flow calculation on a 155×40 global mesh requires about 2 1/2 minutes of CPU time on an APOLLO 10000 work station. Most of the information determined from such a calculation can be saved and re-used in subsequent unsteady flow calculations for different frequencies, interblade phase angles, and modes of excitation, which then require only about 23 seconds of CPU time for each unsteady case. Composite-mesh calculations typically require four (4) times the CPU time required for a global mesh calculation. It should be noted, however, that the composite-mesh analysis represents an important solution capability because it allows a great deal of flexibility in prescribing a mesh structure for accurately analyzing linearized unsteady flows. In addition, this type of capability will be essential for analyzing transonic problems in which a mesh that conforms to the mean shock loci is required to accurately predict the effects of shock displacements.

We proceed to examine in somewhat more detail the unsteady flows through the EGV that are excited by vortical gusts with $\mathbf{v}_{R,-\infty} \cdot \mathbf{e}_N = (1, 0)$ and $\omega = 5$. These results (Figures 9 through 15) and similar ones for the turbine in Figures 18 through 24 were determined using global mesh calculations. Contours of the in-phase component or real part of the unsteady vorticity, source term and pressure are shown in Figures 9, 10 and 11, respectively, for vortical excitations at $\sigma = -\pi$, -2π and -3π. The wave-number magnitudes, $|\boldsymbol{\kappa}_{-\infty}|$, associated with these gusts are 5.66, 10.73 and 17.08, respectively, and the arguments relative to the axial flow direction, $\alpha = \tan^{-1}(\kappa_{\eta,-\infty}/\kappa_{\xi,-\infty})$, are -112.1 deg, -77.8 deg and -67.0 deg, respectively. The vortical gusts are distorted as they are convected by the nonuniform mean flow through the EGV. The vorticity contours in Figure 9 and the source term contours in Figure 10 indicate that this distortion increases in severity, i.e., the vorticity and source-term contours are more severely stretched and re-oriented within the blade and wake passages with increasing values of $|\boldsymbol{\kappa}_{-\infty}|$. The results in Figure 10 reveal the rather strong variations in the source term that occur throughout the extended blade passage solution domain, particularly for the high wave number gust.

The vortical gusts at $\sigma = -\pi$ and $\sigma = -3\pi$ produce a subresonant pressure response, i.e., all acoustic response waves attenuate with increasing axial distance from the blade row (see Figure 11). The vortical excitation at $\sigma = -2\pi$ produces a superresonant (1,1) response in which a pressure response disturbance at $\omega = 5$ and $\kappa_\eta = 0$ propagates away from the blade row in both the far upstream and far downstream directions. Note the spurious pressure behavior indicated in Figure 11 at the upstream boundary (for $\sigma = -2\pi$) and at the downstream boundary (for $\sigma = -2\pi$, -3π) of the solution domain. This can be attributed to the nonuniform spacings between the mesh streamlines currently used in the global mesh calculations. The global mesh streamlines must be packed near the blade and wake surfaces to resolve the vortical flow near these surfaces, but this leads to a reduced accuracy in matching the numerical near-field and analytical far-field solutions for the unsteady potential at the inlet and exit boundaries, and thus, in predicting the acoustic response in the far field. The

use of a composite-mesh procedure in which the global mesh contained uniformly spaced streamlines might overcome this problem.

Responses at the reference blades of EGV and corresponding flat-plate cascades are depicted in Figures 12–15. The flat-plate cascade has a stagger angle of $\Theta = \Omega = 40$ deg, a blade spacing $G = 0.6$, and operates at a Mach number, M, of 0.3. The flat-plate predictions presented in Figures 12–15 have been determined using both LINFLO and the classical linearized analysis of Smith (Ref. [35]). Recall that in the general linearization the unsteady potential equation (3.11) contains a source term, i.e., $\bar{\rho}^{-1}\nabla \cdot (\bar{\rho}\mathbf{v}_*)$, and the normal derivative of the potential, $\nabla\phi \cdot \mathbf{n}$, is zero at the mean blade surfaces. For flat-plate blades aligned with the inlet flow direction the source term reduces to $\nabla^2\phi_*$. In the classical linearization the potential equation is homogeneous, and the normal derivative of the potential cancels the normal component of the gust velocity at the mean blade surfaces. Thus, a comparison between the present and the classical linearizations is quite meaningful because it reveals the ability of the numerical field methods, associated with the former, to accurately account for the strong source term variations that occur over the solution domain.

The pressure difference distributions that act on the reference blade of the EGV and flat-plate cascades for vortical excitations at $\mathbf{v}_{R,-\infty} \cdot \mathbf{e}_N = (1, 0)$, $\omega = 5$ and $\sigma = -\pi$, $\sigma = -2\pi$ and $\sigma = -3\pi$ are shown in Figures 12, 13 and 14, respectively. The unsteady moments acting on the reference blades of the two cascades are plotted versus interblade phase angle for vortical excitations at $\mathbf{v}_{R,-\infty} \cdot \mathbf{e}_N = (1, 0)$, $\omega = 5$ and $-3\pi(-540\,\text{deg}) \leq \sigma \leq -\pi(-180\,\text{deg}$ in Figure 15. Here, the excitations at $\sigma = -404.2$ deg and -293.9 deg produce resonant acoustic response disturbances far upstream and far downstream of the flat-plate cascade and far upstream of the EGV; those at $\sigma = -414.3$ deg and -308.8 deg produce such responses far downstream of the EGV.

Vortical gusts are convected without distortion by the uniform mean flow through the flat-plate cascade, i.e., the rectilinear vorticity contour patterns that exist far upstream of the EGV blade row are maintained throughout the flat-plate flow field. The results in Figures 12–14 indicate the effects of gust distortion, due to nonuniform mean flow phenomena, on blade pressure-difference responses. For the vortical gusts at $\sigma = -\pi$ and $\sigma = -2\pi$ the pressure-difference distributions along the EGV and flat-plate blades show somewhat similar qualitative behaviors, but important quantitative differences. Such differences between real blade and flat-plate responses coincide with intuitive expectations. In contrast, the responses of the EGV and flat-plate blades to the vortical gust at $\sigma = -3\pi$ bear almost no qualitative resemblance. This result is somewhat surprising and, if correct, indicates the effect of mean-flow nonuniformity on the unsteady pressure response of cascades to high-wave-number vortical excitations to be quite substantial. The real blade and flat-plate moment responses shown in Figure 15 again show some qualitative similarity except, perhaps, over the phase-angle range $-540\,\text{deg} \leq \sigma < -420\,\text{deg}$.

Note that the LINFLO and Smith analysis (CLT) pressure-difference predictions in Figures 12 through 14 for the flat-plate cascades are in excellent agreement. Indeed, the pressure-difference curves predicted by the two analyses are almost coincident for the gusts at $\sigma = -\pi$ and $\sigma = -2\pi$, and only slight differences exist for $\sigma = -3\pi$. The LINFLO and classical theory predictions for the moment response (Figure 15) are in excellent agreement over the entire interblade phase angle range, i.e., $-3\pi \leq \sigma \leq -\pi$.

Turbine Cascade

As a representative turbine configuration we have selected the fourth standard configuration of Ref. [34], but for the present study we have modified the blade profiles defined in Ref. [34] so that our example blades close in sharp, i.e., wedge-shaped, trailing edges. The turbine cascade and the corresponding flat-plate configuration operate at an inlet Mach number of 0.19 and an inlet flow angle of 45 deg, and the blade spacing G is 0.76. The turbine cascade has a stagger angle of 56.6 deg, and the flat-plate blades are staggered at $\Theta = \Omega = 45$ deg. The calculated exit Mach number and flow angle for the turbine are 0.49 and 72.0 deg, respectively, and the mean lift acting on each blade is -2.11. The predicted steady Mach number contours and blade-surface Mach number distributions for the steady flow at $M_{-\infty} = 0.19$ and $\Omega_{-\infty} = 45$ deg through the turbine are shown in Figure 16. The drift and stream function contours for this flow are shown in Figure 17. Note the stretching of the drift function contours within the blade passage, which is caused by the acceleration of the steady flow.

Linearized unsteady flow predictions for the turbine cascade, as determined using the LINFLO global-mesh analysis, are presented in Figures 18 through 24. Contours of the in-phase component or real part of the unsteady vorticity, source term and pressure are shown in Figures 18, 19 and 20, respectively, for vortical excitations at $\sigma = -\pi$, -2π and -3π. The wave number magnitudes, $|\kappa_{-\infty}|$, and arguments with respect to the axial direction, $\alpha_{-\infty}$, for these excitations are 5.08, 8.36 and 13.50 and -125.4 deg, -81.7 deg and -66.7 deg, respectively. As indicated in Figures 18 and 19, the vortical gusts are highly distorted as they are convected through the turbine blade row. The unsteady vortical and source term contour patterns for the gusts at $\sigma = -2\pi$ and $\sigma = -3\pi$ are quite different from those for the gust at $\sigma = -\pi$. In the latter case the rectilinear vorticity contours far upstream of the blade row evolve into bowed shapes as the gust is carried through the blade row by the mean flow. The vorticity contours for the gusts at $\sigma = -2\pi$ and $\sigma = -3\pi$ are close to being straight lines far downstream of the blade row, but these show substantial changes in orientation relative to their upstream states. The source term contours in Figure 19 are severely distorted by the turbine blade row from mid-blade passage to the downstream boundary of the solution domain, particularly for the vortical gusts at $\sigma = -2\pi$ and $\sigma = -3\pi$. Also, the source terms associated with the gusts at $\sigma = -2\pi$ and $\sigma = -3\pi$ have very large gradients within the blade passage and downstream of the blade row. These give rise to relatively large unsteady pressure responses, as indicated in Figure 20. Note that the vortical excitations at $\sigma = -\pi$ and $\sigma = -3\pi$ produce a subresonant pressure response; whereas the excitation at $\sigma = -2\pi$, a superresonant (1,1) response.

The unsteady pressure-difference distributions acting on the reference blades of the turbine cascade, and its flat-plate counterpart, for vortical excitations at $\sigma = -\pi$, -2π and -3π are shown in Figures 21, 22 and 23, respectively. Moment responses to incident vortical gusts with $\mathbf{v}_{R,-\infty} \cdot \mathbf{e}_N = (1, 0)$, $\omega = 5$ and -3π (-540 deg) $< \sigma < -\pi$ (-180 deg) are shown in Figure 24. The excitations at $\sigma = -396.8$ deg and $\sigma = -311.7$ deg produce resonant acoustic response disturbances far upstream of the turbine cascade, and far upstream and far downstream of the flat-plate cascade. Those at $\sigma = -389.0$ deg and at $\sigma = -279.2$ deg produce such response disturbances far downstream of the turbine cascade. The unsteady pressure differences associated with the turbine and flat-plate cascades are qualitatively sim-

ilar for $\sigma = -\pi$, but differ substantially for $\sigma = -2\pi$ and $\sigma = -3\pi$. The unsteady moment responses, particularly those for the in-phase moment, differ substantially over a significant range of interblade phase angles, i.e., $-540\,\text{deg} < \sigma < -300\,\text{deg}$. Again, the flat-plate pressure-difference and moment responses predicted by LINFLO and the classical analysis of Smith are in very good agreement.

The unsteady response predictions for the turbine and flat-plate cascades again indicate that mean-flow nonuniformities have a substantial impact on the unsteady aerodynamic response of cascades to vortical gusts, particularly for gusts occurring at high wave number. The large differences between the pressure-difference responses for the EGV and its corresponding flat-plate cascade for a vortical excitation at $\sigma = -3\pi$ and between those for the turbine and its corresponding flat-plate configuration for excitations at $\sigma = -2\pi$ and $\sigma = -3\pi$ suggest that additional studies be undertaken to better understand the effects of mean-flow nonuniformity on blade response to high wave number vortical gusts.

5.2 Viscous Flow: Acoustic Excitation

Unstaggered Flat-Plate Cascade

As a benchmark case to demonstrate the unsteady viscous-layer analysis, UNSVIS, we consider unsteady flow through an unstaggered flat-plate cascade. Here, the uniform inlet velocity $\mathbf{V}_{-\infty}$ is aligned with the mean positions of the blade chord lines. Hence, the steady background flow is uniform with velocity, pressure and total enthalpy given by $\mathbf{V} = \mathbf{e}_\xi$, $P = (\gamma M^2)^{-1}$, and $H = \frac{1}{2} + (\gamma - 1)^{-1} M^{-2}$, respectively. The unsteadiness is excited by an incident pressure disturbance, which carries acoustic energy toward the blade row from either far upstream ($-\infty$) or far downstream ($+\infty$). The acoustic excitation travels in the axial (or chordwise) direction, i.e., $\kappa_\eta = \kappa_y = \sigma/G = 0$, and is therefore described by a velocity potential of the form [cf. (3.17)].

$$\tilde{\phi}(\mathbf{x}, t) = -\text{Re}\{[i(\kappa_{\xi,\mp\infty} + \omega)]^{-1} p_{I,\mp\infty} \exp[i(\kappa_{\xi\mp\infty}\xi + \omega t)]\} \ , \tag{5.3}$$

where ω, $\kappa_\xi = \kappa_x$ and $p_{I,\mp\infty}$ are the temporal frequency, axial wave number and complex amplitude of the unsteady pressure excitation, respectively. The axial wave number is related to the temporal frequency by [cf. (3.33)]

$$\kappa_{\xi,\mp\infty} = \frac{\mp\omega M}{1 \pm M} \ . \tag{5.4}$$

Note that for a given temporal frequency, ω, and Mach number, $M < 1$, $|\kappa_{\xi,+\infty}| > |\kappa_{\xi,-\infty}|$, because a disturbance coming from downstream travels against the freestream flow direction.

The flat-plate cascade produces no response to the pressure excitation described by Eq. (5.3); therefore, this equation describes the entire first-harmonic inviscid flow field. The time-dependent velocity, pressure, and total enthalpy in the flow are then given by

$$\tilde{P} = P + \tilde{p} + \ldots = (\gamma M^2)^{-1} + \text{Re}\{p_{I,\mp\infty} \exp[i(\kappa_{\xi,\mp\infty}\xi + \omega t)]\} + \ldots \ , \tag{5.5}$$

$$\tilde{\mathbf{V}} = \mathbf{V} + \tilde{\mathbf{v}} + \ldots = [1 \pm M\text{Re}\{p_{I,\mp\infty} \exp[i(\kappa_{\xi,\mp\infty}\xi + \omega t)]]\}\mathbf{e}_\xi + \ldots \tag{5.6}$$

and

$$\tilde{H} = H + \tilde{h} + \ldots = H + (1 \pm M)\mathrm{Re}\{p_{I,\mp\infty} \exp[i(\kappa_{\xi,\mp\infty}\xi + \omega t)]\} + \ldots \ . \tag{5.7}$$

where $\tilde{p} = -\bar{D}\tilde{\phi}/Dt$, $\tilde{\mathbf{v}} = \nabla\tilde{\phi}$, and $\tilde{h} = -\bar{D}\phi/Dt + \nabla\phi \cdot \mathbf{e}_\xi$ are the first-harmonic unsteady pressure, velocity and total enthalpy, respectively. The real and imaginary components of the complex amplitude of the first-harmonic unsteady pressure acting along each blade and wake surface ($0 \le x = \xi \le 2$) for a cascade operating at $M = 0.5$ and subjected to upstream acoustic disturbances with $p_{I,-\infty} = (1,0)$ and $\omega = 1$, 2, 5 and 10 are shown in Figure 25; similar results for downstream acoustic disturbances, in Figure 26. The pressure distributions shown in Figures 25 and 26 have been determined from Eqs. (5.4) and (5.5).

The inviscid results in Eqs. (5.5) — (5.7) have been used as edge conditions for a series of unsteady viscous-layer calculations. The latter allow us to examine the effects of pressure-excitation amplitude, temporal frequency and axial wave number on the behavior of the viscous-layer displacement thickness, $\tilde{\bar{\delta}}(\mathbf{x},t)$, surface shear stress $\tilde{\bar{\tau}}_w = (\mathrm{Re})^{-1}(\tilde{\bar{\mu}}\partial\tilde{U}/\partial n)_w$ and wake centerline velocity $\tilde{U}_{\ell}$. In particular, we can decompose each of these quantities into Fourier series; e.g.,

$$\tilde{\bar{\delta}}(\mathbf{x},t) = \int_0^\infty [1 - \tilde{\bar{\rho}}\tilde{U}/(\tilde{\bar{\rho}}_e\tilde{U}_e)]dn = \sum_{n=-\infty}^{\infty} \delta_n(\mathbf{x}) \exp(in\omega t) \ , \tag{5.8}$$

where

$$\delta_n(\mathbf{x}) = \frac{\omega}{2\pi}\int_0^{2\pi/\omega} \tilde{\bar{\delta}}(\mathbf{x},t) \exp(-in\omega t), \quad n = 0, \pm1, \pm2, \ \ldots \ , \tag{5.9}$$

to examine the behavior of their Fourier components. In this way we can gain insight into the relative importance of nonlinear viscous effects and, therefore, into whether a linearized viscous analysis could be applied to provide meaningful and efficient unsteady viscous-layer solutions. Note that the lower limit on the integral in (5.8) must be changed to $-\infty$ if the wake displacement thickness is to be determined.

A series of calculations were performed for upstream and downstream acoustic excitations at the frequencies, ω, listed above and complex amplitudes, $p_{I,\pm\infty}$, of (0.1,0), (0.3,0), (0.5,0) and (0.75,0). In each case the steady Mach number is 0.5 and the Reynolds number, Re, is 10^6. The viscous-layer calculations were initiated at $(x,t) = (0.01,0)$, and the laminar flat-plate similarity solution was imposed as the initial condition in x and t. Also, the flows were assumed to undergo instantaneous transition from laminar to turbulent at $x = 0.02$.

The viscous-layer calculation was carried out using 51 uniformly stretched (with $K_\eta = 1.10$) points across each boundary layer, with $\Delta\eta = 0.0175$ at the blade surface. The wake grid consisted of 101 points across the viscous layer stretched in the same manner as for the surface boundary layers. A total of 25 uniform time steps were used per temporal period of the unsteady excitation. Two different axial or streamwise mesh distributions were used — one for the excitations originating upstream and one for those originating downstream. In each case the streamwise distribution was selected so that there were at least 20 mesh points per wave length, $2\pi/\kappa_{\xi,\mp\infty}$, for the highest frequency considered, i.e., $\omega = 10$.

For disturbances originating upstream, a variably spaced streamwise mesh was used with points clustered near the blade leading and trailing edges. The minimum streamwise spacing on the blade was $\Delta x \approx 0.0177$ at the blade edges, and the maximum was $\Delta x \approx 0.0611$ near mid-chord. The stretching used in the wake is identical to that used for the forward portion

of the blade, with $\Delta x \approx 0.0177$ in the first wake interval and monotonically increasing to $\Delta x \approx 0.11$ at the farthest downstream calculation point ($x = 2.0$). The resulting grid had 29 points on the blade surface and 20 points along the wake. For the downstream disturbances a nearly uniform grid was employed, with $\Delta x \approx 0.025$ on the blade and $0.025 \leq \Delta x \leq 0.030$ along the wake, where the grid was mildly stretched to distribute the points throughout the interval $x \in (1, 2]$. The resulting grid had 40 points along the blade and 36 points along the wake.

First, we consider the solution for an incident pressure disturbance from upstream with $p_{I,-\infty} = (0.5, 0)$, $\omega = 5$ and $\sigma = 0$ deg. The temporal means, δ_0, $\tau_{\omega,0}$ and $\tilde{U}_{\mathcal{L},0}$, and the magnitudes, $|\delta_n|$, $|\tau_{\omega,n}|$ and $|\tilde{U}_{\mathcal{L},n}|$, of the first two harmonics ($n = 1, 2$) of the displacement thickness, $\tilde{\bar{\delta}}$, surface shear stress, $\tilde{\bar{\tau}}_w$, and wake centerline velocity, $\tilde{U}_{\mathcal{L}}$, as determined by the unsteady viscous-layer solution, are presented in Figure 27 along with the corresponding steady ($|p_{I,-\infty}| \equiv 0$) results. The steady viscous solution has also been determined using the UNSVIS code, with the steady displacement thickness and surface shear stress given by

$$\bar{\delta}(\mathbf{x}) = \int_0^\infty [1 - \bar{\rho}U/(\bar{\rho}_e U_e)]dn \tag{5.10}$$

and $\bar{\tau}_w = (\mathrm{Re})^{-1}(\bar{\mu}\partial U/\partial n)_w$, where $\bar{\rho}$ and U are the density and streamwise velocity, respectively, in the steady background flow. The differences between the steady and the temporal mean values of the unsteady viscous quantities, and the amplitudes of the higher harmonic unsteady quantities provide a measure of the importance of nonlinear unsteady viscous effects.

The results in Figure 27 indicate that nonlinear effects are relatively unimportant in the unsteady flow driven by the prescribed upstream pressure excitation. However, similar results in Figure 28 for an acoustic disturbance originating downstream, with $p_{I,+\infty} = (0.5, 0)$, $\omega = 5$ and $\sigma = 0$, indicate that the nonlinear response of the viscous-layer displacement thickness can be quite significant. An unexpected result of the latter calculation is the predicted increase in the time-mean of the unsteady displacement thickness with increasing distance along the wake (i.e., as $x \to 2.0$). In an attempt to determine whether this effect is physical or numerical in origin, an unsteady viscous solution was calculated using a grid with twice as many uniformly distributed streamwise points. It was found that, although slightly less pronounced, this behavior was also present in the fine grid calculation.

The behavior of the zeroth- and first-harmonic components of the viscous parameters is illustrated in Figures 29 and 30 for upstream acoustic excitations with $p_{I,-\infty} = (0.5, 0)$, $\sigma = 0$, and $\omega = 1, 2, 5$ and 10. Similar results for downstream acoustic excitations are given in Figures 31 and 32. For the upstream case, the time-mean values and the magnitudes of the first-harmonic viscous-layer response quantities are relatively unaffected by changes in excitation frequency. In addition, the first-harmonic displacement thickness is essentially out-of-phase with the first-order velocity fluctuation, $\tilde{u}_e$, at the edge of the viscous layer, and the first-harmonic wall shear stress and wake centerline velocity are essentially in phase with the edge-velocity fluctuation. The corresponding results (Figures 31 and 32) for the downstream acoustic excitation show that frequency has a greater impact on the temporal mean and the first-harmonic amplitudes of the viscous quantities. In particular, the time-mean displacement thicknesses vary significantly with ω and indicate that nonlinear effects

are important at higher frequencies. As indicated in Figure 32, the first-harmonic displacement thicknesses lag the fluctuating component of the viscous-layer edge velocity by phase angles ranging from approximately -140 to -180 deg; the first-harmonic wall shear stresses lead this fluctuating velocity by angles ranging from 0 to 40 deg; and the minimum wake-streamwise velocities are approximately in-phase with the wake-edge velocity fluctuation.

As a final illustration, we consider the response of the viscous layer to different amplitudes of acoustic excitation. In particular, numerical results are presented in Figures 33 and 34 for excitations at $\omega = 5$, $\sigma = 0$ and $p_{I,\mp\infty} = (0.1,0)$, $(0.3,0)$, $(0.5,0)$ and $(0.75,0)$. For disturbances from upstream the effect of unsteadiness on the time-mean values of $\tilde{\tilde{\delta}}$ and $\tilde{\tilde{\tau}}_\omega$ is small, except for the highest disturbance amplitude, $|p_{I,-\infty}| = 0.75$, considered. The effect on the time-mean wake centerline velocity is negligible. The results for the acoustic excitations from downstream in Figure 34 once again indicate that such disturbances produce much stronger nonlinear viscous-layer responses, particularly in the displacement thickness. For both the upstream and downstream acoustic excitations, the phase angles (not shown) of the first-harmonic viscous quantities relative to the edge velocity fluctuation are almost independent of the excitation amplitude.

The foregoing results indicate that the viscous-layer response parameters $\tilde{\tilde{\delta}}$, $\tilde{\tilde{\tau}}_\omega$ and $\tilde{U}_{\mathcal{Q}}$ behave essentially in a linear manner for acoustic excitations originating upstream of the blade row. For excitations originating downstream, nonlinear effects can be significant at high temporal frequencies (say $\omega \geq 5$) and/or high excitation amplitudes ($|p_{I,+\infty}| > 0.5$). For $M = 0.5$ the magnitude of the axial wave number for a pressure excitation from downstream is three times that for an excitation from upstream. This produces a corresponding ratio in the magnitudes of the pressure gradients that drive the viscous solution, and is perhaps responsible for the nonlinear response of the viscous layer to downstream disturbances. Another factor is the direction of propagation of the acoustic excitation. We have performed a series of calculations to isolate these effects and have found the latter, i.e., direction of propagation, to be the dominant factor in promoting a nonlinear response in the viscous layer.

The detected behavior of the displacement thickness in the far wake, i.e., increasing with increasing x, for high frequency or high amplitude downstream disturbances is a somewhat disturbing aspect of the present unsteady viscous solutions. A series of laminar calculations were performed, and the results showed a similar behavior. Thus, the increase in displacement thickness in the far wake ($x \rightarrow 2$) cannot be attributed to the turbulence model used in the present viscous analysis.

Turbine Cascade

In order to demonstrate the coupled LINFLO/UNSVIS weak inviscid/viscid interaction solution capability, we consider an unsteady flow through the turbine cascade of § 5.1. This flow occurs at a Reynolds number, Re, of 5.0×10^5, an inlet Mach number, $M_{-\infty}$, of 0.19 and an inlet flow angle, $\Omega_{-\infty}$ of 45 deg. The unsteadiness is excited by a pressure disturbance from upstream, characterized by $p_{I,-\infty} = (0.35,0)$, $\kappa_{\eta,-\infty} = \sigma/G = 0$ and $\omega = 1.0$. The inviscid steady Mach number field and Mach number distribution along a blade surface are shown in Figure 16. For this example the unsteady pressure is essentially in-phase with the upstream acoustic excitation; the in-phase component of the unsteady pressure field is

depicted in Figure 35. The pressure excitation produces a superresonant (1,1) response. Therefore, the pressure contours in Figure 35 indicate a much higher pressure amplitude at the upstream boundary than that due to the acoustic excitation alone. The temporal mean and the upper and lower bounds (envelope) for the inviscid surface velocity are shown in Figure 36. The first-harmonic surface velocity, as determined by the input value of $p_{I,-\infty}$, is of relatively small amplitude for this case. However, for pressure excitations at higher amplitude, the viscous-layer separates on the blade suction surface just upstream of the trailing edge, thereby precluding a continuation of the unsteady viscous calculation into the wake.

Since the turbine blade has a blunt leading edge, the unsteady stagnation-point analysis, described in § 4.3, was applied at each time step to provide the upstream velocity profiles needed to advance the viscous-layer solutions along the blade suction and pressure surfaces. For this case, the unsteady stagnation point motion is confined to a small interval of length $2|\tau_I| \approx 0.0037$. A series of representative velocity profiles for the periodic flow within the stagnation region at four different times (i.e., $t = \pi/2, \pi, 3\pi/2$ and 2π) are shown in Figures 37 and 38. Here the instantaneous streamwise-velocity profiles are presented in the body-fixed frame of reference, and the abscissa on each plot refers to the location on the blade surface at which the velocity profile is determined. The interval shown in Figure 37 is centered about the mean location of the stagnation point; that in Figure 38, about the instantaneous location, i.e., the location at which $\tilde{U}_e = 0$ in the body-fixed frame of reference. Note that the velocity profiles are shown over a much narrower interval, $[-0.02|\tau_I|, 0.02|\tau_I|]$, in Figure 38, where the profiles indicate that reverse flow occurs in the immediate vicinity of the instantaneous stagnation point location.

The viscous-layer calculation for the reference turbine blade and its wake was performed assuming that instantaneous transition from laminar to turbulent flow occurs at $\tau/\tau_{te} = 0.05$ on both the pressure and suction surfaces of the blade. Here, τ is the distance along the blade surfaces measured from the mean leading-edge stagnation point location, and the subscript te refers to the values of τ at the blade trailing edge. The grid used in this calculation had 77 points along the blade surface and 54 points along the reference wake streamline. It is a stretched grid with $\Delta\tau \approx 0.002$ at the farthest upstream point and $\Delta\tau \approx 0.0001$ at the trailing edge. The largest value of $\Delta\tau$ on the blade, i.e., 0.052, occurs near midchord. The streamwise intervals grow aft of the trailing edge from $\Delta\tau \approx 0.0001$ to approximately 0.083 one chord length downstream of the blade row. This distribution ensures that there are at least 20 points per streamwise wavelength of the unsteady excitation. The viscous-layer calculation was carried out using 71 uniformly stretched points across each boundary layer, with $K_\eta = 1.045$ and $\Delta\eta = 0.04$ at the blade surface. The wake grid consisted of 141 points across the viscous layer stretched in the same manner as on the blade surface. A total of 40 uniform time steps were used per temporal period of the unsteady excitation.

Results of the unsteady viscous-layer calculation are shown in Figures 39 through 41. Temporal mean values and upper and lower bounds for the displacement thickness and wall shear stress along the upper and lower surfaces of the reference turbine blade are shown in Figure 39; corresponding results for the wake displacement thickness and minimum streamwise velocity, in Figure 40. Here, the upper and lower bounds of a viscous-layer response

quantity, say the displacement thickness, are defined as

$$\tilde{\tilde{\delta}}^{\pm} = \delta_0 \pm 2 \sum_{n=1}^{\infty} |\delta_n| \,, \tag{5.11}$$

and $\tilde{\tilde{\delta}}_W$ is the displacement thickness of the complete wake. Wake velocity profiles at four different instants of time are depicted in Figure 41. The unsteady response of the viscous layer is essentially linear for this example, i.e., the temporal mean and the steady viscous solutions are almost identical, and the Fourier amplitudes of the higher ($n > 2$) harmonic components of $\tilde{\tilde{\delta}}$, $\tilde{\tilde{\tau}}_\omega$ and $\tilde{U}_{W_{\min}}$ are negligible.

The foregoing results demonstrate the new capabilities that have been added to the UNSVIS code, i.e., an unsteady stagnation region analysis and a modified unsteady wake analysis. These results also demonstrate the present weak inviscid/viscid interaction prediction capability that results from a sequential coupling of a linearized unsteady inviscid solution, determined using LINFLO, and a nonlinear unsteady viscous-layer solution. Unfortunately, since boundary-layer separation usually occurs in realistic configurations, and a weak interaction analysis breaks down in such cases, a weak interaction analysis has a limited range of application. This is particularly true for compressor cascades where, because of adverse mean pressure gradients, separation occurs near the blade leading edges. There is an important need, therefore, to develop a simultaneous coupling (or strong interaction) solution procedure for separated unsteady cascade flows.

6. Concluding Remarks

Linearized inviscid and nonlinear viscous-layer unsteady aerodynamic analyses and codes have been developed for predicting subsonic unsteady flows through isolated, two-dimensional blade rows. The inviscid analysis can be applied to predict the aerodynamic response to structural (i.e., blade motions) and external aerodynamic (entropic, vortical, and acoustic) excitations. It provides very efficient response predictions for realistic cascade configurations, and should therefore be useful for turbomachinery aeroelastic and aeroacoustic design applications. The viscous analysis can be applied to predict the viscous-layer response that arises from imposed inviscid conditions at the blade and wake surfaces. At present only a weak or sequential coupling of the inviscid and viscous-layer solutions has been considered. The development of a strong inviscid/viscid interaction analysis involving a simultaneous coupling of the inviscid and viscous solutions is planned as future work.

Under the present phase of this overall research effort a composite (global/local) mesh analysis has been developed for determining the linearized unsteady velocity potential. The composite-mesh capability allows a great deal of flexibility in prescribing a suitable mesh for the accurate resolution of an unsteady cascade flow, and this type of capability will be essential for analyzing gust encounters in unsteady transonic flows with moving shocks. However, based on the parametric studies reported herein, a global-mesh analysis appears to be quite adequate for analyzing low speed flows, provided that a sufficiently dense mesh is employed. Moreover, a global mesh analysis requires only about one-fourth of the CPU time needed for a composite analysis. Also, under the present effort, an existing unsteady viscous layer analysis has been extended by incorporating a similarity analysis for the flow in the vicinity of a moving stagnation point, and by properly accounting for the jumps in the inviscid flow variables across vortex-sheet unsteady wakes.

The linearized inviscid (LINFLO) and nonlinear viscous-layer (UNSVIS) analyses have been demonstrated via application to compressor, turbine and flat-plate blade rows. The numerical results indicate that mean-flow nonuniformity has an important impact on the pressure responses of cascades subjected to vortical excitations. In particular, high wave number vortical gusts produce pressure responses in real blade configurations that differ substantially from those occurring in corresponding flat plate configurations. The viscous-layer analysis has been applied to unstaggered flat plate and to turbine cascades subjected to acoustic excitations coming from upstream or downstream and traveling in the axial direction. The flat-plate example is, perhaps, the simplest unsteady cascade problem that can be analyzed, both because of the geometric simplicity and because the unsteady pressure is nonsingular at the flat-plate leading edges. The numerical results indicate that the viscous layer responds linearly, for the most part, to acoustic excitations from upstream, but significant nonlinear response components occur for downstream excitations at high temporal frequency and/or high amplitude, which travel against the mainstream velocity. The numerical results for the turbine demonstrate the present weak inviscid/viscid interaction solution capability for a realistic cascade configuration.

Because of boundary-layer separation the range of application of a weak inviscid/viscid interaction analysis is severely limited. For example, the mean pressure rise produced by a compressor blade row typically causes boundary-layer separation very near the blade leading

edges, thereby precluding a continuation of a direct viscous-layer calculation along the blade and into the wake. Thus, the development of a strong inviscid/viscid interaction analysis will be needed so that the effects of viscous displacement on the unsteady pressure response can be included in aeroelastic and aeroacoustic design calculations. The linearized inviscid response to high wave number gusts, and the linear vs nonlinear response of viscous layers to entropic, vortical and blade-motion excitations are other issues that will require further study and clarification.

References

[1] Whitehead, D. S., "Classical Two-Dimensional Methods," chapter III in *AGARD Manual on Aeroelasticity in Axial-Flow Turbomachines*, Vol. 1, *Unsteady Turbomachinery Aerodynamics*, edited by M. F. Platzer and F. O. Carta, AGARD-AG-298, March 1987.

[2] Verdon, J. M. and Caspar, J. R., "A Linearized Unsteady Aerodynamic Analysis for Transonic Cascades," *Journal of Fluid Mechanics*, Vol. 149, December 1984, pp. 403–429.

[3] Whitehead, D. S. and Newton, S. G., "A Finite Element Method for the Solution of Two-Dimensional Transonic Flows in Cascades," *International Journal for Numerical Methods in Fluids*, Vol. 5, No. 2, February 1985, pp. 115–132.

[4] Hall, K. C. and Crawley, E. F., "Calculation of Unsteady Flows in Turbomachinery Using the Linearized Euler Equations," *AIAA Journal*, Vol. 27, No. 6, June, 1989, pp. 777–787.

[5] Whitehead, D. S., "A Finite Element Solution of Unsteady Two-Dimensional Flow in Cascades", *International Journal for Numerical Methods in Fluids*, Vol. 10, January 1990, pp. 13–34.

[6] Verdon, J. M., "Unsteady Aerodynamics for Turbomachinery Aeroelastic Applications", in *Unsteady Transonic Aerodynamics*, edited by D. Nixon, *Progress in Astronautics and Aeronautics*, Vol. 120, American Institute of Aeronautics and Astronautics, Washington, D. C., 1989, pp. 287–347.

[7] Verdon, J. M., "Linearized Unsteady Aerodynamics for Turbomachinery Aeroelastic Applications", Paper No. 90–2355, AIAA/SAE/ASME/ASEE 26th Joint Propulsion Conference, Orlando, Florida, July 16–18, 1990.

[8] Goldstein, M. E., "Unsteady Vortical and Entropic Distortions of Potential Flows Round Arbitrary Obstacles," *Journal of Fluid Mechanics*, Vol. 89, Part 3, December 1978, pp. 433–468.

[9] Goldstein, M. E., "Turbulence Generated by the Interaction of Entropy Fluctuations with Non-uniform Mean Flows," *Journal of Fluid Mechanics*, Vol. 93, Part 2, July 1979, pp. 209–224.

[10] Atassi, H. M. and Grzedzinski, J., "Unsteady Disturbances of Streaming Motions around Bodies," *Journal of Fluid Mechanics*, Vol. 209, December 1989, pp. 385–403.

[11] Usab, W. J., Jr. and Verdon, J. M., "Advances in the Numerical Analysis of Linearized Unsteady Cascade Flows," ASME Paper 90–GT–11, presented at the International Gas Turbine and Aeroengine Congress and Exposition, Brussels, Belgium, June 11–14, 1990, to be published in the *Transactions of the ASME*.

[12] Hall, K. C. and Verdon, J. M., "Gust Response Analysis for Cascades Operating in Nonuniform Mean Flows," presented at AGARD Specialists meeting on Unsteady Aerodynamic Phenomena in Turbomachines, Luxembourg, August 28–30, 1989, Paper No. 10 in AGARD–CP–468, February, 1990, to be published in the *AIAA Journal.*

[13] Power, G. D., Verdon, J. M. and Kousen, K. A., "Analysis of Unsteady Compressible Viscous Layers", ASME Paper No. 90–GT–14,35th International Gas Turbine and Aeroengine Congress and Exposition, Brussels, Belgium, June 10–14, 1990, to be published in *Trans. of the ASME*

[14] Dring, R. P., Joslyn, H. D. Hardin, L. W., and Wagner, J. H., "Turbine Rotor-Stator Interaction," *Transactions of the ASME, A: Journal of Engineering for Power*, Vol. 104, No. 4, October 1982, pp. 729–742.

[15] Dring, R. P., Blair, M. F., Joslyn, H. D., Power, G. D., and Verdon, J. M., "The Effects of Inlet Turbulence and Rotor/Stator Interactions in the Aerodynamics and Heat Transfer of a Large-Scale Rotating Model," Vol. I — Final Report, NASA CR 4079, June 30, 1989.

[16] Verdon, J. M. and Hall, K. C., "Development of a Linearized Unsteady Aerodynamic Analysis for Cascade Gust Response Predictions", CR 4308, prepared under Contract NAS3–25425 for NASA Lewis Research Center, Cleveland, Ohio, July 1990.

[17] Verdon, J. M., "The Unsteady Flow in the Far Field of an Isolated Blade Row," *Journal of Fluids and Structures*, Vol. 3, No. 2, March 1989, pp. 123–149.

[18] Caspar, J. R., "Unconditionally Stable Calculation of Transonic Potential Flow Through Cascades Using an Adaptive Mesh for Shock Capture," *Trans. ASME A: Journal of Engineering for Power*, Vol. 105, No. 3, July 1983, pp. 504–513.

[19] Verdon, J. M., "Linearized Unsteady Aerodynamic Theory," chapter II in *AGARD Manual on Aeroelasticity in Axial Flow Turbomachines*, Vol. 1, Unsteady Turbomachinery Aerodynamics, edited by M. F. Platzer and F. O. Carta, AGARD–AG–298, March 1987.

[20] Caspar, J. R. and Verdon, J. M., "Numerical Treatment of Unsteady Subsonic Flow Past an Oscillating Cascade," *AIAA Journal*, Vol. 19, No. 12, December 1981, pp. 1531–1539.

[21] Verdon, J. M. and Caspar, J. R., "Development of a Linear Unsteady Aerodynamic Analysis for Finite-deflection Subsonic Cascades," *AIAA Journal*, Vol. 20, No. 9, September 1982, pp. 1259–1267.

[22] Verdon, J. M., "The Unsteady Aerodynamic Response to Arbitrary Modes of Blade Motion," *Journal of Fluids and Structures*, Vol. 3, No. 3, May 1989, pp. 255–274.

[23] Williams, M. H., "Linearization of Unsteady Transonic Flows Containing Shocks," *AIAA Journal*, Vol. 17, No. 4, April 1979, pp. 394–397.

[24] Schlichting, H., *Boundary Layer Theory*, McGraw Hill Book Company, Inc., New York, 1960, p. 339.

[25] Cebeci, T. and Smith, A. M. O., *Analysis of Turbulent Boundary Layers*, New York, 1974, pp 211–239.

[26] Dhawan, S. and Narashima, R., "Some Properties of Boundary-Layer Flow During the Transition from Laminar to Turbulent Motion", *Journal of Fluid Mechanics*, Vol. 3, 1958.

[27] Chang, K. C., Bui, M. N., Cebeci, T. and Whitelaw, J. H., "The Calculation of Turbulent Wakes," *AIAA Journal*, Vol. 24, February 1986, pp. 200–201.

[28] Yuhas, L. J., *An Optimization Technique for the Development of a Two-Dimensional Turbulent Boundary Layer Model*, MS thesis Lehigh University, 1981.

[29] Blottner, F. G., "Finite Difference Method of Solution of the Boundary-Layer Equations", *AIAA Journal*, Vol. 18, February 1970, pp.193–205.

[30] Werle, M. J. and Verdon, J. M., "Viscid/Inviscid Interaction Analysis for Symmetric Trailing Edges," UTRC Report R79–914493–5, East Hartford, CT, prepared under Contract N00019–78–C–0604 for the Naval Air Systems Command January 1980.

[31] Rott, N., "Unsteady Viscous Flow in the Vicinity of a Stagnation Point," *Quarterly Journal of Applied Mathematics*, Vol. 13, 1956, pp. 444–451.

[32] Glauert, M. B., "The Laminar Boundary Layer on Oscillating Plates and Cylinders," *Journal of Fluid Mechanics*, Vol. 1, 1956, pp. 97–110.

[33] White, F. M., *Viscous Fluid Flow*, McGraw-Hill, Inc., New York, 1974, p. 596.

[34] Fransson, T. H. and Suter, P., "Two-Dimensional and Quasi Three-Dimensional Experimental Standard Configurations for Aeroelastic Investigations in Turbomachine-Cascades," Report LTA–TM–83–2, Ecole Polytechnique Federale de Lausanne, Lausanne, Switzerland, 1983.

[35] Smith, S. N., "Discrete Frequency Sound Generation in Axial Flow Turbomachines," British Aeronautical Research Council, R&M 3709, London, UK, 1971.

List of Symbols

All physical parameters listed below are dimensionless. Lengths have been scaled with respect to blade chord, time with respect to the ratio of blade chord to upstream freestream flow speed, density and viscosity with respect to their upstream freestream values, respectively, velocity with respect to the upstream freestream flow speed, normal and shear stresses with respect to the product of the upstream freestream density and the square of the upstream freestream flow speed, temperature with respect to the square of the upstream freestream speed divided by the fluid specific heat at constant pressure, and entropy with respect to the fluid specific heat at constant pressure. The number(s) in parentheses at the end of each symbol description indicates an equation in which the symbol appears.

Roman

$\mathcal{A}_\infty$	Constant vector , (3.23).
$\tilde{A}_T$	Inner region turbulence model parameter, (4.11).
A	Speed of sound propagation in steady background flow, (3.7).
a_0	Constant, (3.26).
$\mathcal{B}$	Moving blade surface.
B	Blade mean position, (3.28).
$b,\ c$	Stagnation-region constants, (4.42), (4.49).
$d\boldsymbol{\tau}$	Differential vector tangent to path of integration, (3.20).
$d\tau_\Psi$	Differential element of arc length along a streamline, (3.19).
$\mathbf{e}$	Unit vector, (3.18).
$\mathcal{F},\ \mathcal{V},\ \mathcal{G}$	Dependent variables in Levy-Lees transformation, (4.18).
F	Complex function of mean-flow stream function, (3.26).
f, g	Dependent similarity variables for stagnation region, (4.31).
$\mathbf{G}$	Cascade gap vector ($= G\mathbf{e}_\eta$), Figure 1.
$\tilde{H}$	Total enthalpy, (3.48).
H	Total enthalpy in steady background flow, (3.37).

$\tilde{h}$	First-order unsteady total enthalpy, (3.41).
h'	Turbulent total enthalpy fluctuation, (4.3).
i	Imaginary unit, (2.1).
$K_\xi,\ K_\eta$	Grid stretching factors used in viscous-layer calculations, (4.50), (4.51).
$l,\ \hat{l}$	Functions appearing in viscous region similarity equations, (4.22), (4.34).
M	Mach number in steady background flow, (3.7).
m	Blade number index, Figure 1; complex amplitude of first-harmonic unsteady aerodynamic moment about midchord, Figure 14.
$\mathbf{n}$	Unit normal vector, (3.3).
$\tilde{P}$	Pressure, (3.36).
P	Pressure in steady background flow, (3.7).
Pr, Pr_T	Prandtl number, turbulent Prandtl number, (4.3), (4.6).
$\tilde{P}^+$	Inner region turbulence model parameter, (4.11).
$\tilde{p}$	First-order unsteady pressure, Equation (3.40).
p	Complex amplitude of first-harmonic unsteady pressure, (2.4).
$\bar{Q},\ \tilde{Q}$	Functions associated with Levy-Lees transformation, (4.17), (4.19).
$\tilde{Q}_w$	Surface heat flux, (4.8).
$\mathcal{R}$	Surface (blade, wake or shock) displacement vector, (2.1).
Re	Reynolds number, (4.2).
Re_θ	Reynolds number based on viscous-layer momentum thickness, (4.32).
$\mathbf{r}$	Complex amplitude of surface (blade, wake or shock) displacement vector, (2.1).
r_τ	Flat-plate displacement tangential to surface, (4.30).

$\mathcal{S}h$	Moving shock surface.
Sh	Shock mean position, (3.30)
$\tilde{s}$	First-order unsteady entropy, (3.39).
s	Complex amplitude of first-harmonic unsteady entropy, (2.2).
$\tilde{T}$	Temperature, (4.4).
T	Temperature in steady background flow, (3.7).
T_C	Temperature constant used in Sutherland's law, (4.5).
$\tilde{t}$	First-order unsteady temperature, (3.40).
t	Time, (2.1).
$\tilde{U}$, $\tilde{V}$	Unsteady velocity components along and normal to a moving blade surface or reference wake streamline, (4.1).
$\tilde{U}_{\mathcal{C}}$	Wake centerline velocity, Figure 26.
$U_{\mathcal{C}}$	Wake centerline velocity in steady background flow, Figure 26.
$U_{\mathcal{C},n}$	Fourier component of unsteady wake centerline velocity, Figure 26.
u', v'	Streamwise and normal components of turbulent velocity fluctuation, (4.2).
$\tilde{\mathbf{V}}$	Velocity, (3.1).
$\mathbf{V}$	Velocity in steady background flow, (3.1).
$\tilde{\mathbf{v}}$	First-order unsteady velocity, (3.4).
$\mathbf{v}$	Complex amplitude of first-harmonic unsteady velocity, (3.5).
$\mathbf{v}_R$	Complex amplitude of first-harmonic rotational unsteady velocity, (3.8).
$\mathbf{v}_*$	Complex amplitude of first-harmonic source-term unsteady velocity, (3.8).
$\mathbf{v}'$	Turbulent velocity fluctuation, (4.14).

$\mathcal{W}$	Moving wake surface.
W	Wake mean position, (3.29).
$\mathbf{X}$	Lagrangian coordinate vector, (3.18).
$\mathbf{x}$	Position vector, (2.1).
x, y	Cartesian coordinates along and normal to mean position of blade chord, Figure 1.
Y^+	Reynolds number based on friction velocity and normal distance from blade.

Greek

$\alpha_1, \ldots, \alpha_6$	Coefficient functions in Levy-Lees equations, (4.22).
$\beta_{\mp\infty}$	Acoustic attenuation constant, (2.4).
γ	Fluid specific heat ratio, (3.7).
γ_{tr}	Turbulence intermittency factor, (4.15).
Δ	Drift function, (3.19).
Δp	Complex amplitude of first-harmonic unsteady pressure difference (lower surface − upper surface) acting on reference ($m = 0$) blade, Figure 7.
$\Delta\xi,\ \Delta\eta$	Mesh spacings, (4.50), (4.51).
$\tilde{\bar{\delta}}$	Viscous-layer displacement thickness, (5.8).
$\bar{\delta}$	Viscous-layer displacement thickness in steady background flow, (5.11).
δ_n	Fourier component of viscous-layer displacement thickness, (5.8).
ϵ	Small parameter ($\ll 1$); Turbulent eddy viscosity, (4.6).
$\bar{\epsilon}$	Turbulent eddy viscosity in steady background flow, (4.22).
$\epsilon_{\tilde{H}}$	Turbulent eddy diffusivity, (4.6).
$\tilde{\boldsymbol{\zeta}}$	First-order unsteady vorticity, (2.3).

$\boldsymbol{\zeta}$	Complex amplitude of first-harmonic unsteady vorticity, (3.24).
Θ	Cascade stagger angle, Figure 1.
$\theta,\ \lambda$	Dependent similarity variables, (4.32), (4.42).
$\boldsymbol{\kappa}$	Wave number vector, (2.2).
$\tilde{\bar{\mu}}$	Molecular viscosity, (4.5).
$\bar{\mu}$	Molecular viscosity in steady background flow, (4.22).
$\xi,\ \eta$	Cascade axial and "circumferential" Cartesian coordinates, Figure 1; independent similarity variables, (4.17), (4.33).
$\tilde{\bar{\rho}}$	Density, (4.1).
$\bar{\rho}$	Density in steady background flow, (3.6).
$\tilde{\rho}$	First-order unsteady density, (3.40).
σ	Interblade phase angle, (3.5).
$\boldsymbol{\tau}$	Unit tangent vector, (3.3).
$\tilde{\bar{\tau}}_w$	Surface shear stress.
$\bar{\tau}_w$	Surface shear stress in steady background flow, Figure 26.
$\tau_{w,n}$	Fourier component of surface shear stress, Figure 26.
$\tau,\ n$	Viscous-layer coordinates along and normal to blade surface and reference wake streamline, (4.1).
Φ	Velocity potential for inviscid steady background flow, (3.6).
$\tilde{\phi}$	Velocity potential for first-order inviscid unsteady flow, (3.40).
ϕ	Complex amplitude of first-harmonic unsteady velocity potential, (3.11).
ϕ_*	Complex amplitude of first-harmonic convected potential, (3.25).
$\phi_{\tilde{\delta}_1}$, $\phi_{\tilde{\tau}_{w,1}}$, $\phi_{\tilde{u}_{\mathcal{L},1}}$, & $\phi_{\tilde{u}_e}$	Phase angles of the first-harmonic displacement thickness, wall shear stress, wake centerline velocity, and viscous-layer edge velocity, Figure 29.

χ, χ_0	Outer region turbulence model parameters, (4.13), (4.14).
Ψ	Stream function for inviscid steady background flow, (3.20).
Ω	Steady flow angle, Figure 1.
ω	Temporal frequency, (3.4).

Mathematical

$\tilde{D}/Dt$	Convective derivative operator, (4.2).
$\bar{D}/Dt$	Convective derivative operator based on mean-flow velocity, (3.9), (3.40).
Im{ }	Imaginary part of { }, Figure 7.
Re{ }	Real part of { }, (2.1), Figure 7.
∇	Gradient operator, (3.6).
[ ]	Change in a flow quantity across a surface of discontinuity, (3.29).

Subscripts

B	Reference blade surface, (2.1).
$\mathfrak{C}\!\!\mathfrak{L}$	Wake centerline, Figure 27.
E, R	Acoustic excitation, response, (2.1).
e	Edge of viscous layer, (4.7).
I	Incident pressure or irrotational velocity disturbance, (2.4); initial τ-station for viscous-layer calculation, (4.49).
i, o	Inner, outer turbulent regions, (4.10), (4.12).
l, n	Integer indices.
m	Blade number index, Figure 1.
N, T, z, η and ξ	Indicates direction: N — normal to inlet freestream direction, (3.18), T — parallel to inlet freestream direction, (3.18), z — out from the page, (3.20), η — cascade "circumferential" direction, (3.31), and ξ — cascade axial direction, (3.33).

$\mathcal{S}$	Moving blade, wake or shock surface, (3.2).
S	Mean position of blade, wake or shock surface, (3.2); stagnation region variable, (4.28).
$\mathcal{S}h_{m,n}$	Moving shock surface, (3.36).
te	Blade trailing edge, (4.16).
$\mathcal{W}$, $\mathcal{W}_{\min}$	Wake value, (4.24); minimum wake value, Figure 39.
w	Wall, i.e., blade surface, value, (4.8).
$-$, $+$	Axial locations at finite distance upstream and downstream from blade row, (2.4); point of intersection (ξ_-, η_-) of axial line $\xi = \xi_-$ and reference blade stagnation streamline, (3.20).
$\mp\infty$	Far upstream/downstream freestream value of a steady flow variable, Figure 1; far upstream/downstream value of an unsteady flow variable, (2.4).

Superscripts

$'$	Turbulent fluctuation, (4.2).
$+$, $-$	Upper, lower viscous layer, (4.24).
$\overline{}$	Steady background flow quantity, (3.11).
$\overline{\overline{}}$	Turbulent correlation, (4.2).
$\sim$	Time-dependent flow variable, (3.1), (3.4).

List of Figures

Figure 17. Drift and stream contours for steady flow at $M_{-\infty} = 0.19$ and $\Omega_{-\infty} = 45$ deg through the turbine cascade.

Figure 18. Contours of the in-phase component of the unsteady vorticity for the turbine cascade subjected to vortical gusts with $\mathbf{v}_{R,-\infty} \cdot \mathbf{e}_N = (1,0)$ and $\omega = 5$.

Figure 19. Contours of the in-phase component of the source term for the turbine cascade subjected to vortical gusts with $\mathbf{v}_{R,-\infty} \cdot \mathbf{e}_N = (1,0)$ and $\omega = 5$.

Figure 20. Contours of the in-phase component of the unsteady pressure for the turbine cascade subjected to vortical gusts with $\mathbf{v}_{R,-\infty} \cdot \mathbf{e}_N = (1,0)$ and $\omega = 5$.

Figure 21. Unsteady pressure-difference response of the turbine and corresponding flat-plate cascades subjected to a vortical gust with $\mathbf{v}_{R,-\infty} \cdot \mathbf{e}_N = (1,0)$, $\omega = 5$ and $\sigma = -\pi$.

Figure 22. Unsteady pressure-difference response of the turbine and corresponding flat-plate cascades subjected to a vortical gust with $\mathbf{v}_{R,-\infty} \cdot \mathbf{e}_N = (1,0)$, $\omega = 5$ and $\sigma = -2\pi$.

Figure 23. Unsteady pressure-difference response of the turbine and corresponding flat-plate cascades subjected to a vortical gust with $\mathbf{v}_{R,-\infty} \cdot \mathbf{e}_N = (1,0)$, $\omega = 5$ and $\sigma = -3\pi$.

Figure 24. Unsteady moment vs interblade phase angle for the turbine and corresponding flat-plate cascades subjected to vortical gusts with $\mathbf{v}_{R,-\infty} \cdot \mathbf{e}_N = (1,0)$ and $\omega = 5$.

Figure 25. Unsteady pressure distributions along blade and wake for an unstaggered flat-plate cascade ($\Omega = \Theta = 0$ deg, $M_{-\infty} = 0.5$ and $G = 1$) subjected to a unit-amplitude, $|p_{I,-\infty}| = 1$, pressure excitation from upstream with $\kappa_{\eta,-\infty} = \sigma G^{-1} = 0$.

Figure 26. Unsteady pressure distributions along blade and wake for an unstaggered flat-plate cascade ($\Omega = \Theta = 0$ deg, $M_{-\infty} = 0.5$ and $G = 1$) subjected to a unit-amplitude, $|p_{I,+\infty}| = 1$, pressure excitation from downstream with $\kappa_{\eta,+\infty} = \sigma G^{-1} = 0$.

Figure 27. Temporal mean and Fourier magnitudes of the displacement thickness, $\tilde{\bar{\delta}}$, wall shear stress, $\tilde{\bar{\tau}}_\omega$, and wake centerline velocity, $\tilde{U}_{\mathcal{L}}$, for turbulent flow through an unstaggered flat-plate cascade ($\Omega = \Theta = 0$ deg, $G = 1$, $M = 0.5$ and $\mathrm{Re} = 10^6$) subjected to an incident pressure disturbance from upstream with $p_{I,-\infty} = (0.5, 0)$, $\omega = 5$ and $\sigma = 0$ deg.

Figure 28. Temporal mean and Fourier magnitudes of the displacement thickness, $\tilde{\bar{\delta}}$, wall shear stress, $\tilde{\bar{\tau}}_\omega$, and wake centerline velocity, $\tilde{U}_{\mathcal{L}}$, for turbulent flow through an unstaggered flat-plate cascade ($\Omega = \Theta = 0$ deg, $G = 1$, $M = 0.5$ and $\mathrm{Re} = 10^6$) subjected to an incident pressure disturbance from downstream with $p_{I,+\infty} = (0.5, 0)$, $\omega = 5$ and $\sigma = 0$ deg.

Figure 29. Fourier amplitudes of $\tilde{\bar{\delta}}$, $\tilde{\bar{\tau}}_\omega$ and $\tilde{U}_{\mathcal{L}}$ for an unstaggered flat-plate cascade ($\Omega = \Theta = 0$ deg, $G = 1$, $M = 0.5$ and $\mathrm{Re} = 10^6$) subjected to pressure excitations from upstream with $p_{I,-\infty} = (0.5, 0)$ and $\sigma = 0$ deg.

Figure 30. Relative phase angles of first-harmonic displacement thickness, wall shear stress, and wake centerline velocity for an unstaggered flat-plate cascade ($\Omega = \Theta = 0$ deg, $G = 1$,

$M = 0.5$ and $\mathrm{Re} = 10^6$) subjected to pressure excitations from upstream with $p_{I,-\infty} = (0.5, 0)$ and $\sigma = 0\,\mathrm{deg}$.

Figure 31. Fourier amplitudes of $\tilde{\bar{\delta}}$, $\tilde{\bar{\tau}}_\omega$ and $\tilde{U}_{\mathcal{L}}$ for an unstaggered flat-plate cascade ($\Omega = \Theta = 0\,\mathrm{deg}$, $G = 1$, $M = 0.5$ and $\mathrm{Re} = 10^6$) subjected to pressure excitations from downstream with $p_{I,+\infty} = (0.5, 0)$ and $\sigma = 0\,\mathrm{deg}$.

Figure 32. Relative phase angles of first-harmonic displacement thickness, wall shear stress, and wake centerline velocity for an unstaggered flat-plate cascade ($\Omega = \Theta = 0\,\mathrm{deg}$, $G = 1$, $M = 0.5$ and $\mathrm{Re} = 10^6$) subjected to pressure excitations from downstream with $p_{I,+\infty} = (0.5, 0)$ and $\sigma = 0\,\mathrm{deg}$.

Figure 33. Fourier amplitudes of $\tilde{\bar{\delta}}$, $\tilde{\bar{\tau}}_\omega$ and $\tilde{U}_{\mathcal{L}}$ vs amplitude, $|p_{I,-\infty}|$, for an acoustic excitation from upstream with, $\omega = 5$ and $\sigma = 0\,\mathrm{deg}$, interacting with an unstaggered flat-plate cascade ($\Omega = \Theta = 0\,\mathrm{deg}$, $G = 1$, $M = 0.5$ and $\mathrm{Re} = 10^6$).

Figure 34. Fourier amplitudes of $\tilde{\bar{\delta}}$, $\tilde{\bar{\tau}}_\omega$ and $\tilde{U}_{\mathcal{L}}$ vs amplitude, $|p_{I,+\infty}|$, for an acoustic excitation from downstream with, $\omega = 5$ and $\sigma = 0\,\mathrm{deg}$, interacting with an unstaggered flat-plate cascade ($\Omega = \Theta = 0\,\mathrm{deg}$, $G = 1$, $M = 0.5$ and $\mathrm{Re} = 10^6$).

Figure 35. Contours of the in-phase component of the unsteady pressure for the turbine cascade subjected to a pressure excitation from upstream with $p_{I,-\infty} = (0.35, 0)$, $\omega = 1$ and $\sigma = 0$.

Figure 36. Temporal mean values and upper and lower bounds of the inviscid surface (viscous-layer edge) velocity for the turbine cascade subjected to an upstream pressure excitation with $p_{I,-\infty} = (0.35, 0)$, $\omega = 1$ and $\sigma = 0$.

Figure 37. Velocity profiles in the neighborhood of a mean stagnation point location for the turbine cascade subjected to an upstream acoustic excitation with $p_{I,-\infty} = (0.35, 0)$, $\omega = 1$ and $\sigma = 0$: (a) $t = \pi/2$; (b) $t = \pi$; (c) $t = 3\pi/2$; (d) $t = 2\pi$.

Figure 38. Velocity profiles in the neighborhood of an instantaneous stagnation point location for the turbine cascade subjected to an upstream acoustic excitation with $p_{I,-\infty} = (0.35, 0)$, $\omega = 1$ and $\sigma = 0$: (a) through (d) as in Figure 36.

Figure 39. Temporal mean values and upper and lower bounds for the displacement thickness and surface shear stress along a turbine blade surface for an upstream pressure excitation with $p_{I,-\infty} = (0.35, 0)$, $\omega = 1$ and $\sigma = 0$.

Figure 40. Temporal mean values and upper and lower bounds for the displacement thickness and minimum wake streamwise velocity along a turbine wake for an upstream pressure excitation with $p_{I,-\infty} = (0.35, 0)$, $\omega = 1$ and $\sigma = 0$.

Figure 41. Streamwise velocity profiles in the wake of a turbine blade for an acoustic excitation from upstream with $p_{I,-\infty} = (0.35, 0)$, $\omega = 1$ and $\sigma = 0$.

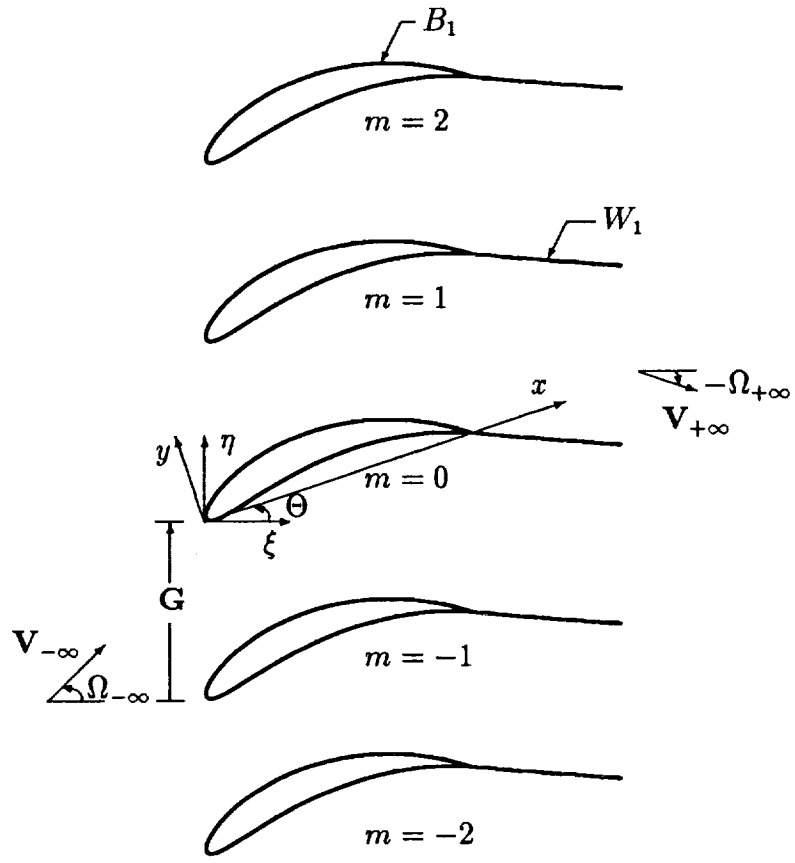

Figure 1: Two-dimensional compressor cascade.

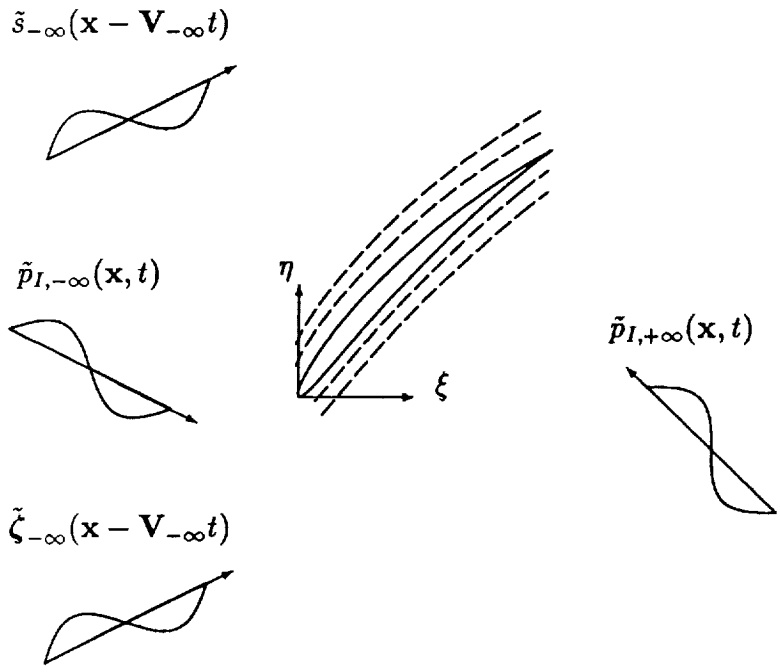

Figure 2: Unsteady excitations: blade motion; incident vortical and entropic disturbances from upstream; and incident acoustic disturbances from upstream and downstream.

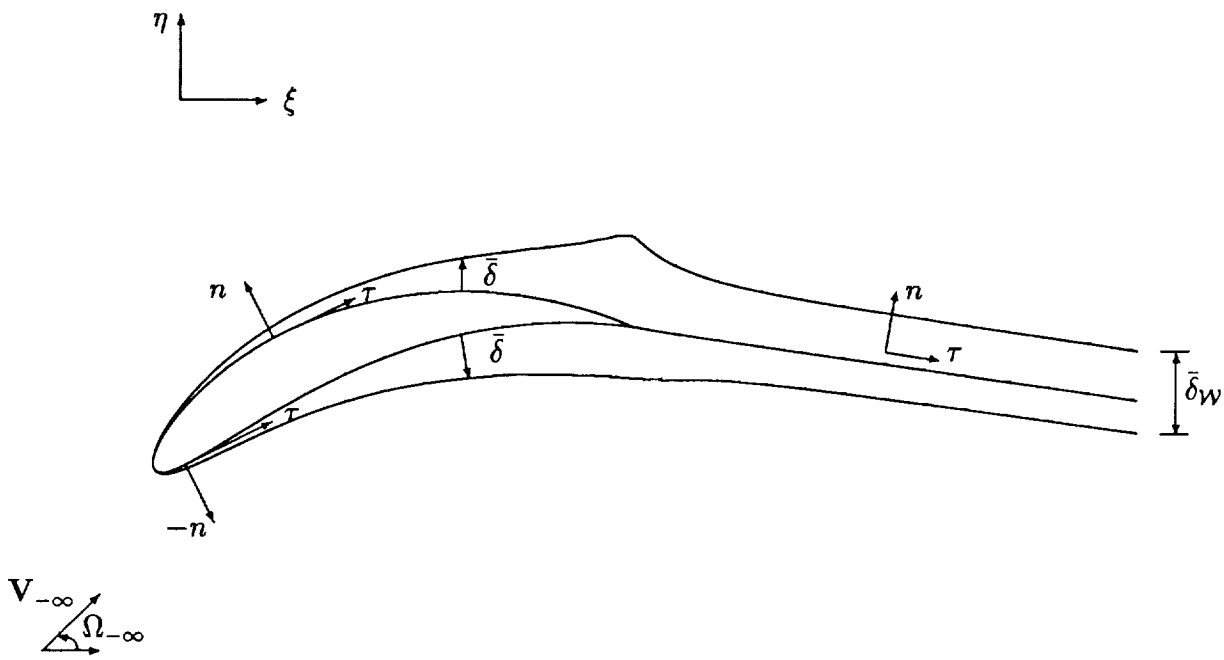

Figure 3: High Reynolds number steady flow over a blade surface.

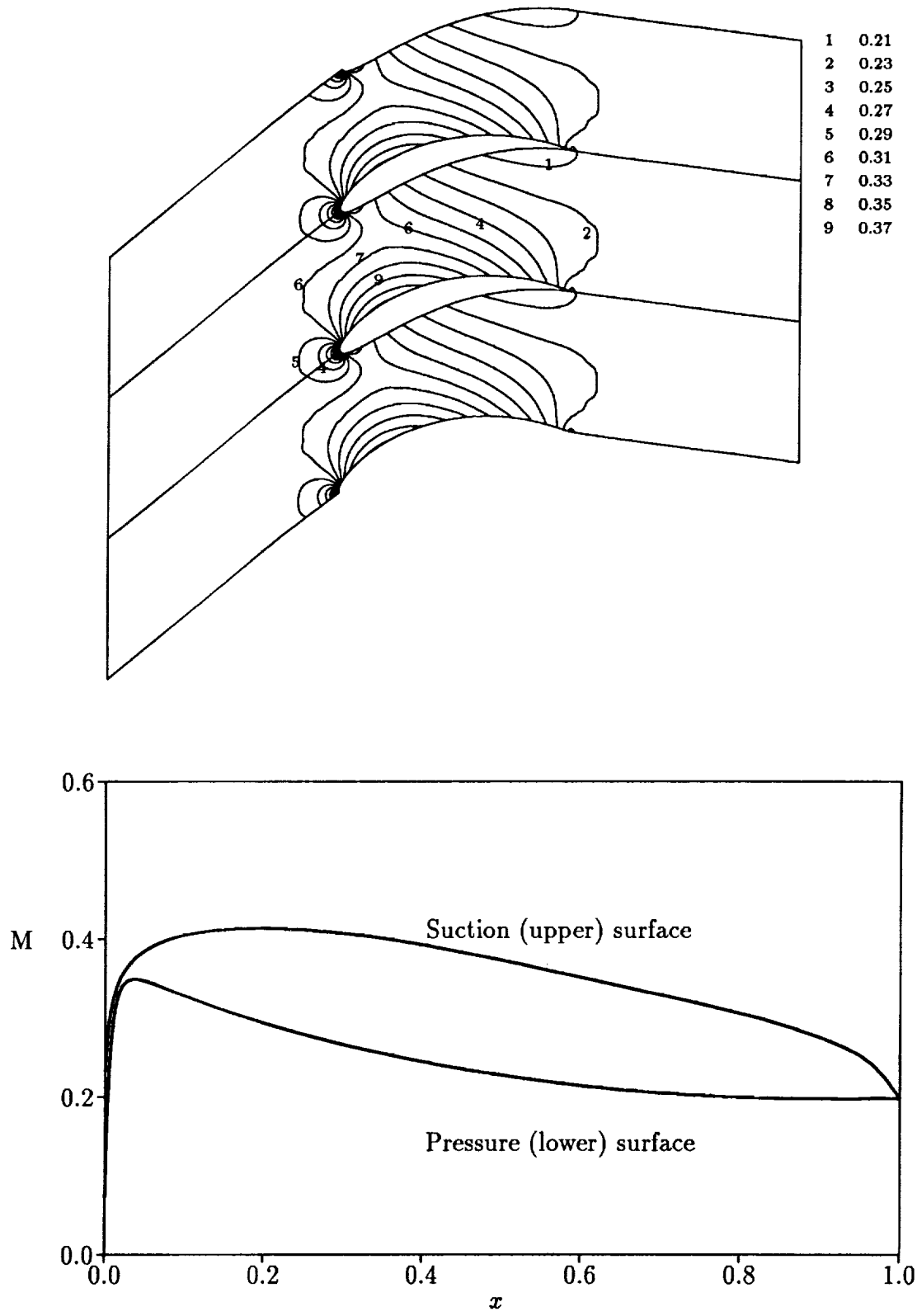

Figure 4: Mach number contours and blade surface Mach number distributions for steady flow at $M_{-\infty} = 0.3$ and $\Omega_{-\infty} = 40$ deg through the EGV cascade.

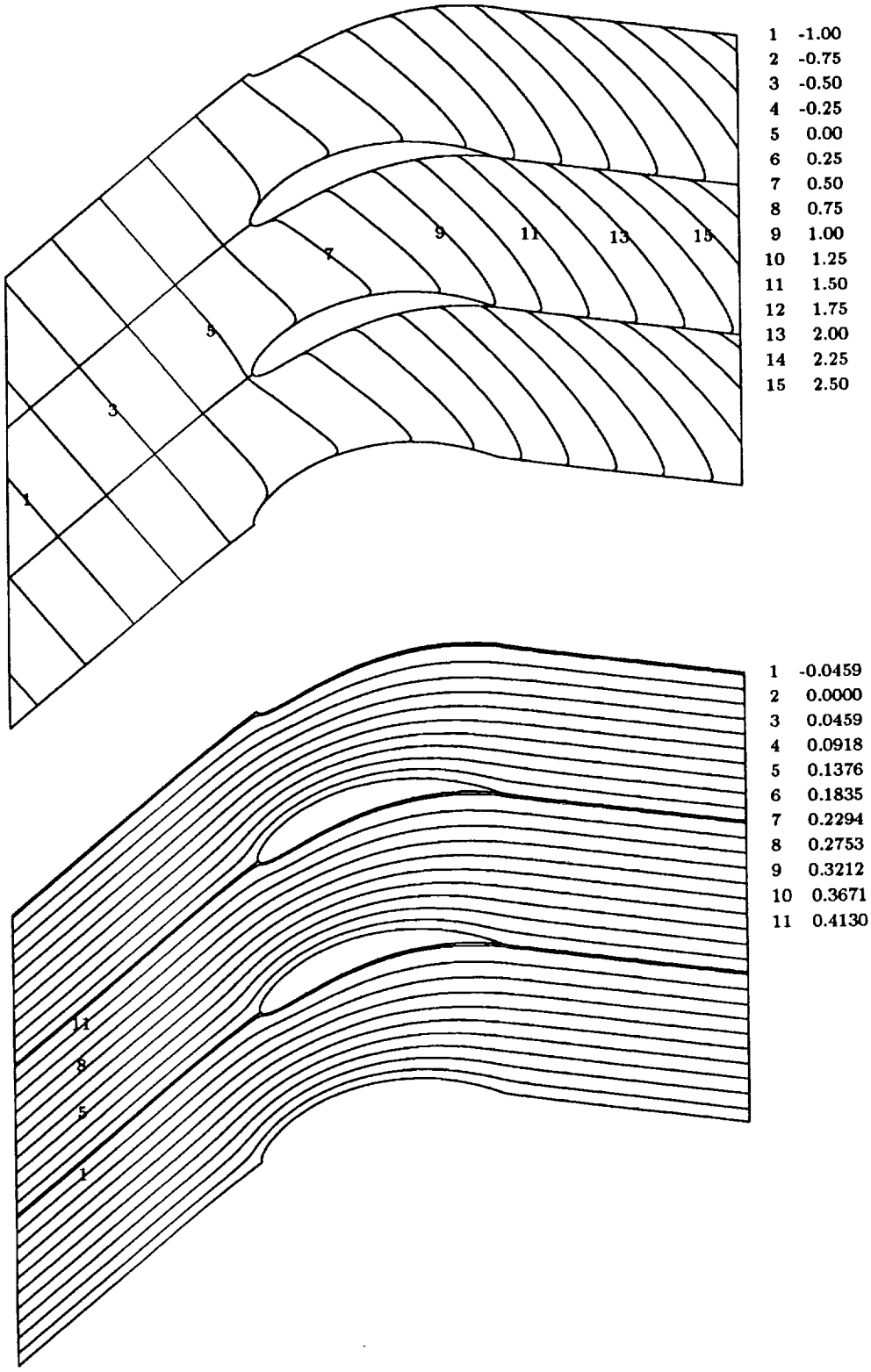

Figure 5: Drift and stream contours for steady flow at $M_{-\infty} = 0.3$ and $\Omega_{-\infty} = 40$ deg through the EGV cascade.

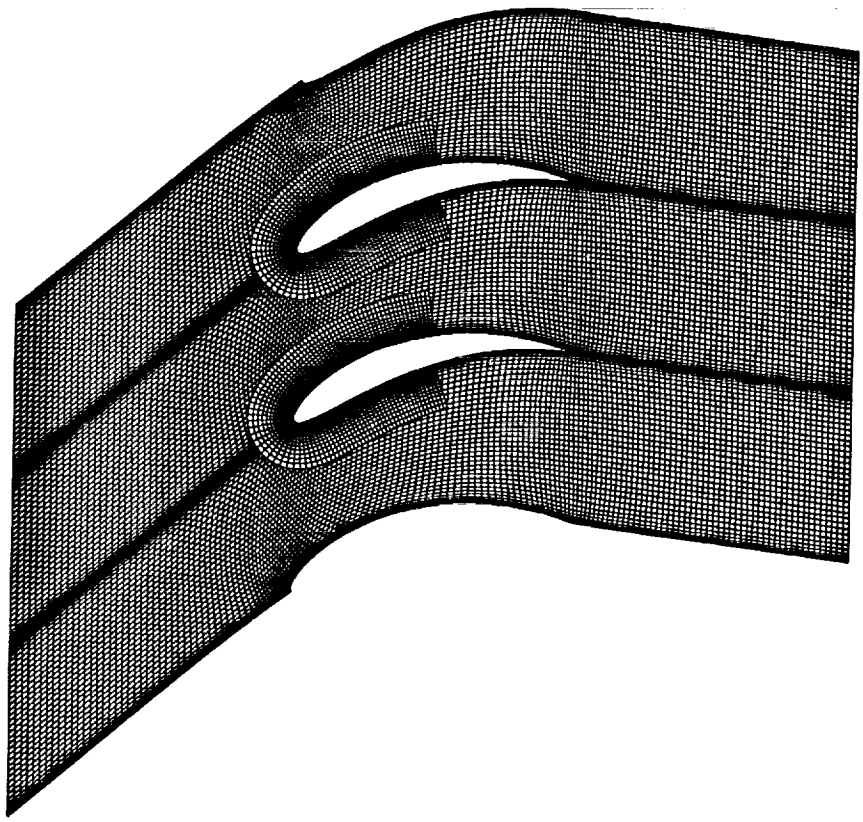

Figure 6: Global and local meshes used for the EGV unsteady flow calculations.

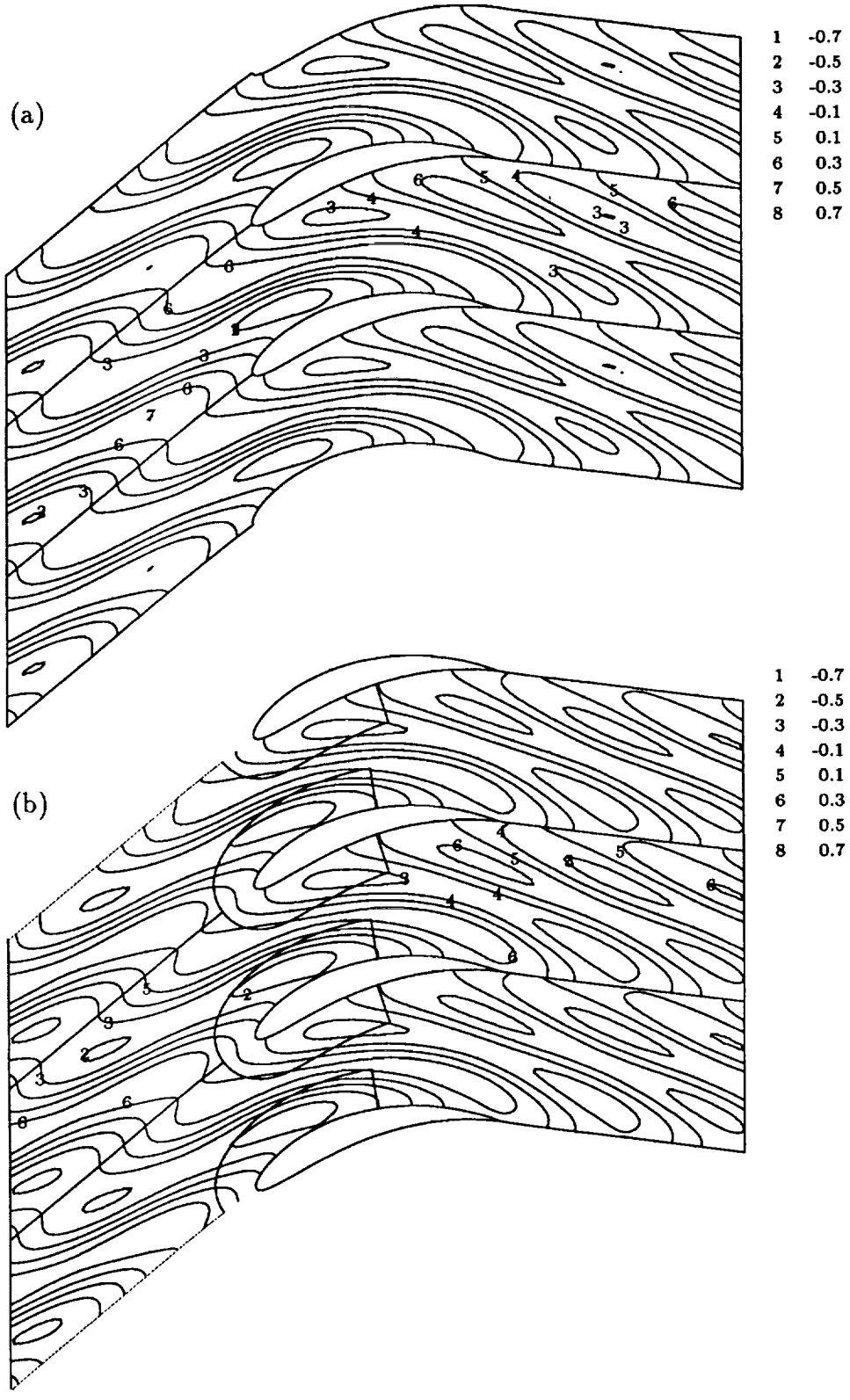

Figure 7: In-phase component (real part) of the linearized unsteady potential due to the interaction of a vortical gust with $\mathbf{v}_{R,-\infty} \cdot \mathbf{e}_N = (1,0)$, $\omega = 5$ and $\sigma = -2\pi$ and the EGV cascade: (a) global-mesh calculation; (b) composite-mesh calculation.

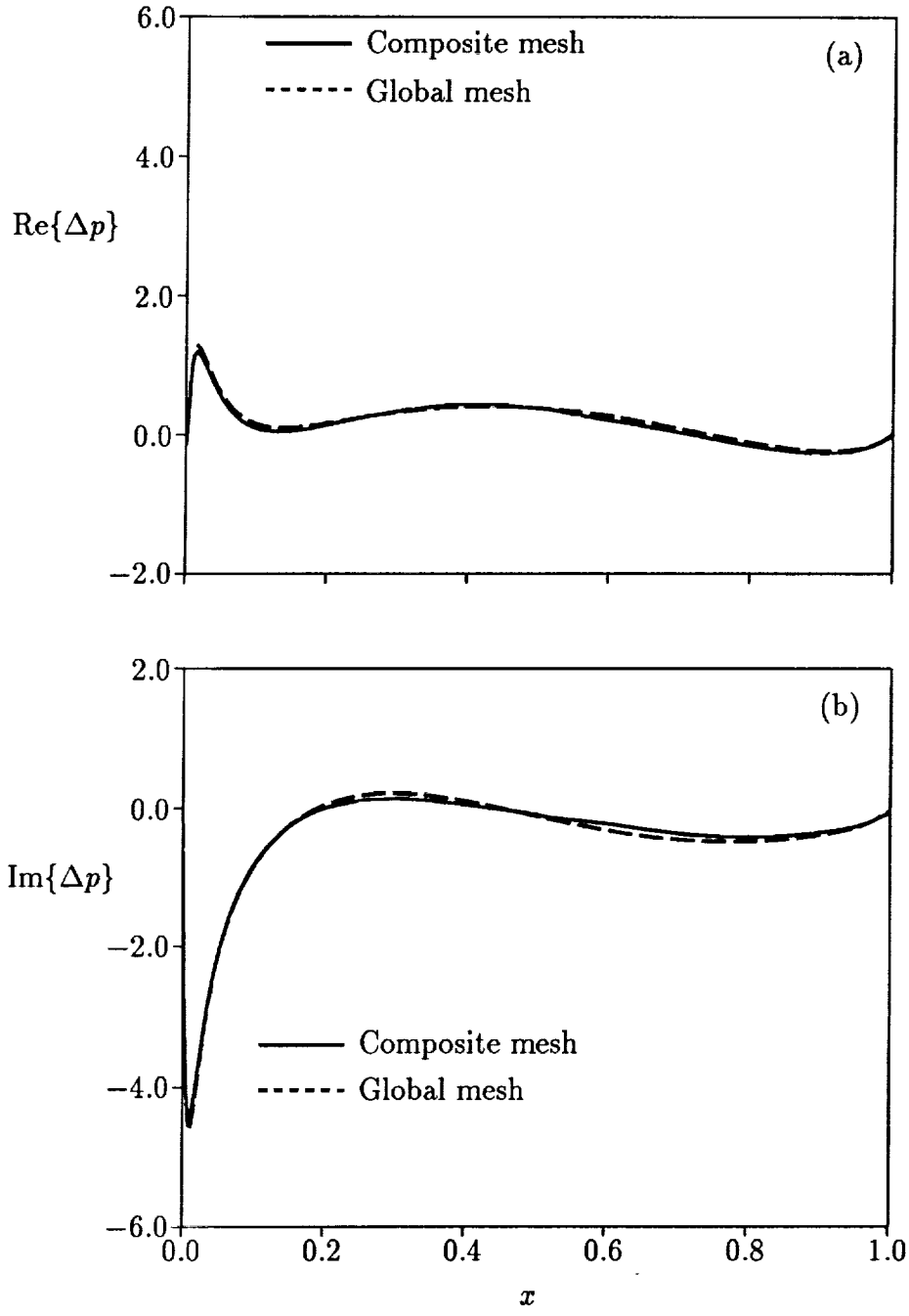

Figure 8: Global- and composite-mesh solutions for the unsteady pressure-difference response due to the interaction of a vortical gust with $\mathbf{v}_{R,-\infty} \cdot \mathbf{e}_N = (1, 0)$, $\omega = 5$ and $\sigma = -2\pi$ and the EGV cascade: (a) in-phase component (real part) of the unsteady pressure difference; (b) out-of-phase component (imaginary part).

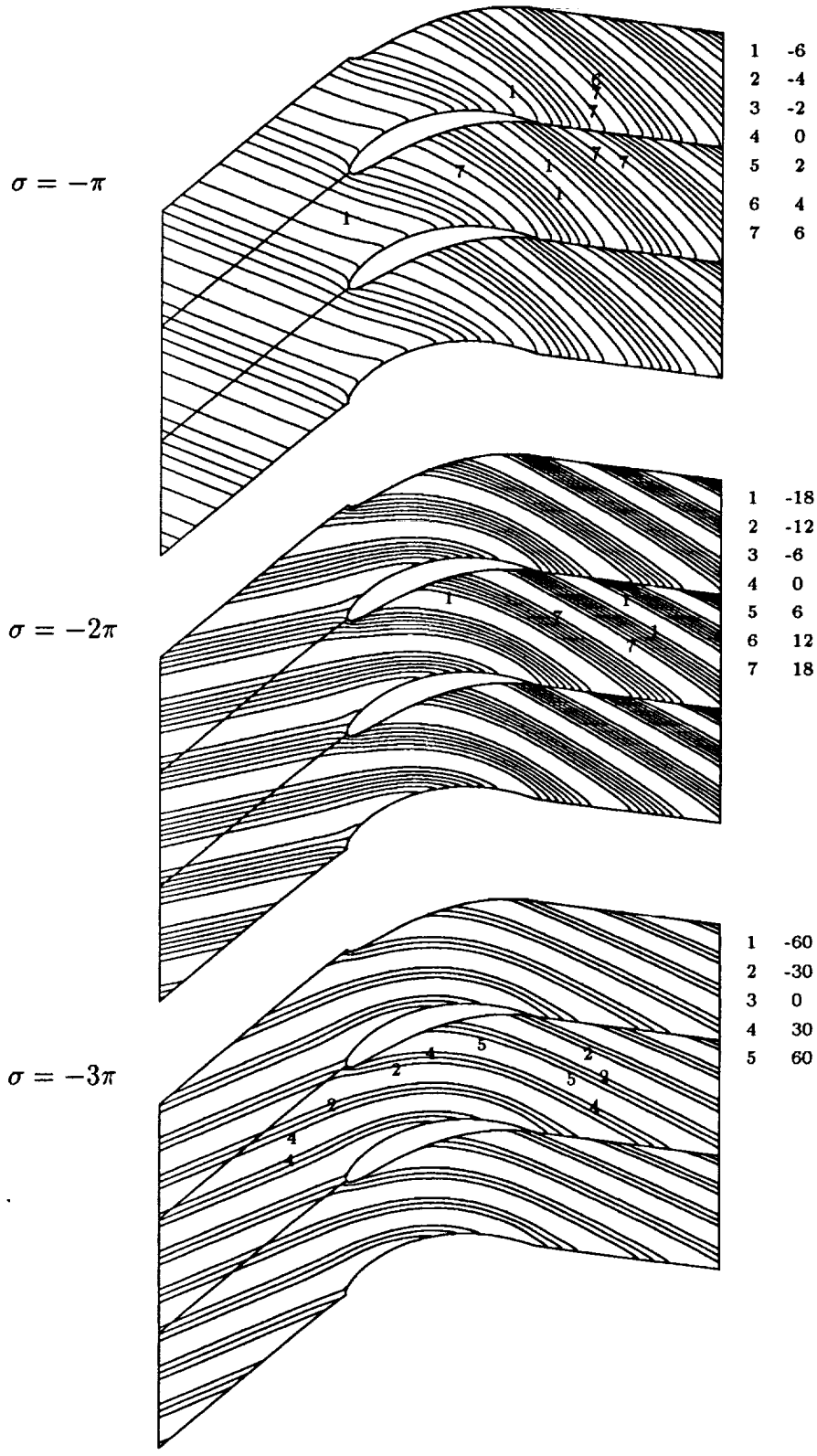

Figure 9: Contours of the in-phase component of the unsteady vorticity for the EGV cascade subjected to vortical gusts with $\mathbf{v}_{R,-\infty} \cdot \mathbf{e}_N = (1,0)$ and $\omega = 5$.

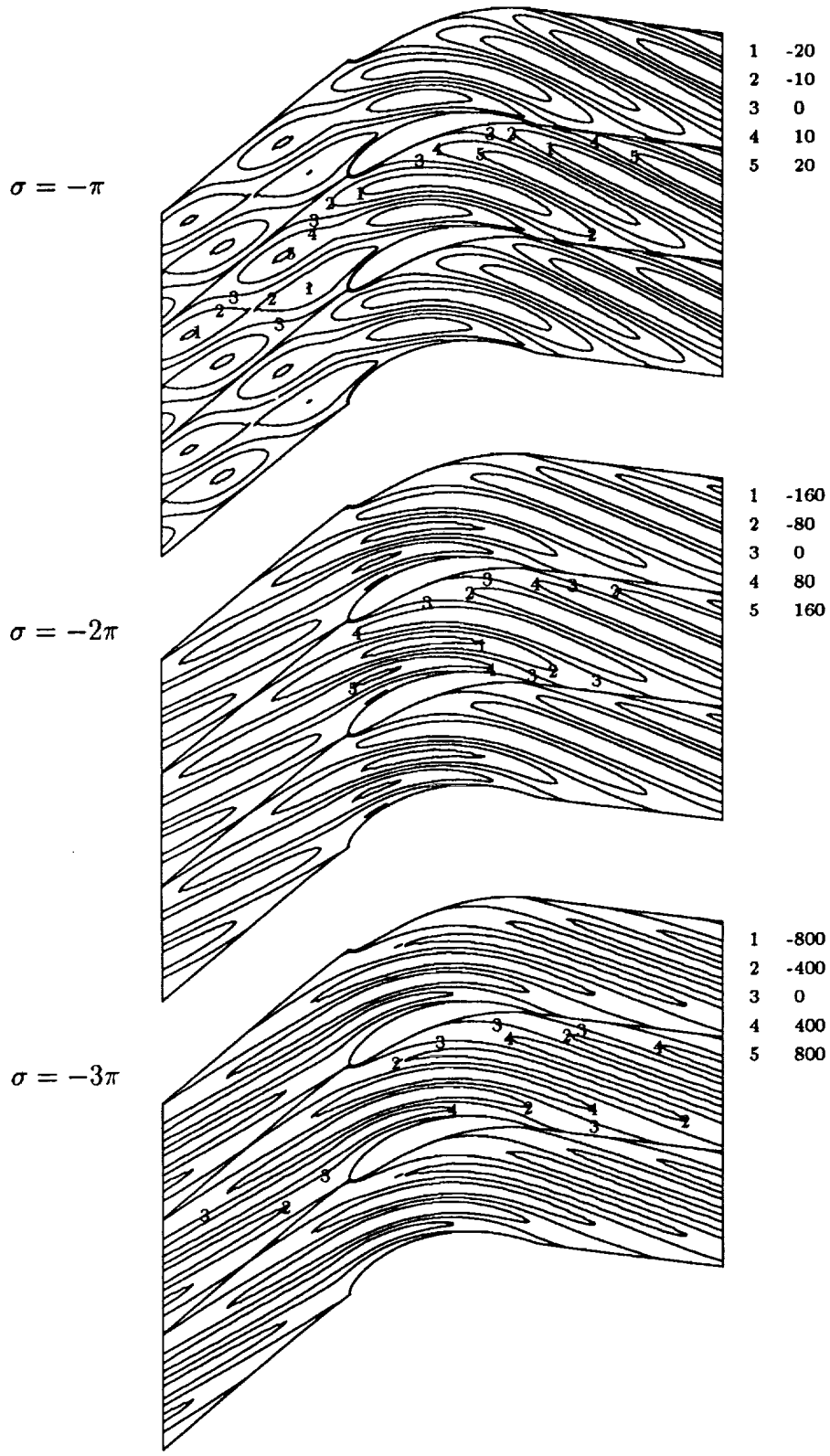

Figure 10: Contours of the in-phase component of the source term for the EGV cascade subjected to vortical gusts with $\mathbf{v}_{R,-\infty} \cdot \mathbf{e}_N = (1,0)$ and $\omega = 5$.

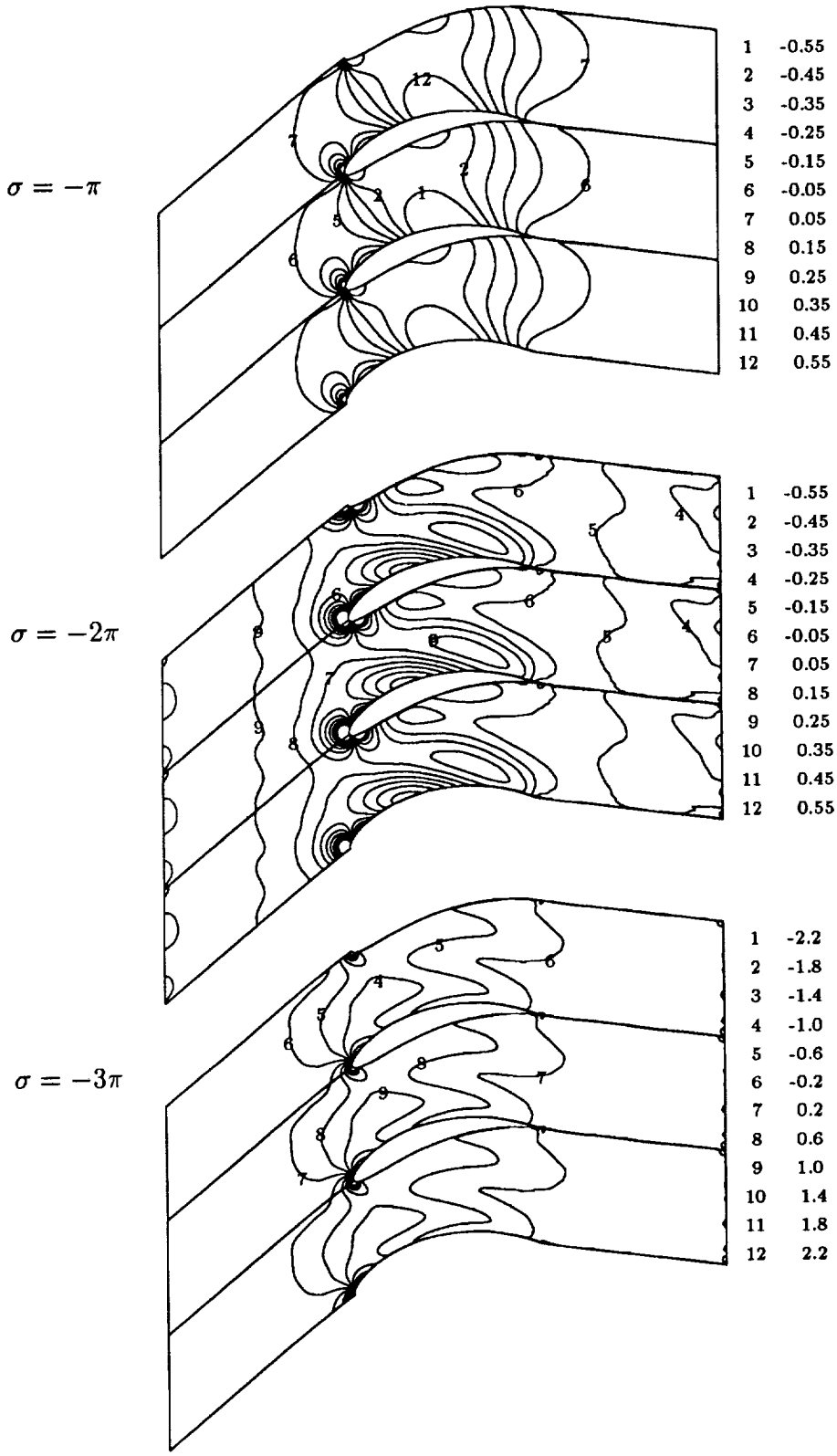

Figure 11: Contours of the in-phase component of the unsteady pressure for the EGV cascade subjected to vortical gusts with $\mathbf{v}_{R,-\infty} \cdot \mathbf{e}_N = (1,0)$ and $\omega = 5$.

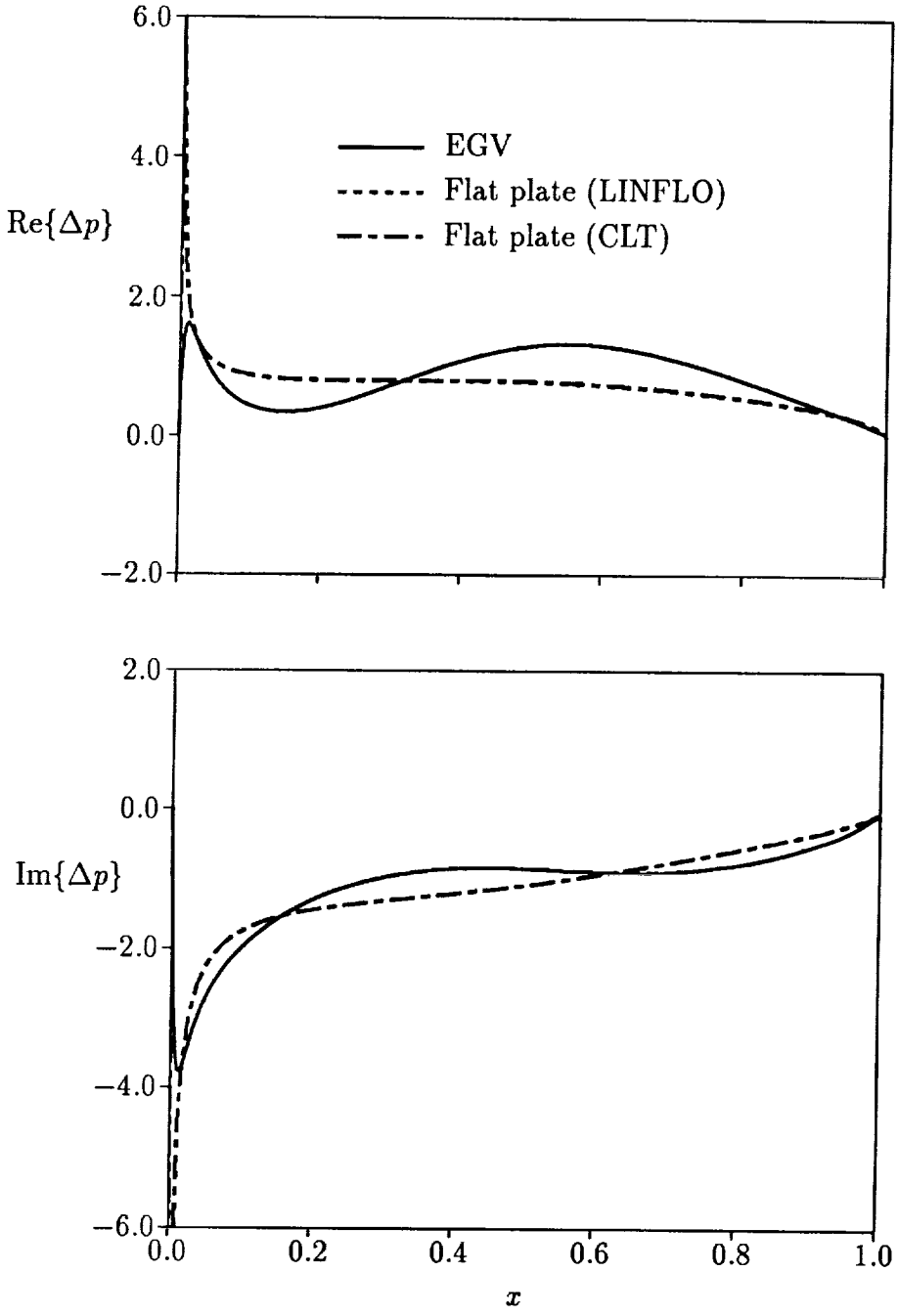

Figure 12: Unsteady pressure-difference response of the EGV and corresponding flat-plate cascades subjected to a vortical gust with $\mathbf{v}_{R,-\infty} \cdot \mathbf{e}_N = (1,0)$, $\omega = 5$ and $\sigma = -\pi$.

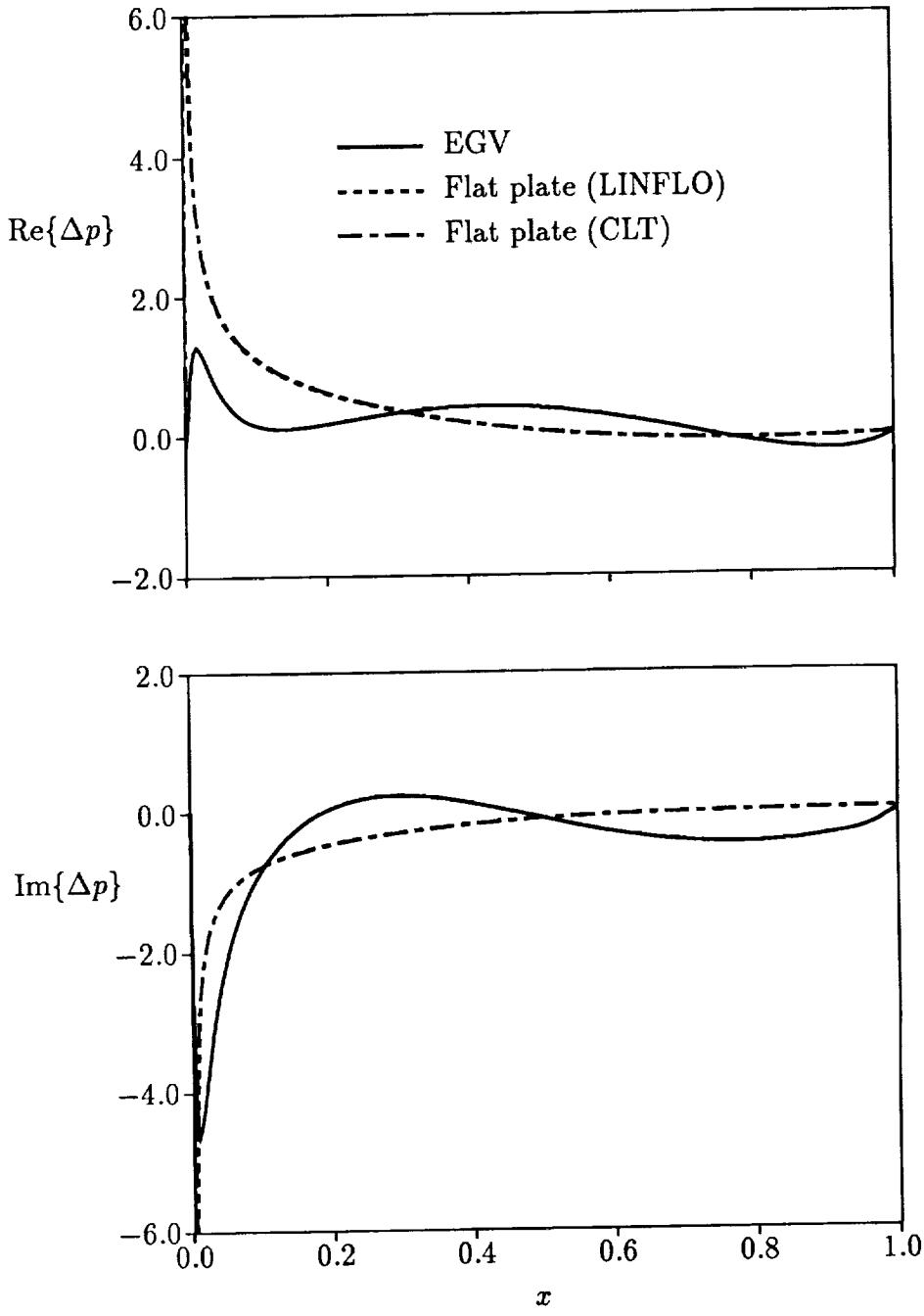

Figure 13: Unsteady pressure-difference response of the EGV and corresponding flat-plate cascades subjected to a vortical gust with $\mathbf{v}_{R,-\infty} \cdot \mathbf{e}_N = (1,0)$, $\omega = 5$ and $\sigma = -2\pi$.

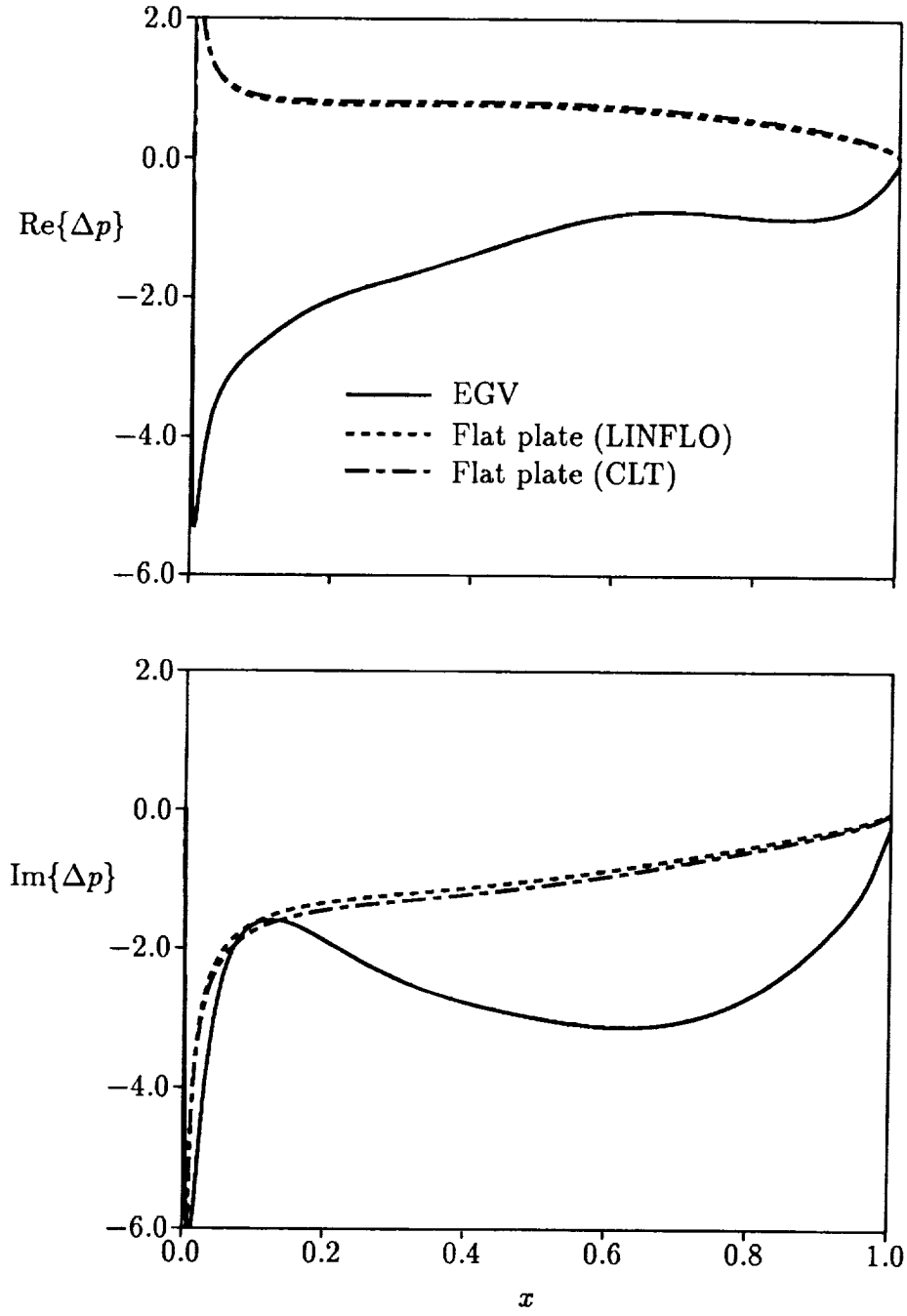

Figure 14: Unsteady pressure-difference response of the EGV and corresponding flat-plate cascades subjected to a vortical gust with $\mathrm{v}_{R,-\infty} \cdot \mathbf{e}_N = (1,0)$, $\omega = 5$ and $\sigma = -3\pi$.

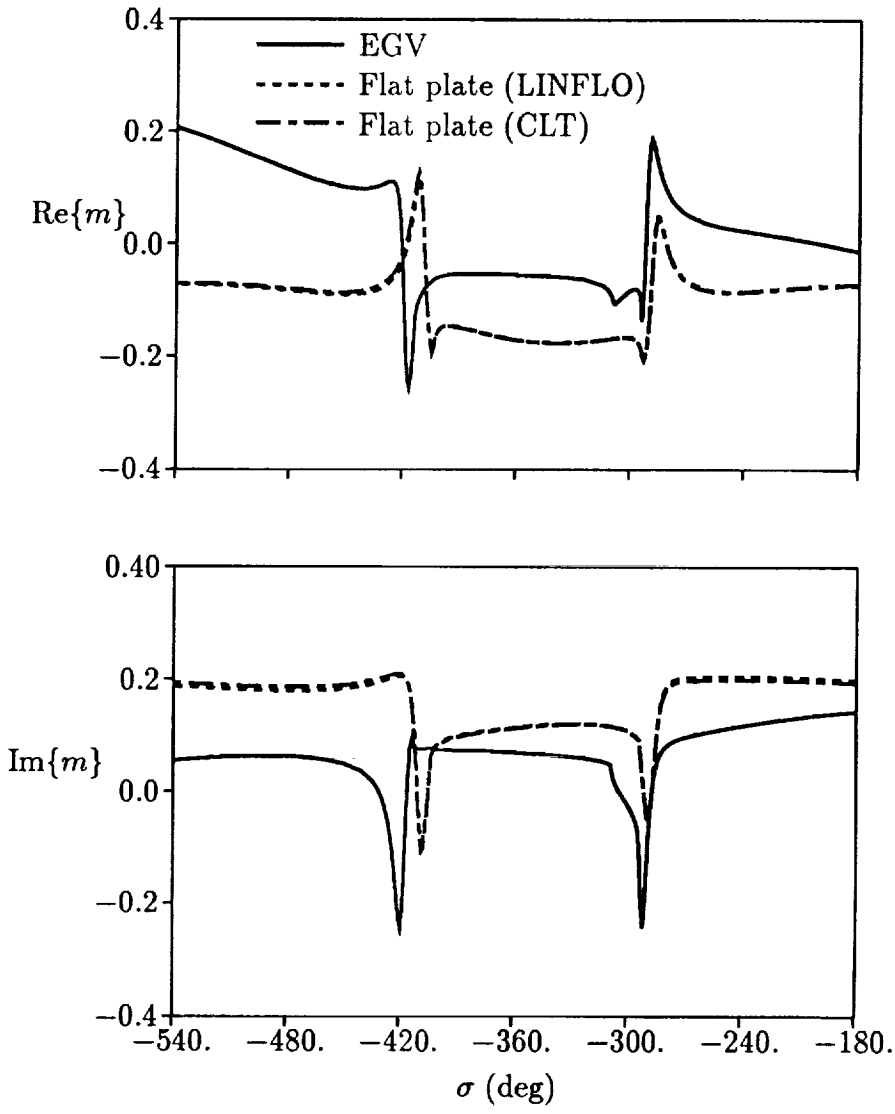

Figure 15: Unsteady moment vs interblade phase angle for the EGV and corresponding flat-plate cascades subjected to vortical gusts with $\mathbf{v}_{R,-\infty} \cdot \mathbf{e}_N = (1, 0)$ and $\omega = 5$.

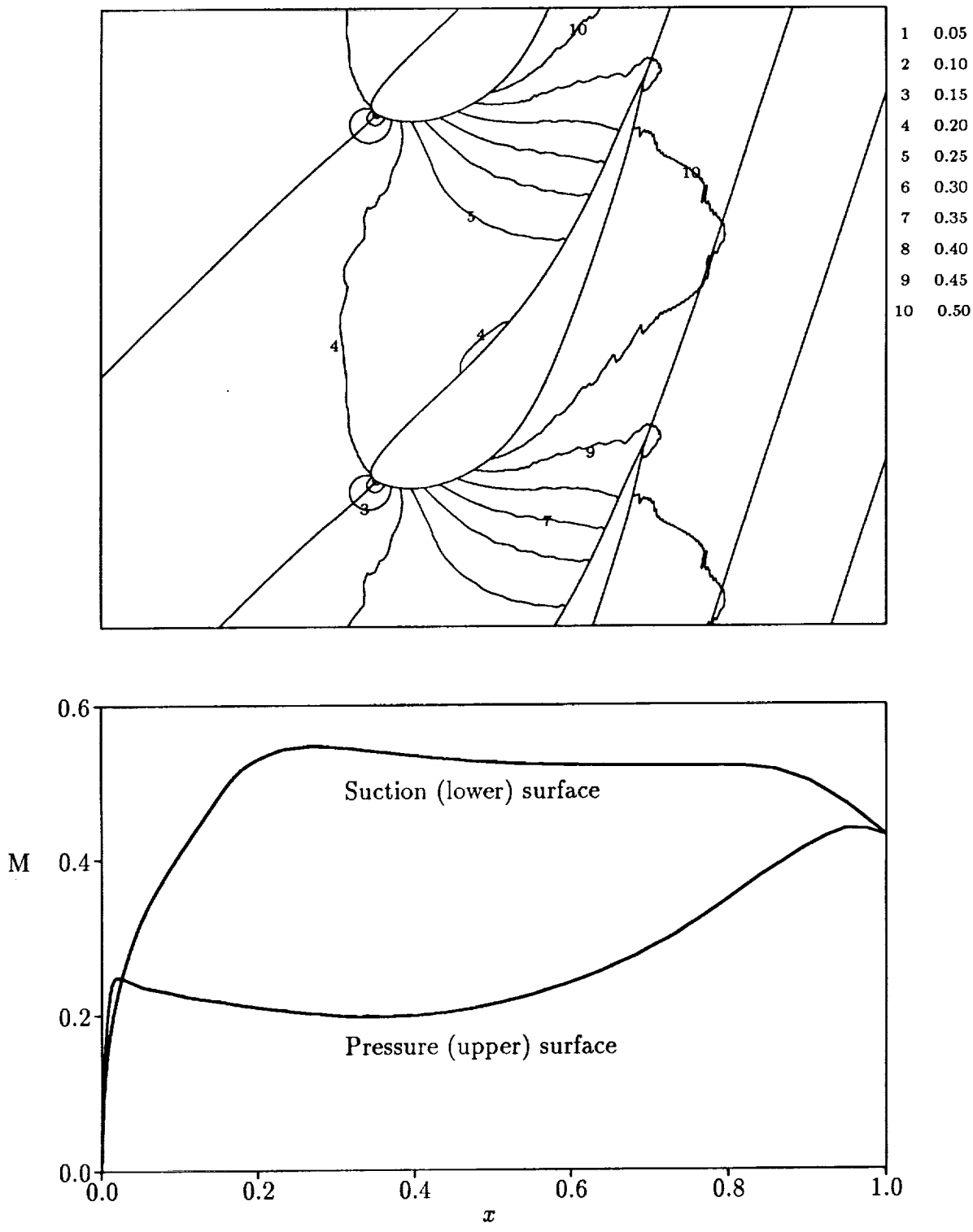

Figure 16: Mach number contours and blade surface Mach number distributions for steady flow at $M_{-\infty} = 0.19$ and $\Omega_{-\infty} = 45$ deg through the turbine cascade.

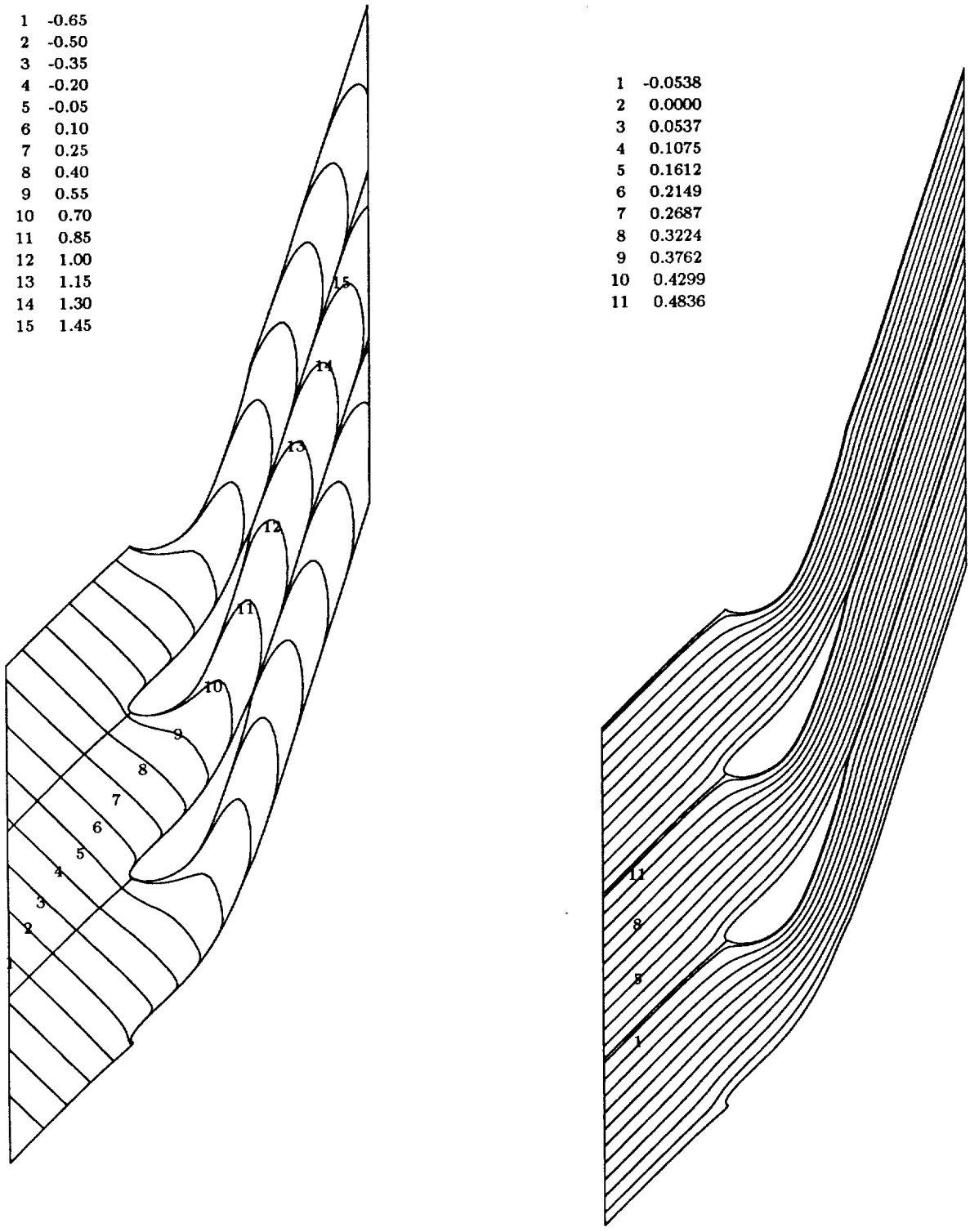

Figure 17: Drift and stream contours for steady flow at $M_{-\infty} = 0.19$ and $\Omega_{-\infty} = 45$ deg through the turbine cascade.

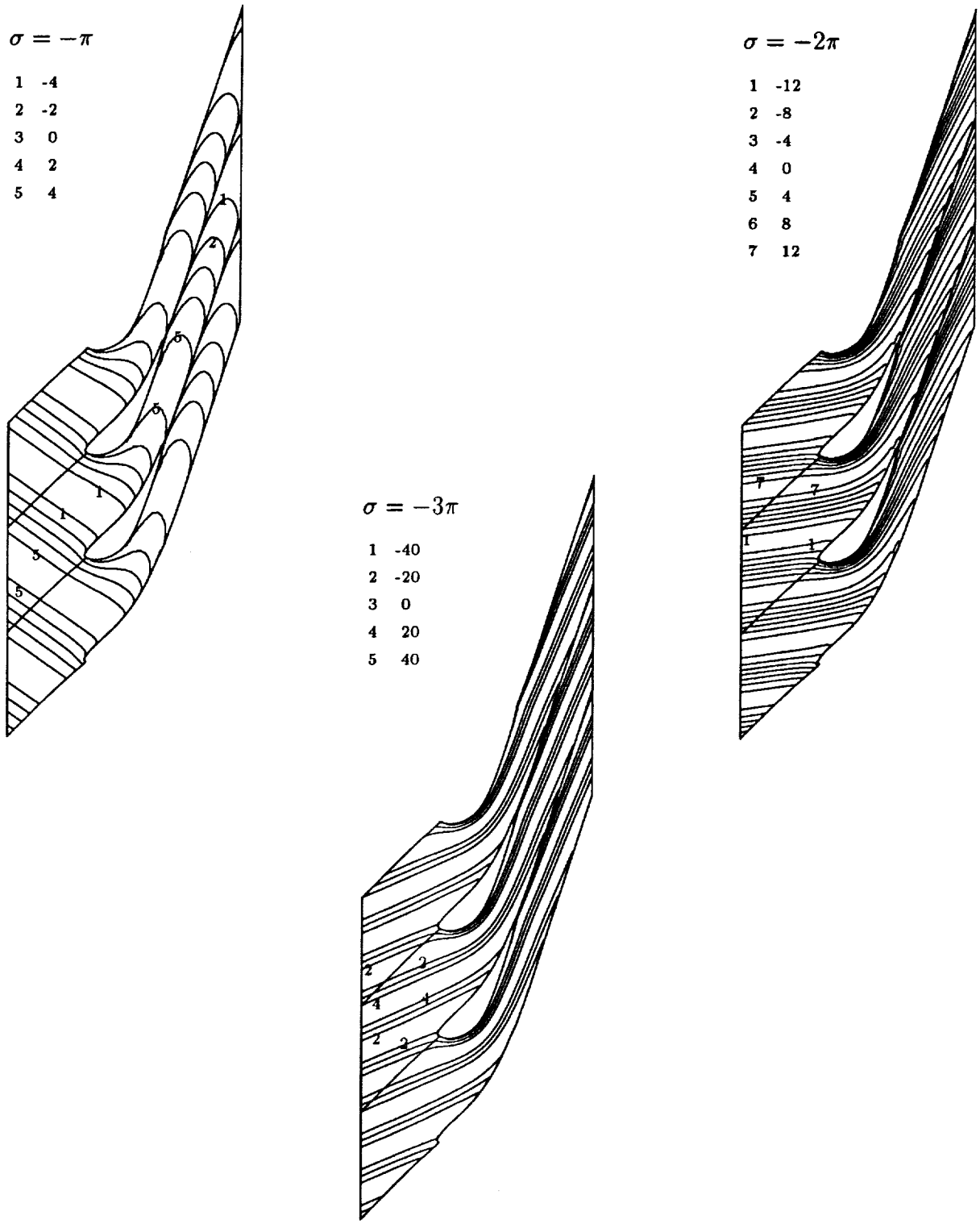

Figure 18: Contours of the in-phase component of the unsteady vorticity for the turbine cascade subjected to vortical gusts with $\mathbf{v}_{R,-\infty} \cdot \mathbf{e}_N = (1, 0)$ and $\omega = 5$.

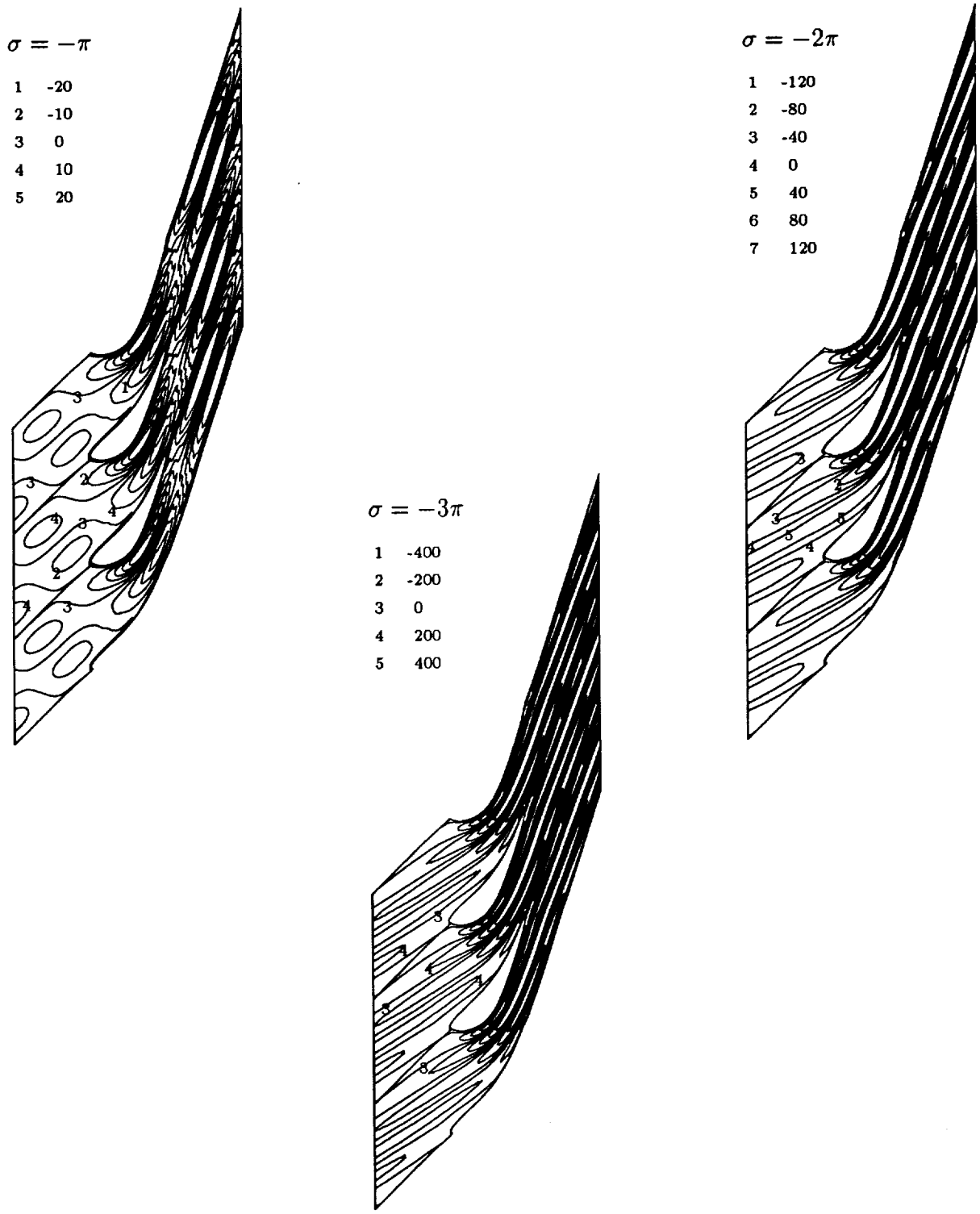

Figure 19: Contours of the in-phase component of the source term for the turbine cascade subjected to vortical gusts with $\mathbf{v}_{R,-\infty} \cdot \mathbf{e}_N = (1,0)$ and $\omega = 5$.

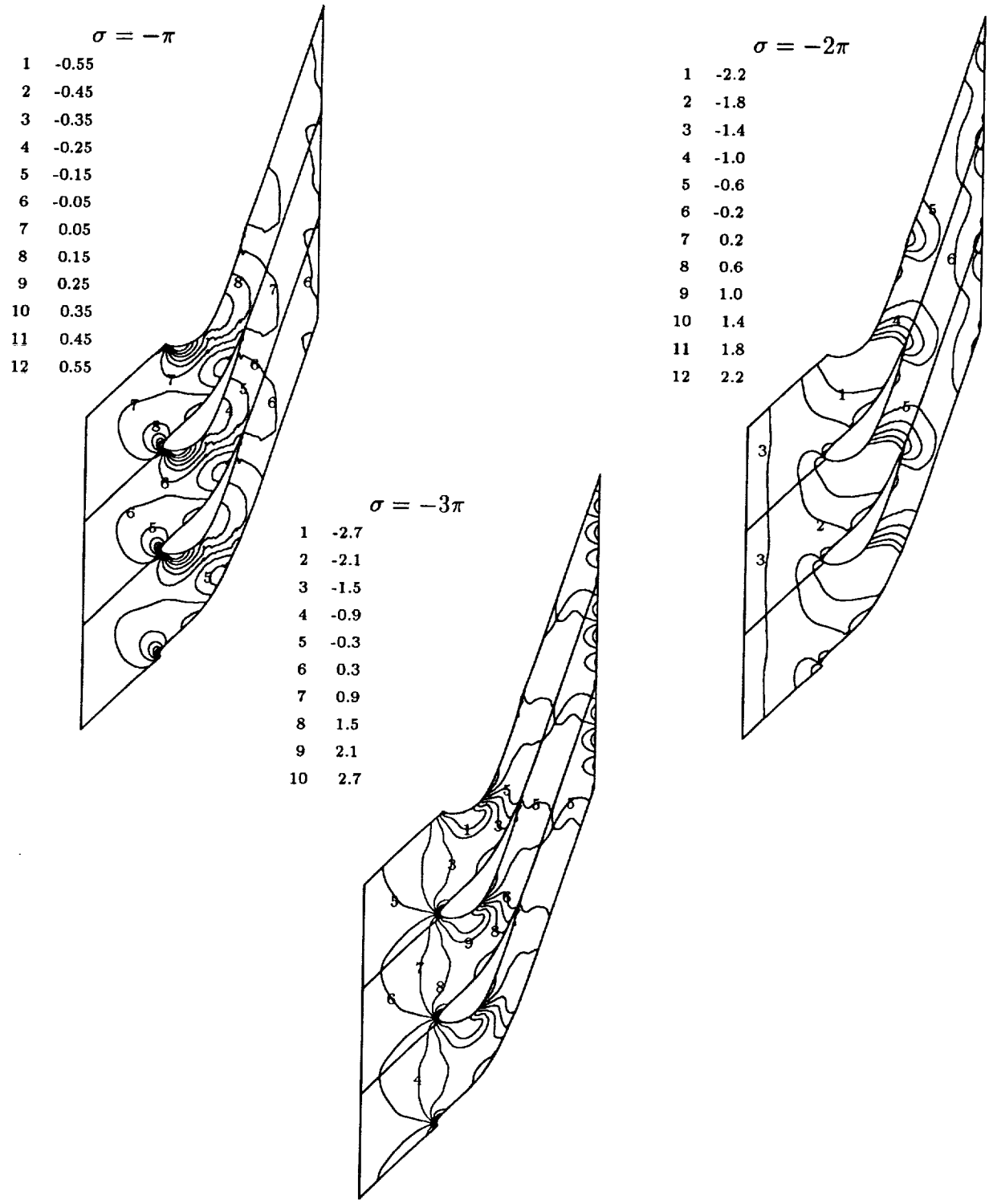

Figure 20: Contours of the in-phase component of the unsteady pressure for the turbine cascade subjected to vortical gusts with $\mathbf{v}_{R,-\infty} \cdot \mathbf{e}_N = (1, 0)$ and $\omega = 5$.

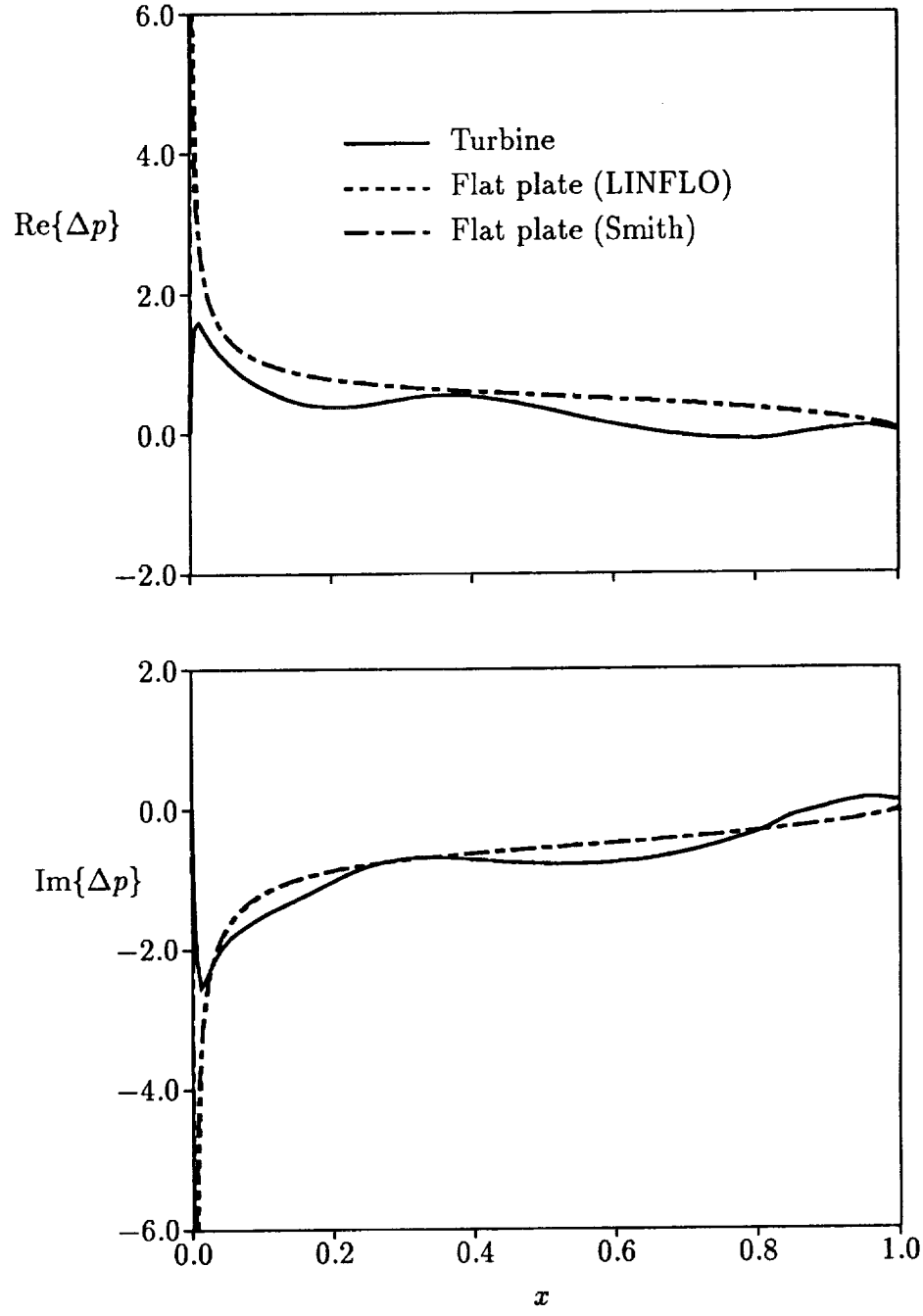

Figure 21: Unsteady pressure-difference response of the turbine and corresponding flat-plate cascades subjected to a vortical gust with $\mathbf{v}_{R,-\infty} \cdot \mathbf{e}_N = (1,0)$, $\omega = 5$ and $\sigma = -\pi$.

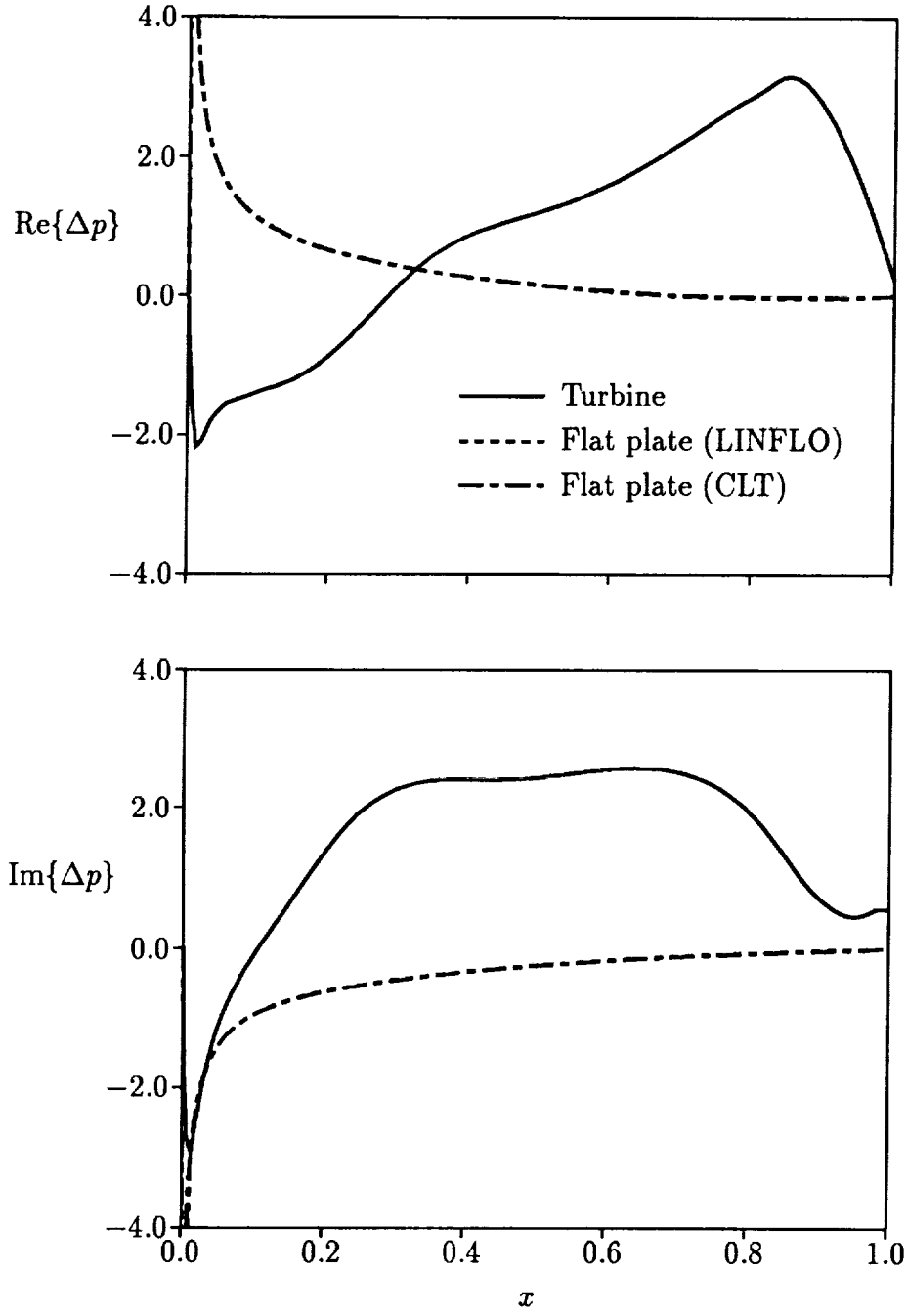

Figure 22: Unsteady pressure-difference response of the turbine and corresponding flat-plate cascades subjected to a vortical gust with $\mathbf{v}_{R,-\infty} \cdot \mathbf{e}_N = (1,0)$, $\omega = 5$ and $\sigma = -2\pi$.

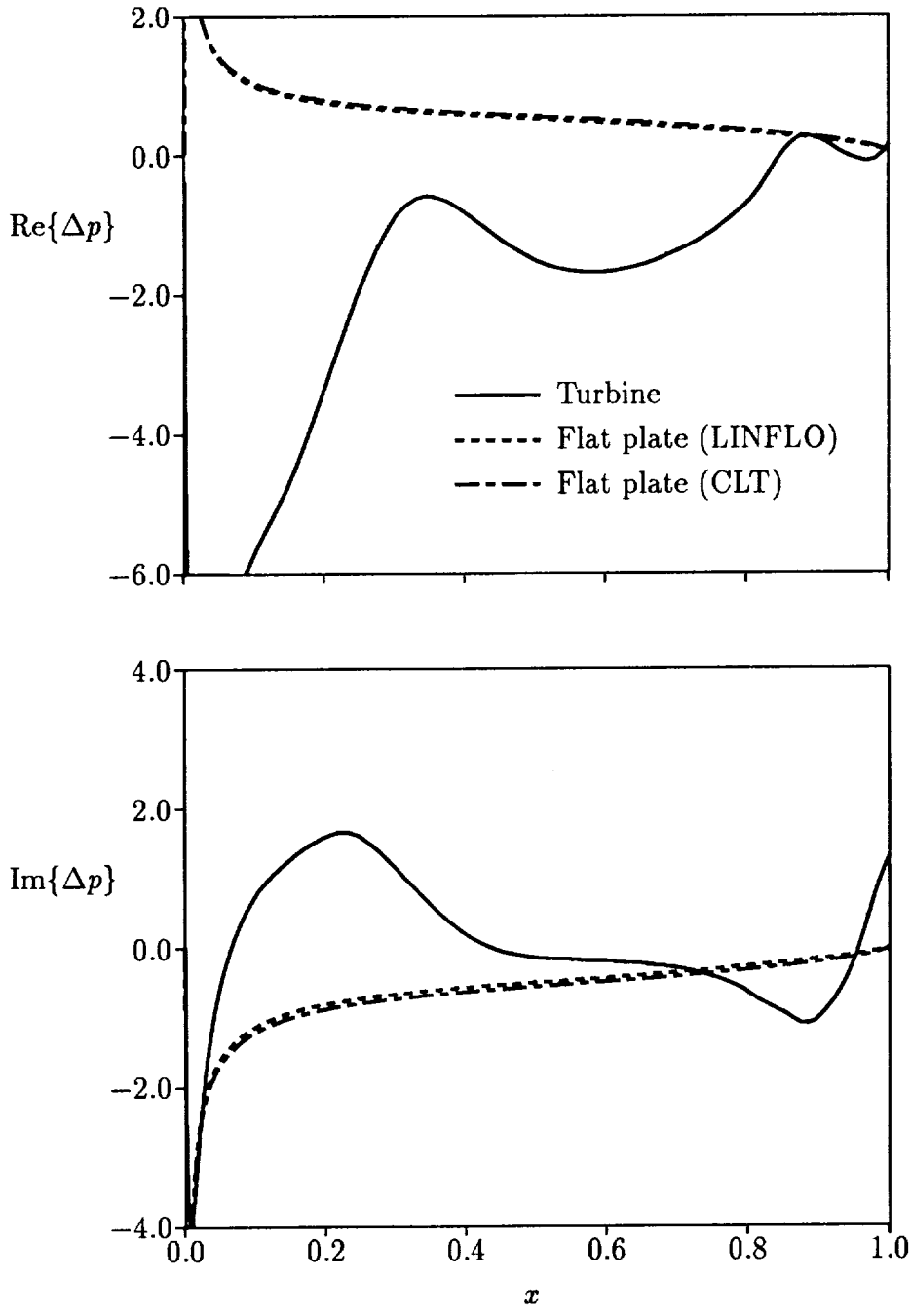

Figure 23: Unsteady pressure-difference response of the turbine and corresponding flat-plate cascades subjected to a vortical gust with $\mathbf{v}_{R,-\infty} \cdot \mathbf{e}_N = (1,0)$, $\omega = 5$ and $\sigma = -3\pi$.

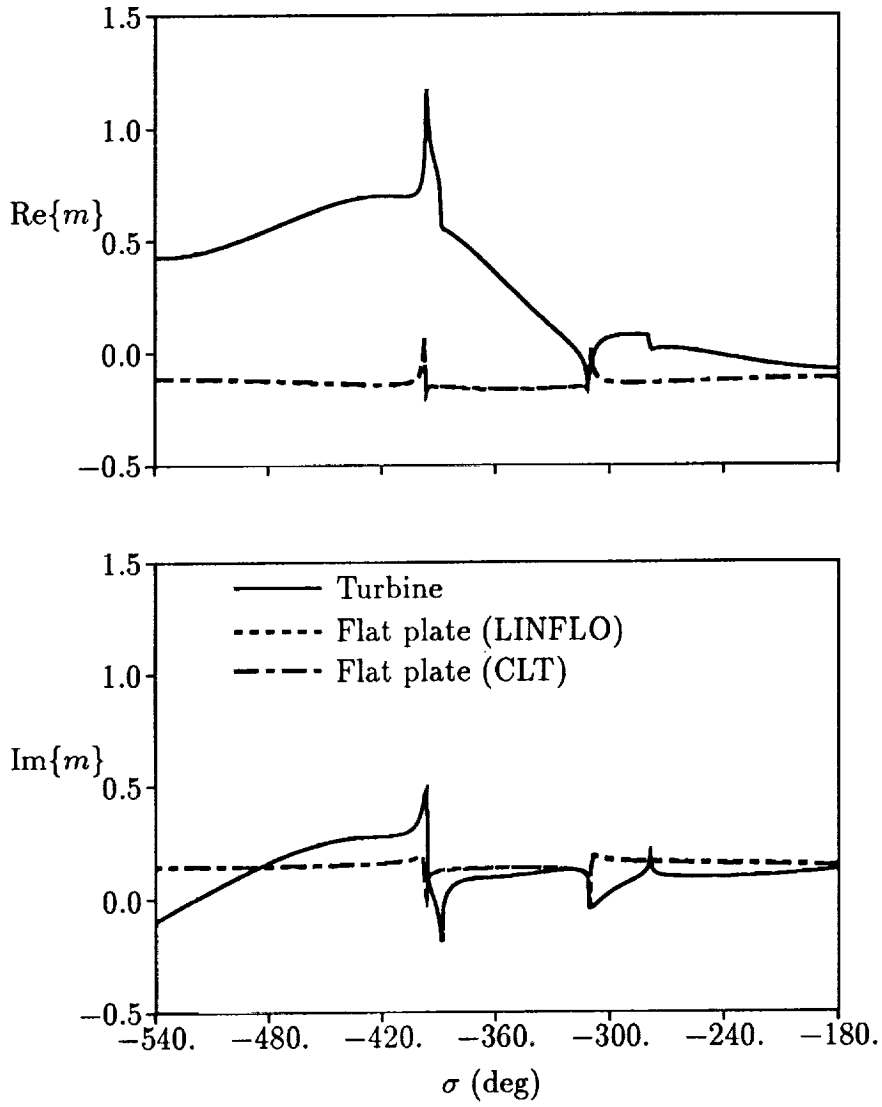

Figure 24: Unsteady moment vs interblade phase angle for the turbine and corresponding flat-plate cascades subjected to vortical gusts with $\mathbf{v}_{R,-\infty} \cdot \mathbf{e}_N = (1, 0)$ and $\omega = 5$.

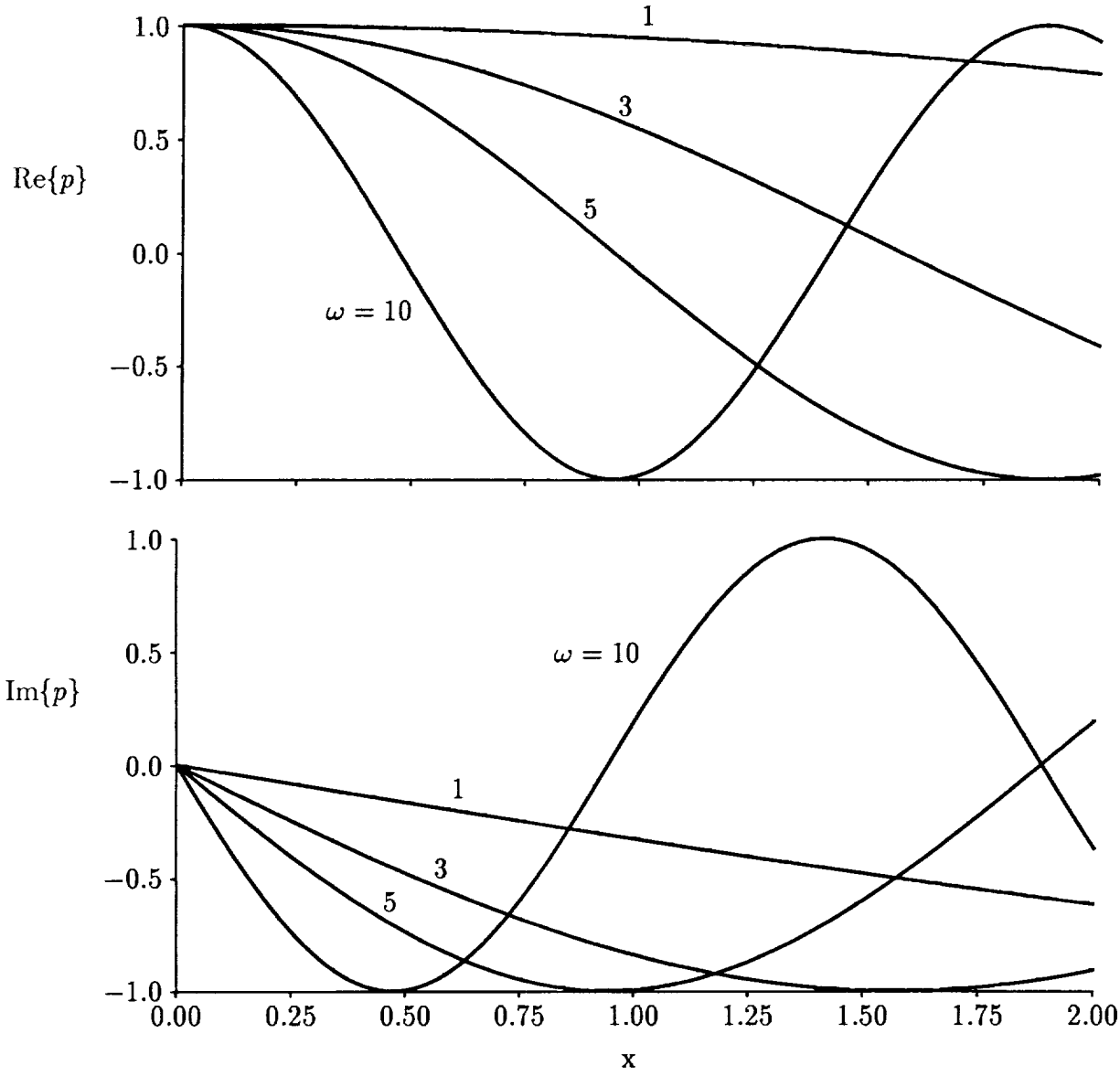

Figure 25: Unsteady pressure distributions along blade and wake for an unstaggered flat-plate cascade ($\Omega = \Theta = 0\,\text{deg}$, $M_{-\infty} = 0.5$ and $G = 1$) subjected to a unit-amplitude, $|p_{I,-\infty}| = 1$, pressure excitation from upstream with $\kappa_{\eta,-\infty} = \sigma G^{-1} = 0$.

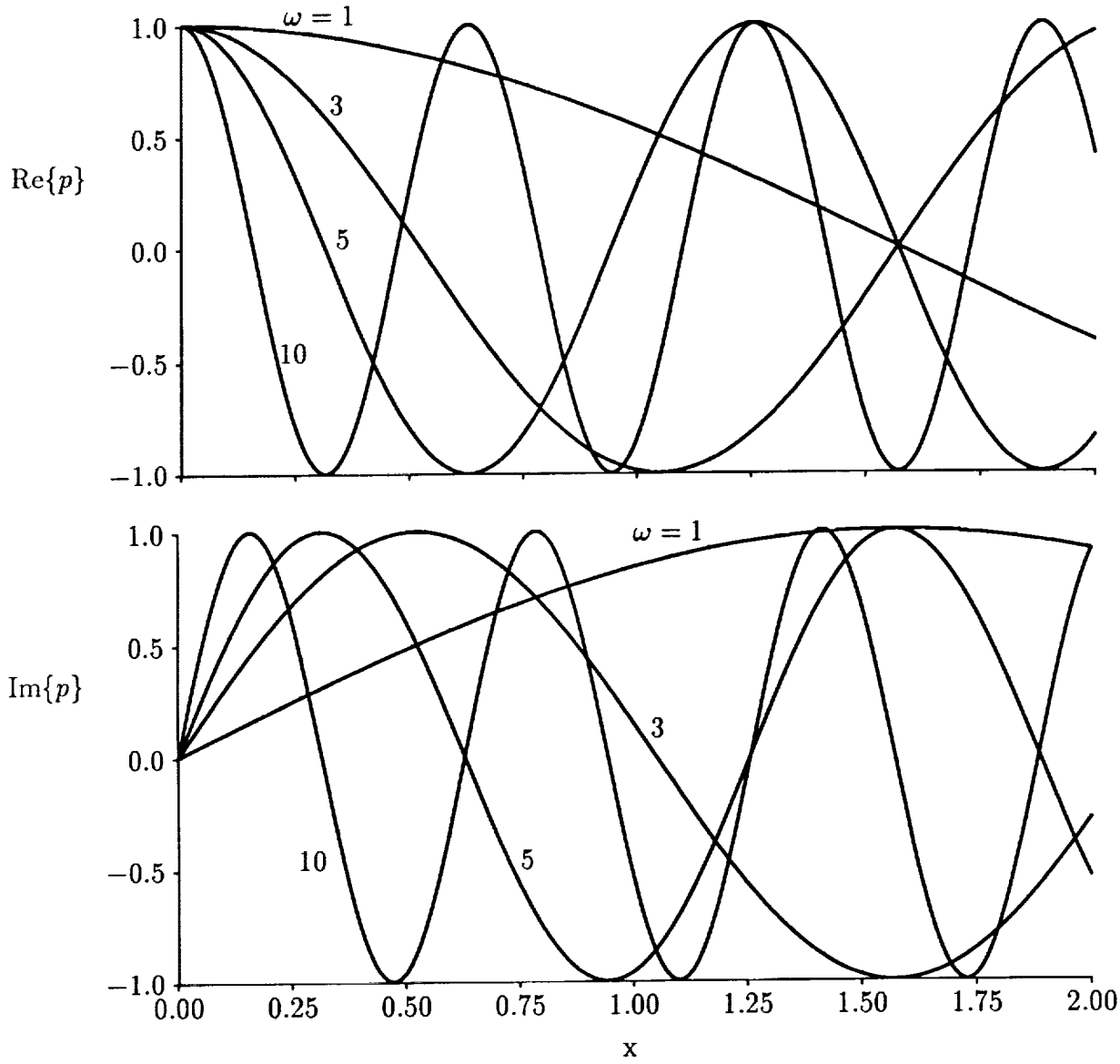

Figure 26: Unsteady pressure distributions along blade and wake for an unstaggered flat-plate cascade (with $\Omega = \Theta = 0\,\text{deg}$, $M_{-\infty} = 0.5$ and $G = 1$) subjected to a unit-amplitude, $|p_{I,+\infty}| = 1$, pressure excitation from downstream with $\kappa_{\eta,+\infty} = \sigma G^{-1} = 0$.

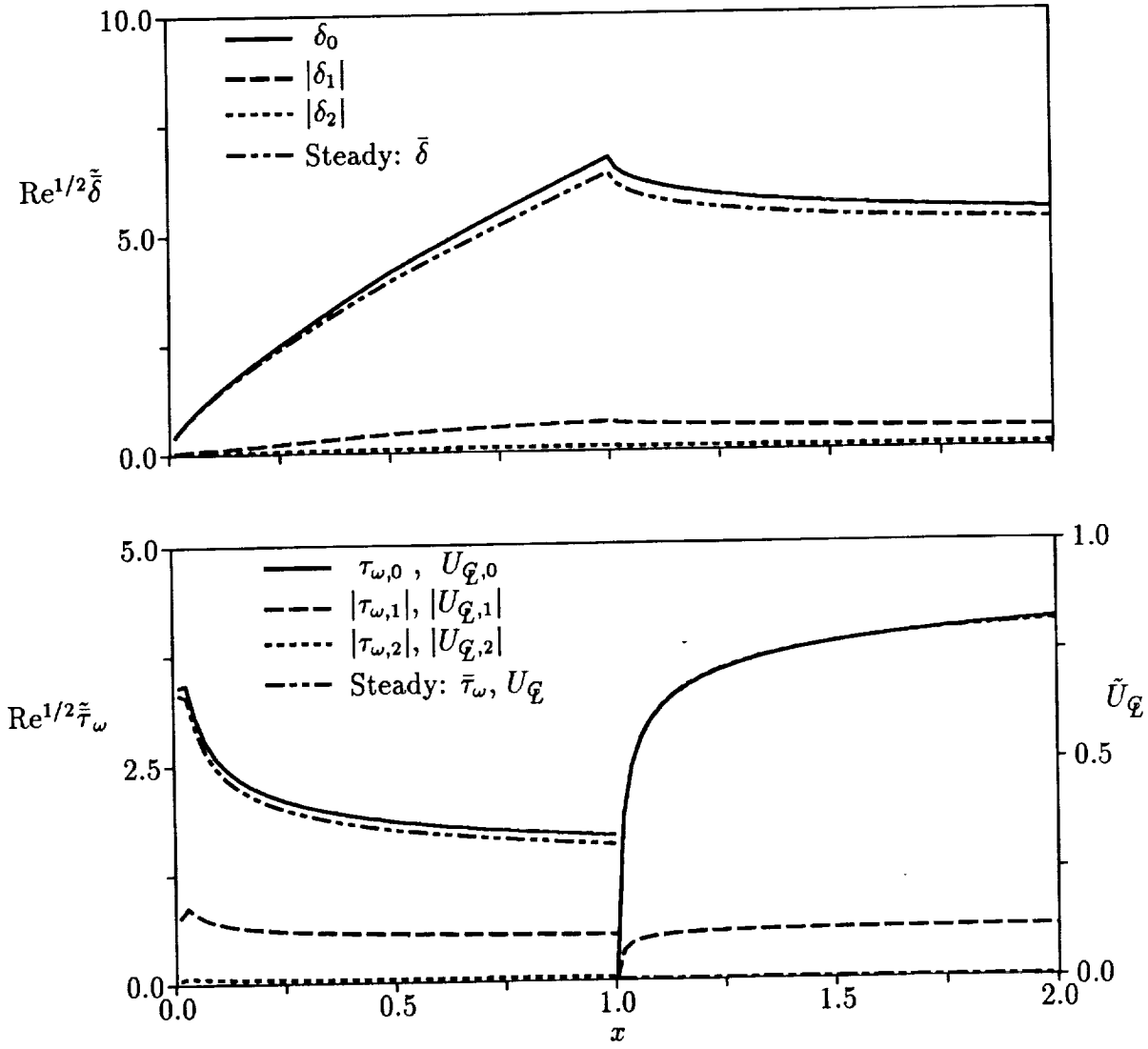

Figure 27: Temporal mean and Fourier magnitudes of the displacement thickness, $\tilde{\bar{\delta}}$, wall shear stress, $\tilde{\bar{\tau}}_\omega$, and wake centerline velocity, $\tilde{U}_{\mathcal{L}}$, for turbulent flow through an unstaggered flat-plate cascade ($\Omega = \Theta = 0\,\mathrm{deg}$, $G = 1$, $M = 0.5$ and $\mathrm{Re} = 10^6$) subjected to an incident pressure disturbance from upstream with $p_{I,-\infty} = (0.5, 0)$, $\omega = 5$ and $\sigma = 0\,\mathrm{deg}$.

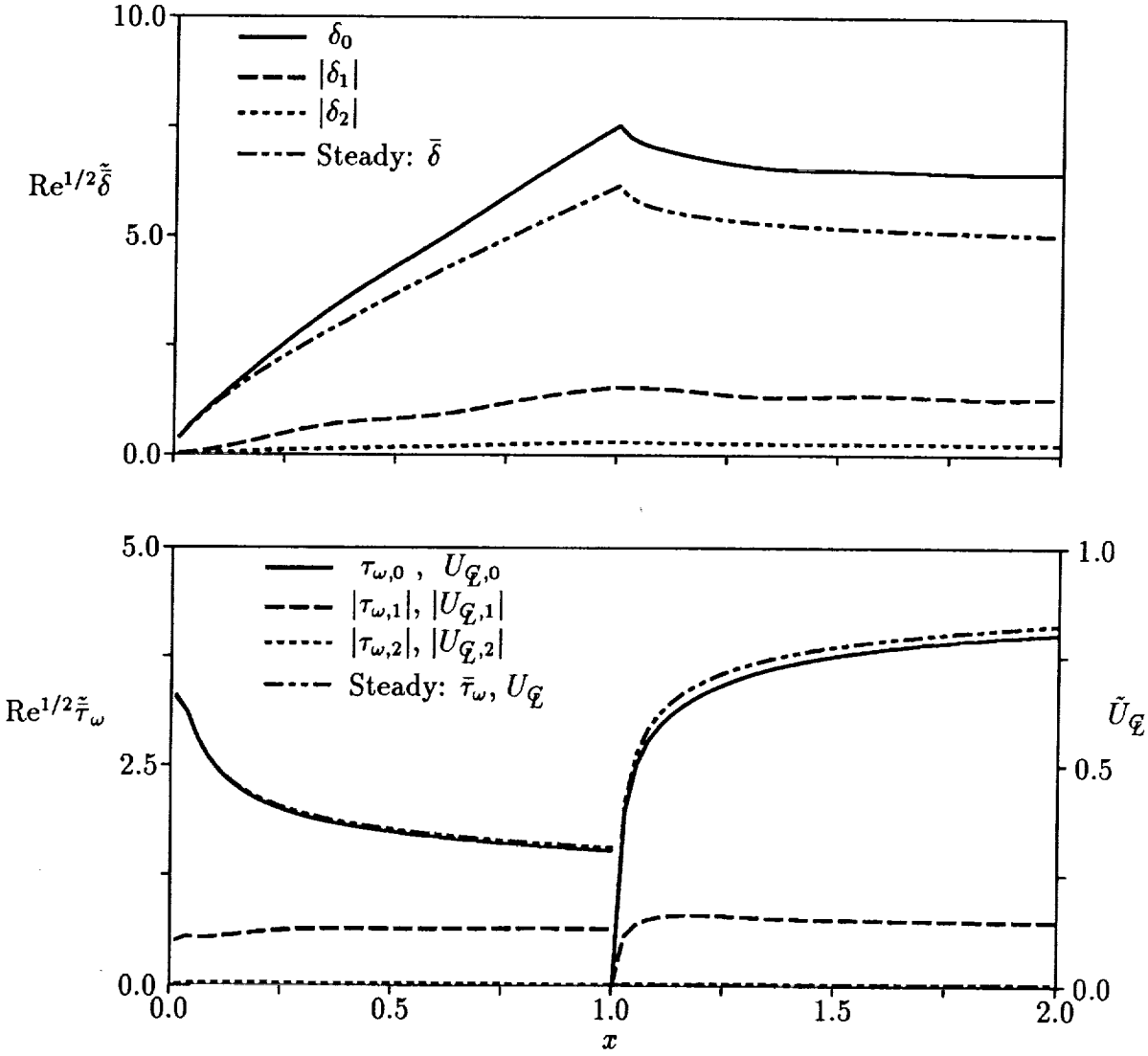

Figure 28: Temporal mean and Fourier magnitudes of the displacement thickness, $\tilde{\bar{\delta}}$, wall shear stress, $\tilde{\bar{\tau}}_\omega$, and wake centerline velocity, $\tilde{U}_{\mathcal{L}}$, for turbulent flow through an unstaggered flat-plate cascade ($\Omega = \Theta = 0\,\mathrm{deg}$, $G = 1$, $M = 0.5$ and $\mathrm{Re} = 10^6$) subjected to an incident pressure disturbance from downstream with $p_{I,+\infty} = (0.5, 0)$, $\omega = 5$ and $\sigma = 0\,\mathrm{deg}$.

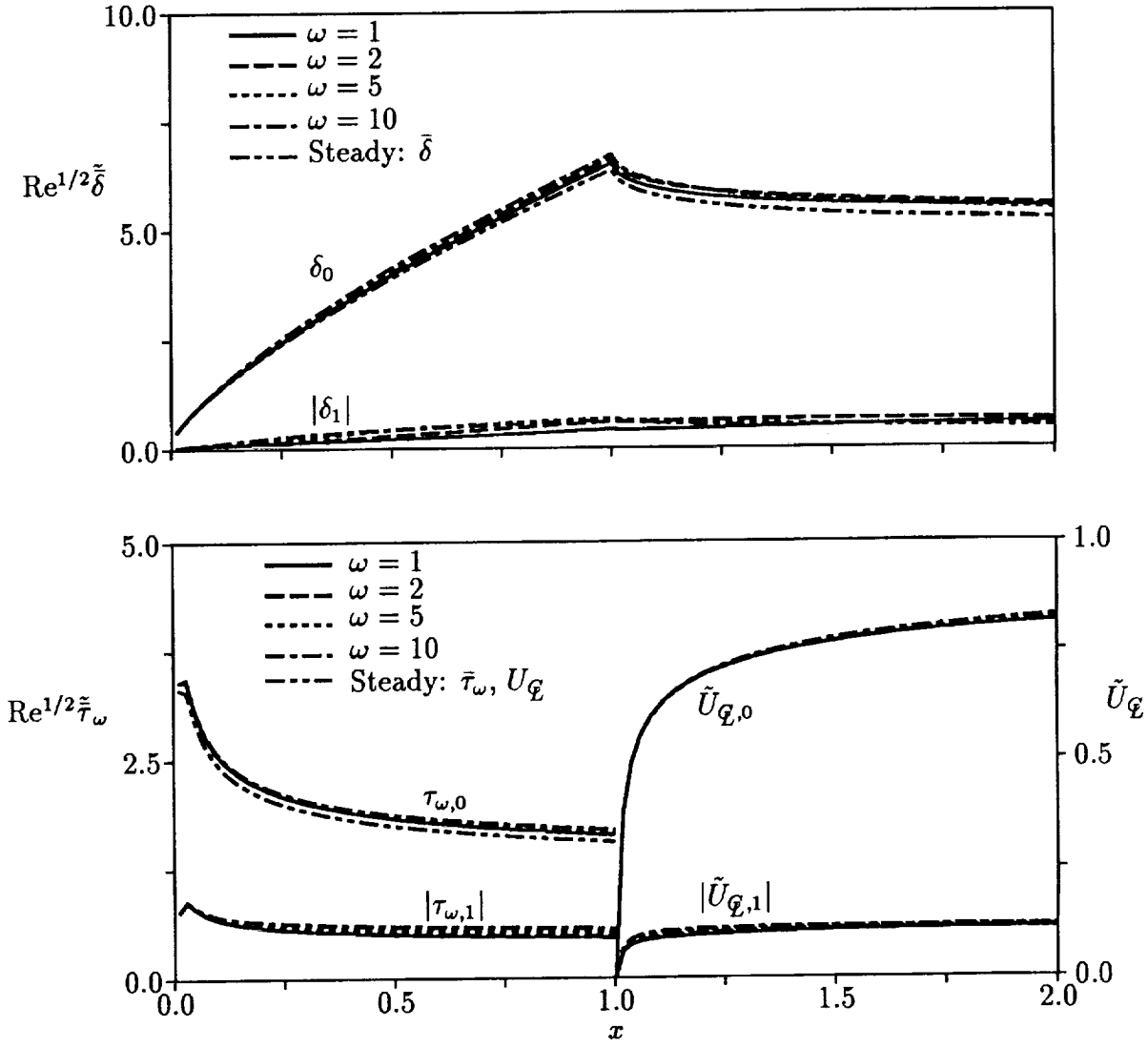

Figure 29: Fourier amplitudes of $\tilde{\bar{\delta}}$, $\tilde{\bar{\tau}}_\omega$ and $\tilde{U}_{\mathcal{L}}$ for an unstaggered flat-plate cascade ($\Omega = \Theta = 0\,\mathrm{deg}$, $G = 1$, $M = 0.5$ and $\mathrm{Re} = 10^6$) subjected to pressure excitations from upstream with $p_{I,-\infty} = (0.5, 0)$ and $\sigma = 0\,\mathrm{deg}$.

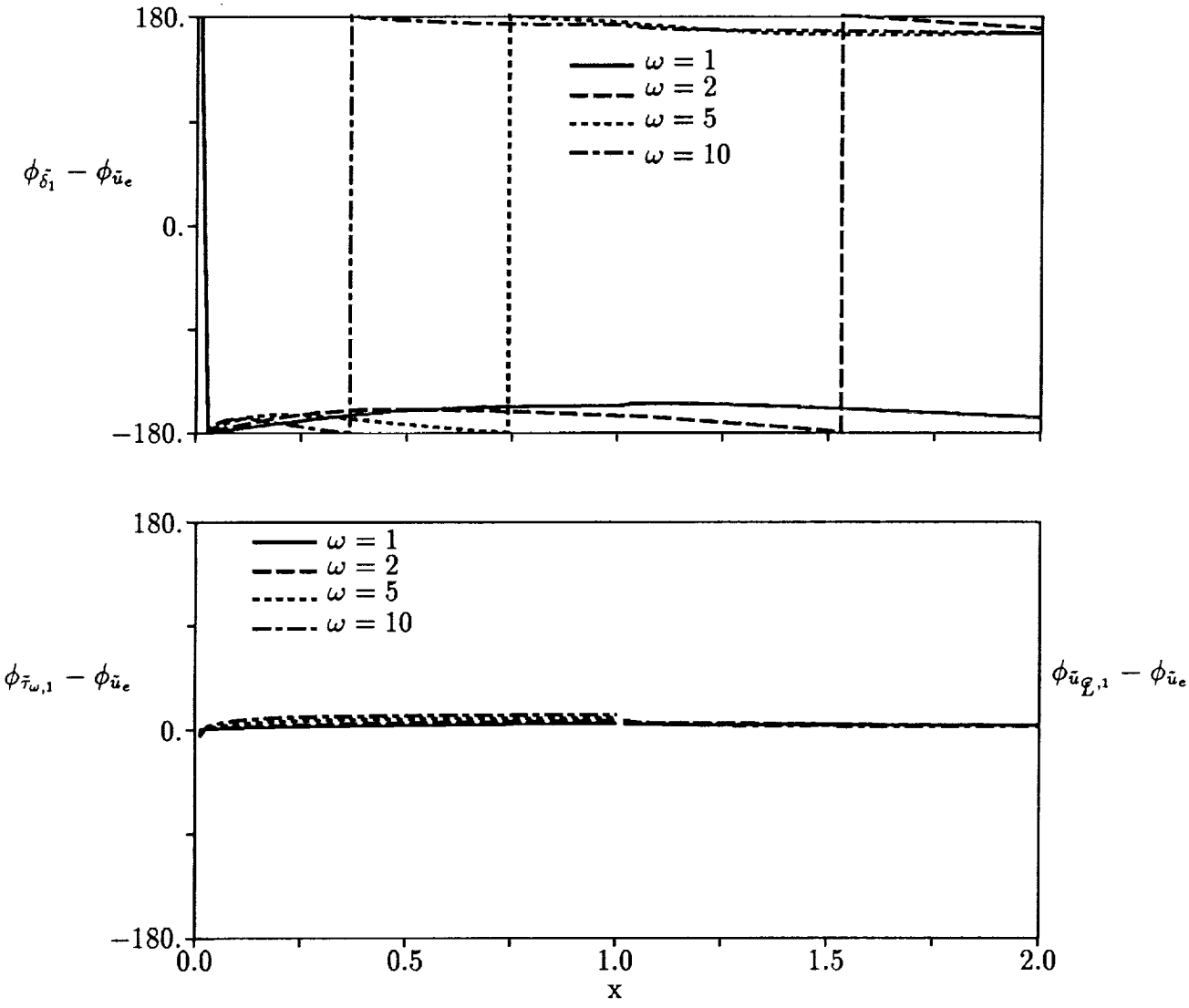

Figure 30: Relative phase angles of first-harmonic displacement thickness, wall shear stress, and wake centerline velocity for an unstaggered flat-plate cascade ($\Omega = \Theta = 0\,\text{deg}$, $G = 1$, $M = 0.5$ and $\text{Re} = 10^6$) subjected to pressure excitations from upstream with $p_{I,-\infty} = (0.5, 0)$ and $\sigma = 0\,\text{deg}$.

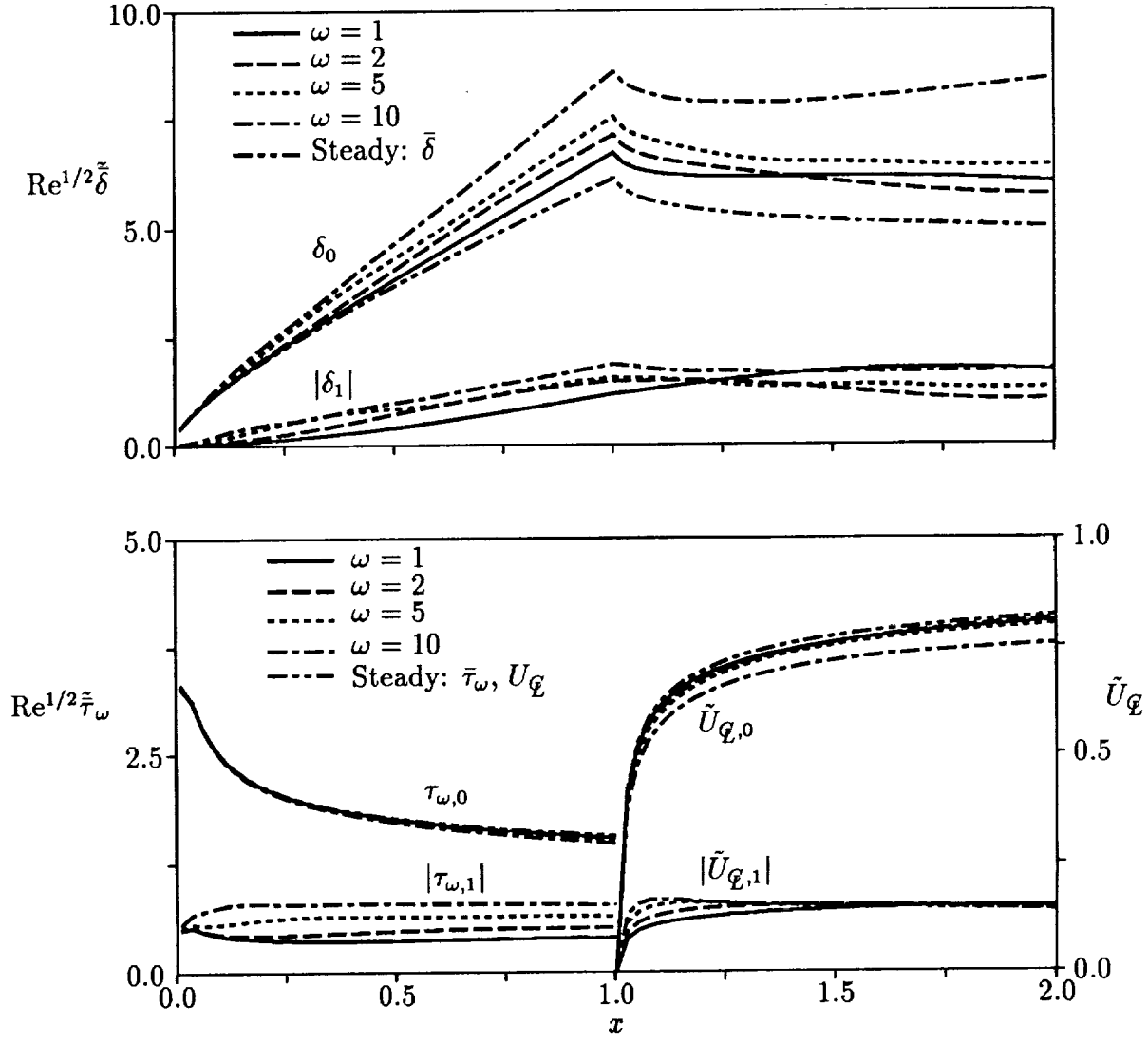

Figure 31: Fourier amplitudes of $\tilde{\bar{\delta}}$, $\tilde{\bar{\tau}}_\omega$ and $\tilde{U}_{\mathcal{L}}$ for an unstaggered flat-plate cascade ($\Omega = \Theta = 0$ deg, $G = 1$, $M = 0.5$ and $\mathrm{Re} = 10^6$) subjected to pressure excitations from downstream with $p_{I,+\infty} = (0.5, 0)$ and $\sigma = 0$ deg.

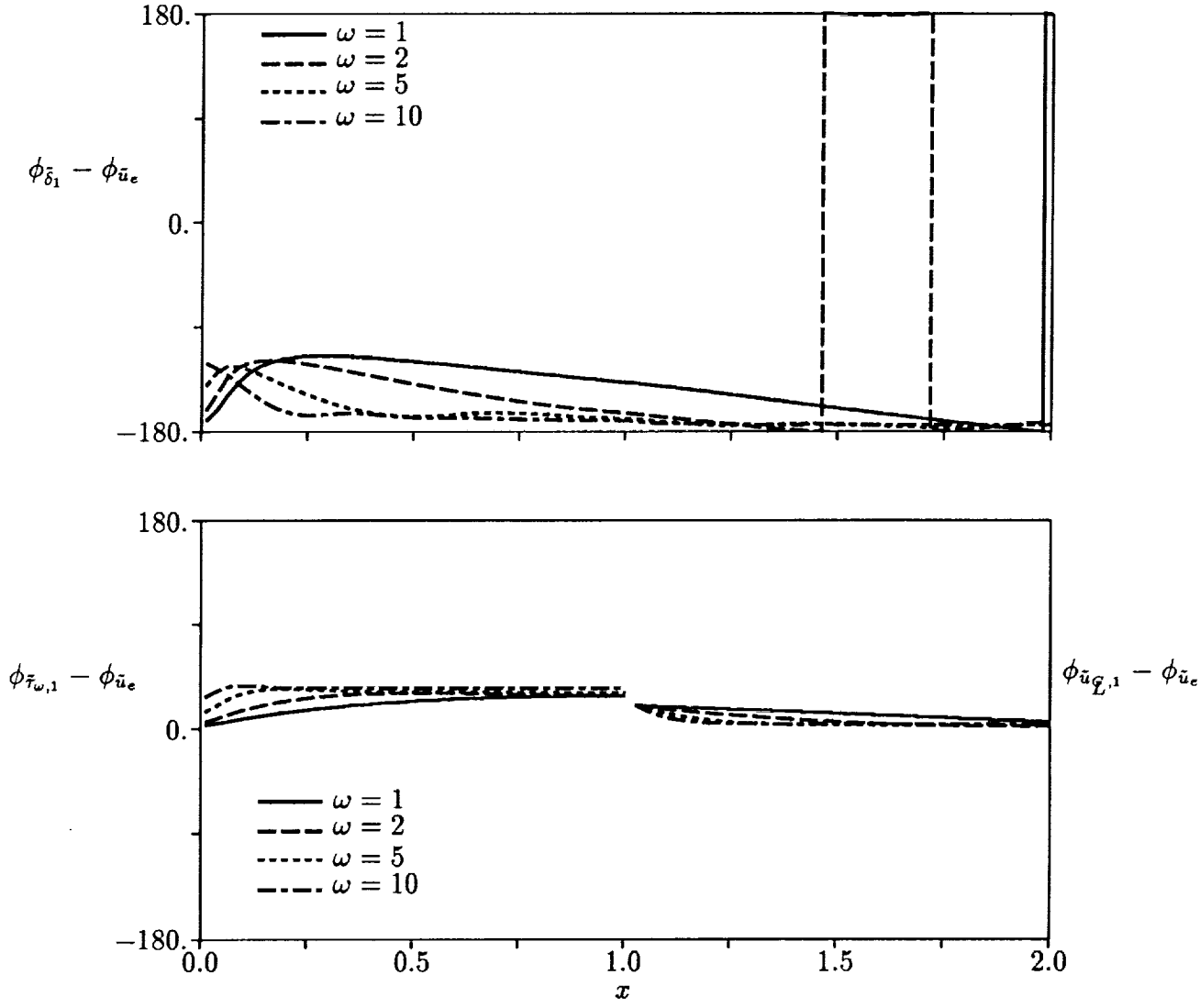

Figure 32: Relative phase angles of first-harmonic displacement thickness, wall shear stress, and wake centerline velocity for an unstaggered flat-plate cascade ($\Omega = \Theta = 0\,\text{deg}$, $G = 1$, $M = 0.5$ and $\text{Re} = 10^6$) subjected to pressure excitations from downstream with $p_{I,+\infty} = (0.5, 0)$ and $\sigma = 0\,\text{deg}$.

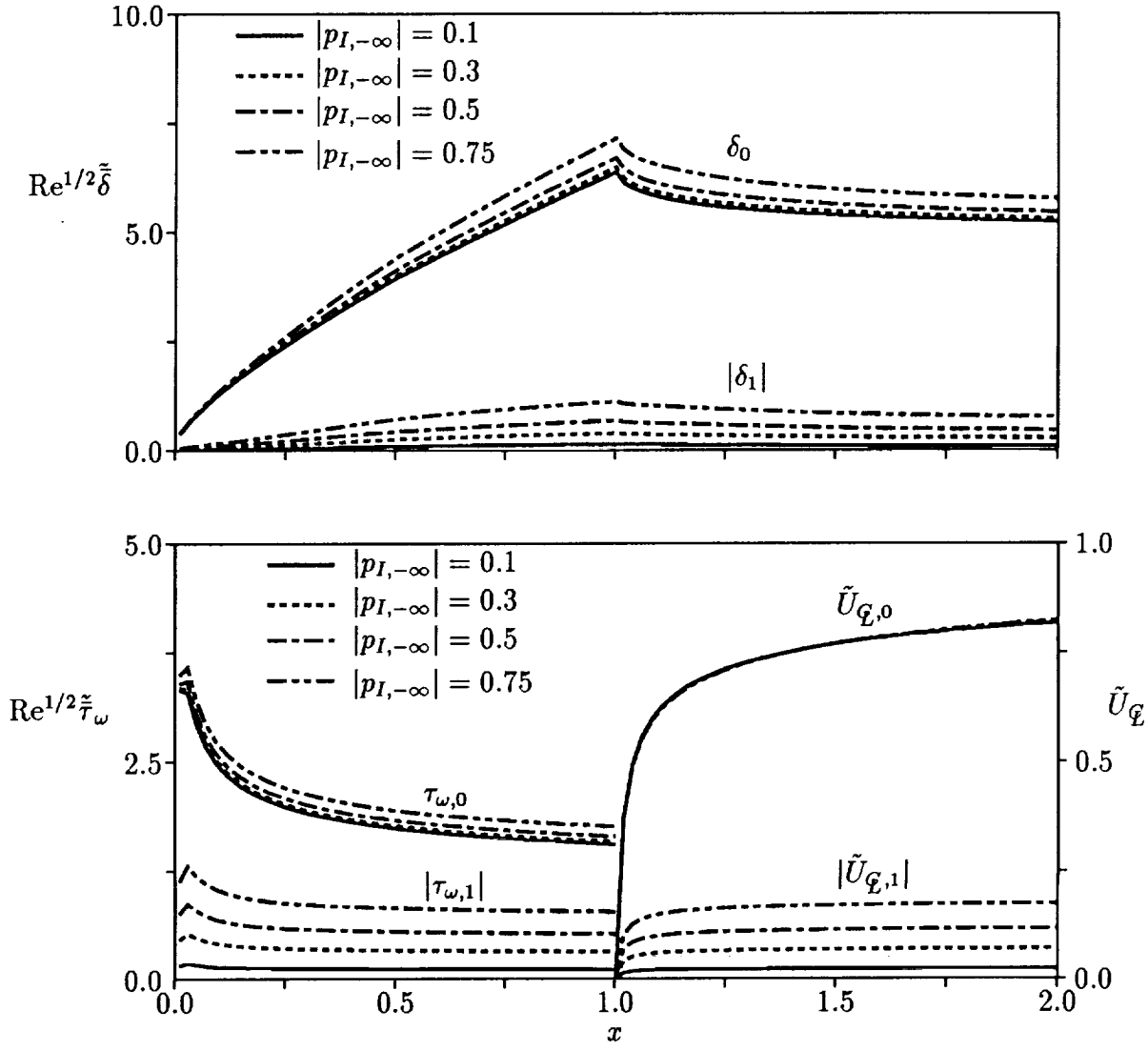

Figure 33: Fourier amplitudes of $\tilde{\bar{\delta}}$, $\tilde{\bar{\tau}}_\omega$ and $\tilde{U}_{\mathcal{L}}$ vs amplitude, $|p_{I,-\infty}|$, for an acoustic excitation from upstream, with $\omega = 5$ and $\sigma = 0\,\mathrm{deg}$, interacting with an unstaggered flat-plate cascade ($\Omega = \Theta = 0\,\mathrm{deg}$, $G = 1$, $M = 0.5$ and $\mathrm{Re} = 10^6$).

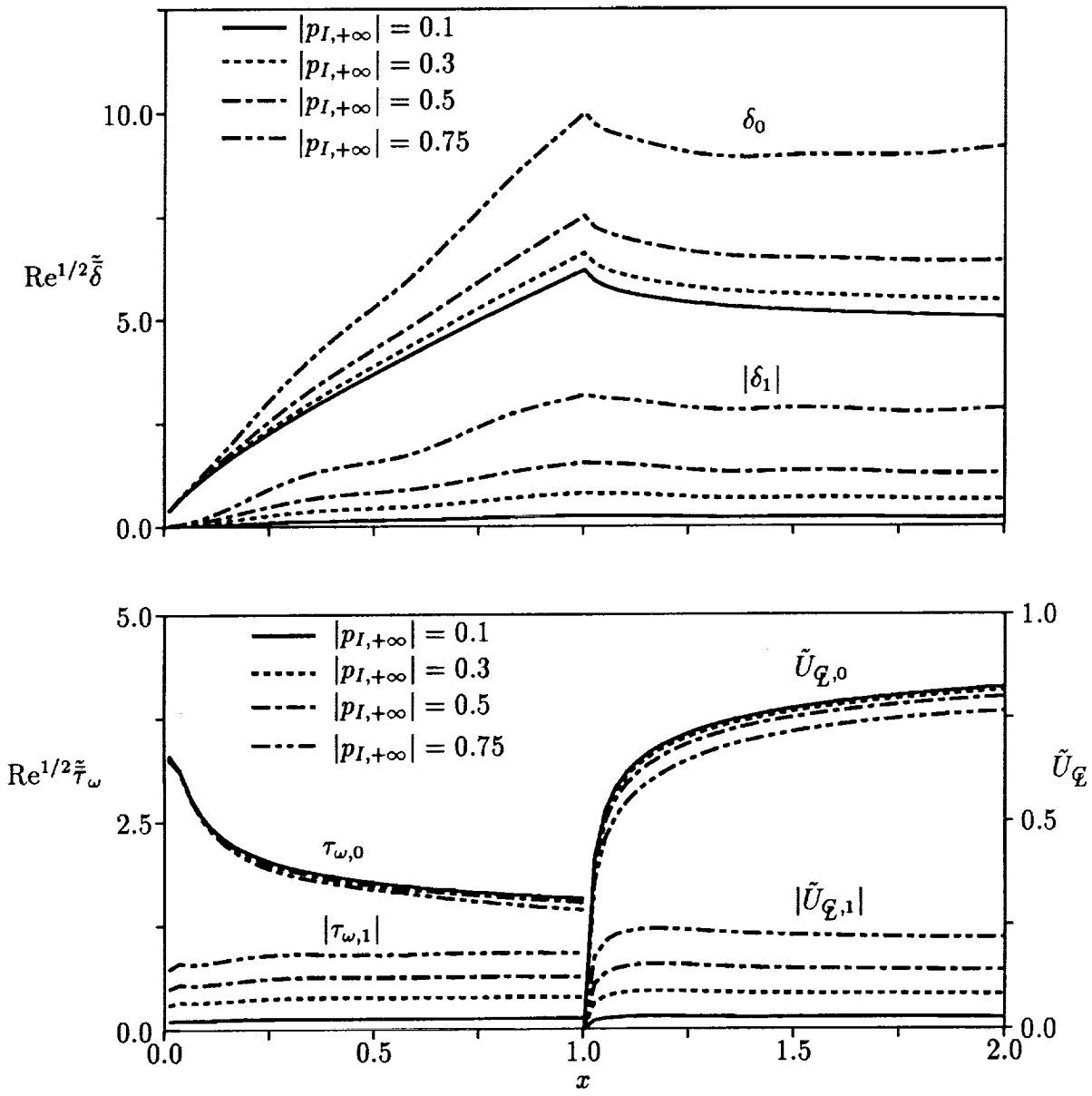

Figure 34: Fourier amplitudes of $\tilde{\bar{\delta}}$, $\tilde{\bar{\tau}}_\omega$ and $\tilde{U}_{\mathcal{L}}$ vs amplitude, $|p_{I,+\infty}|$, for an acoustic excitation from downstream with, $\omega = 5$ and $\sigma = 0$ deg, interacting with an unstaggered flat-plate cascade ($\Omega = \Theta = 0$ deg, $G = 1$, $M = 0.5$ and $\mathrm{Re} = 10^6$).

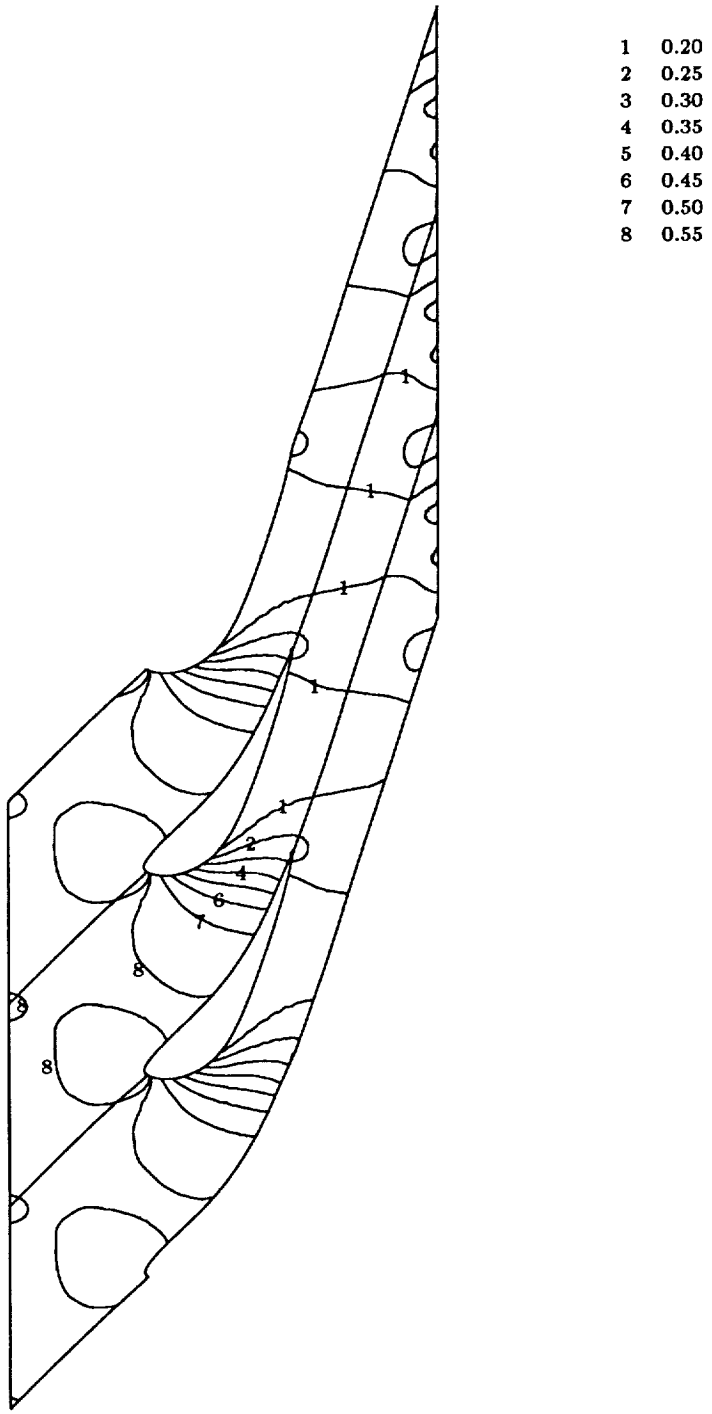

Figure 35: Contours of the in-phase component of the unsteady pressure for the turbine cascade subjected to a pressure excitation from upstream with $p_{I,-\infty} = (0.35, 0)$, $\omega = 1$ and $\sigma = 0$.

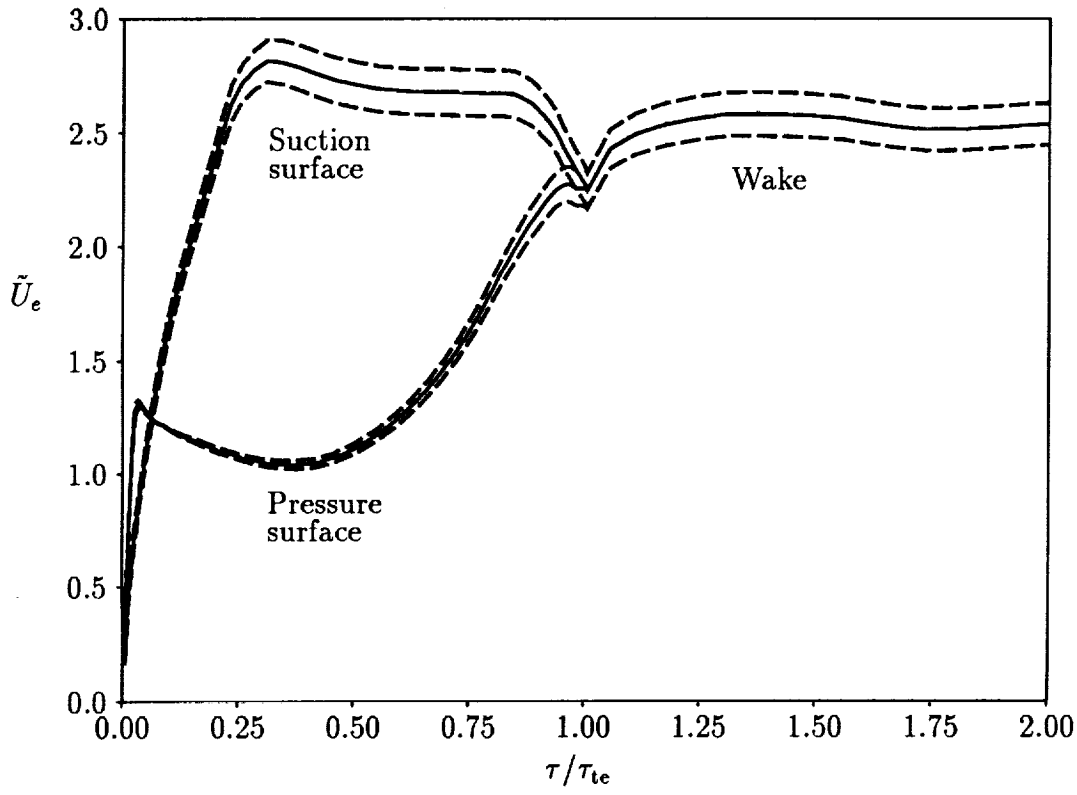

Figure 36: Temporal mean values and upper and lower bounds of the inviscid surface (viscous-layer edge) velocity for the turbine cascade subjected to an upstream pressure excitation with $p_{I,-\infty} = (0.35, 0)$, $\omega = 1$ and $\sigma = 0$.

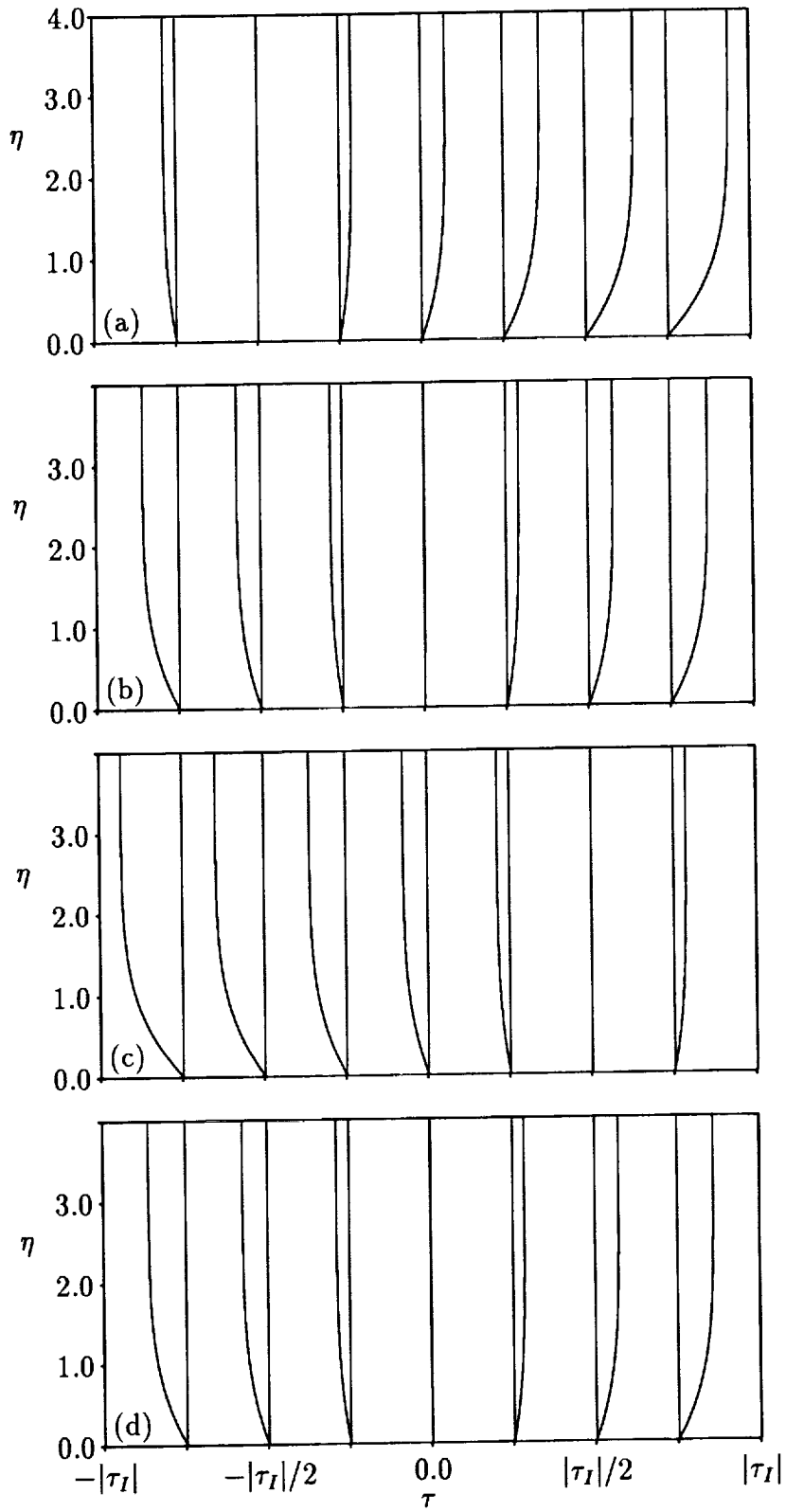

Figure 37: Velocity profiles in the neighborhood of a mean stagnation point location for the turbine cascade subjected to an upstream acoustic excitation with $p_{I,-\infty} = (0.35, 0)$, $\omega = 1$ and $\sigma = 0$: (a) $t = \pi/2$; (b) $t = \pi$; (c) $t = 3\pi/2$; (d) $t = 2\pi$.

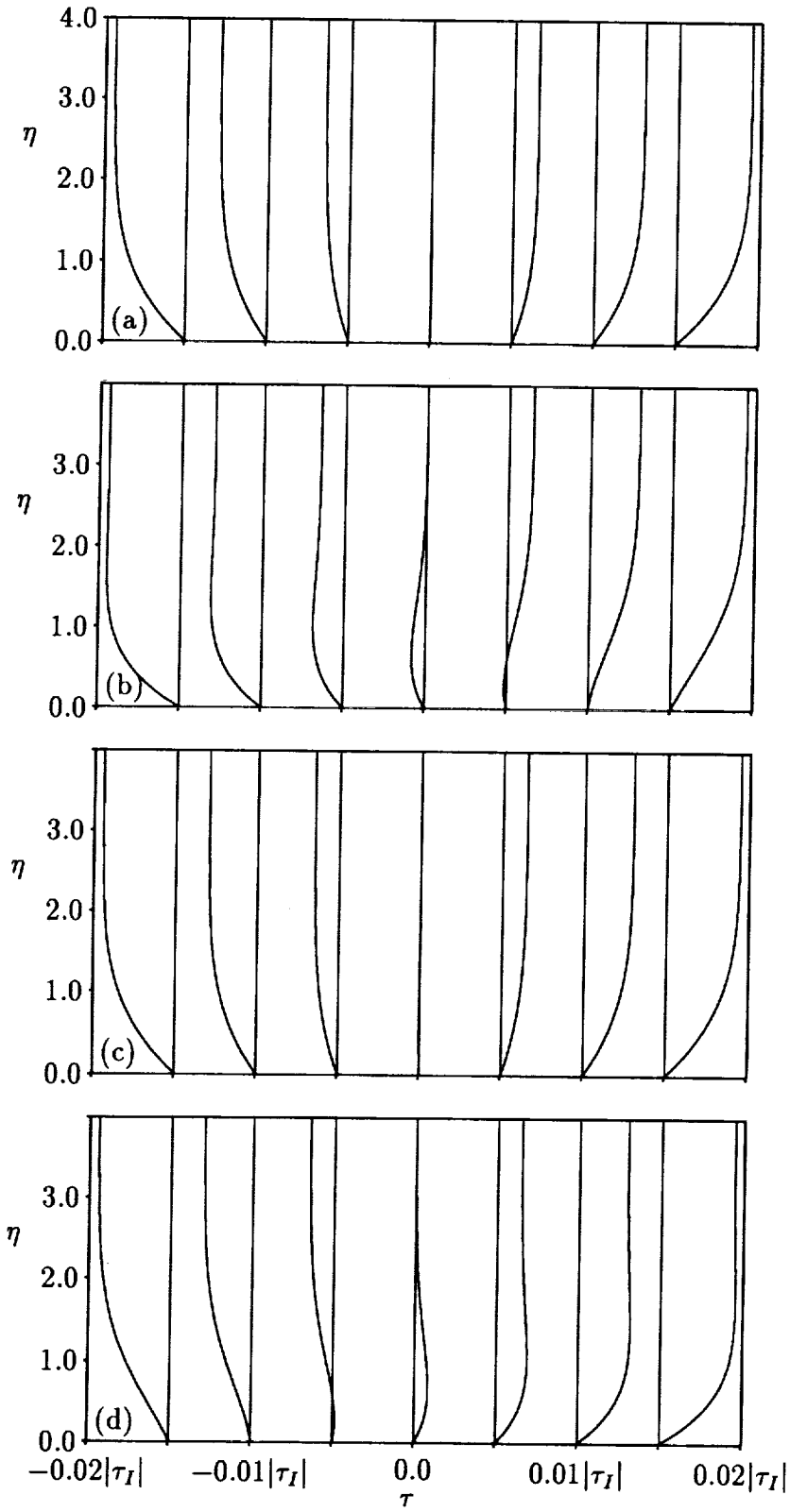

Figure 38: Velocity profiles in the neighborhood of an instantaneous stagnation point location for the turbine cascade subjected to an upstream acoustic excitation with $p_{I,-\infty} = (0.35, 0)$, $\omega = 1$ and $\sigma = 0$: (a) through (d) as in Figure 36.

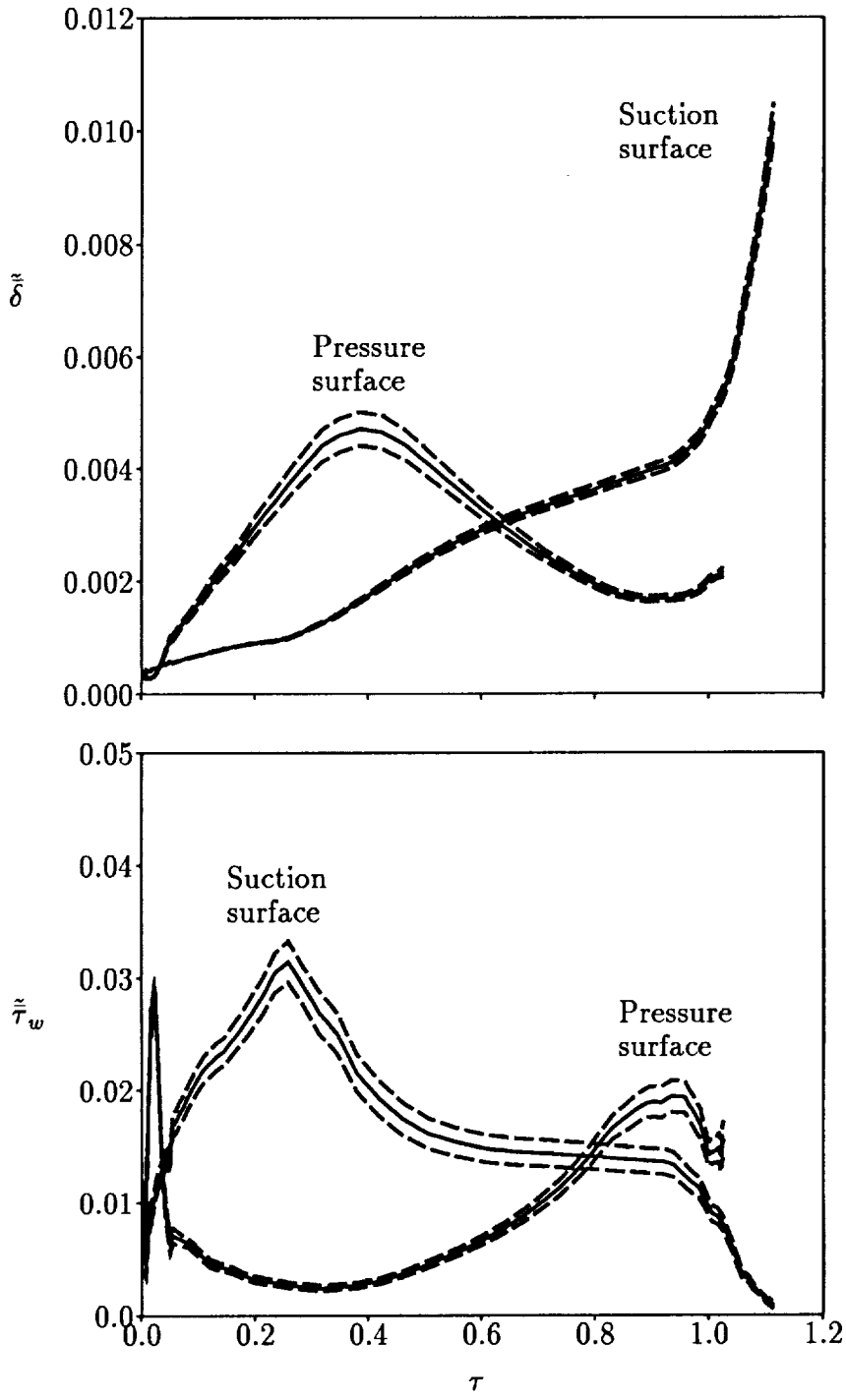

Figure 39: Temporal mean values and upper and lower bounds for the displacement thickness and surface shear stress along a turbine blade surface for an upstream pressure excitation with $p_{I,-\infty} = (0.35, 0)$, $\omega = 1$ and $\sigma = 0$.

Q-2

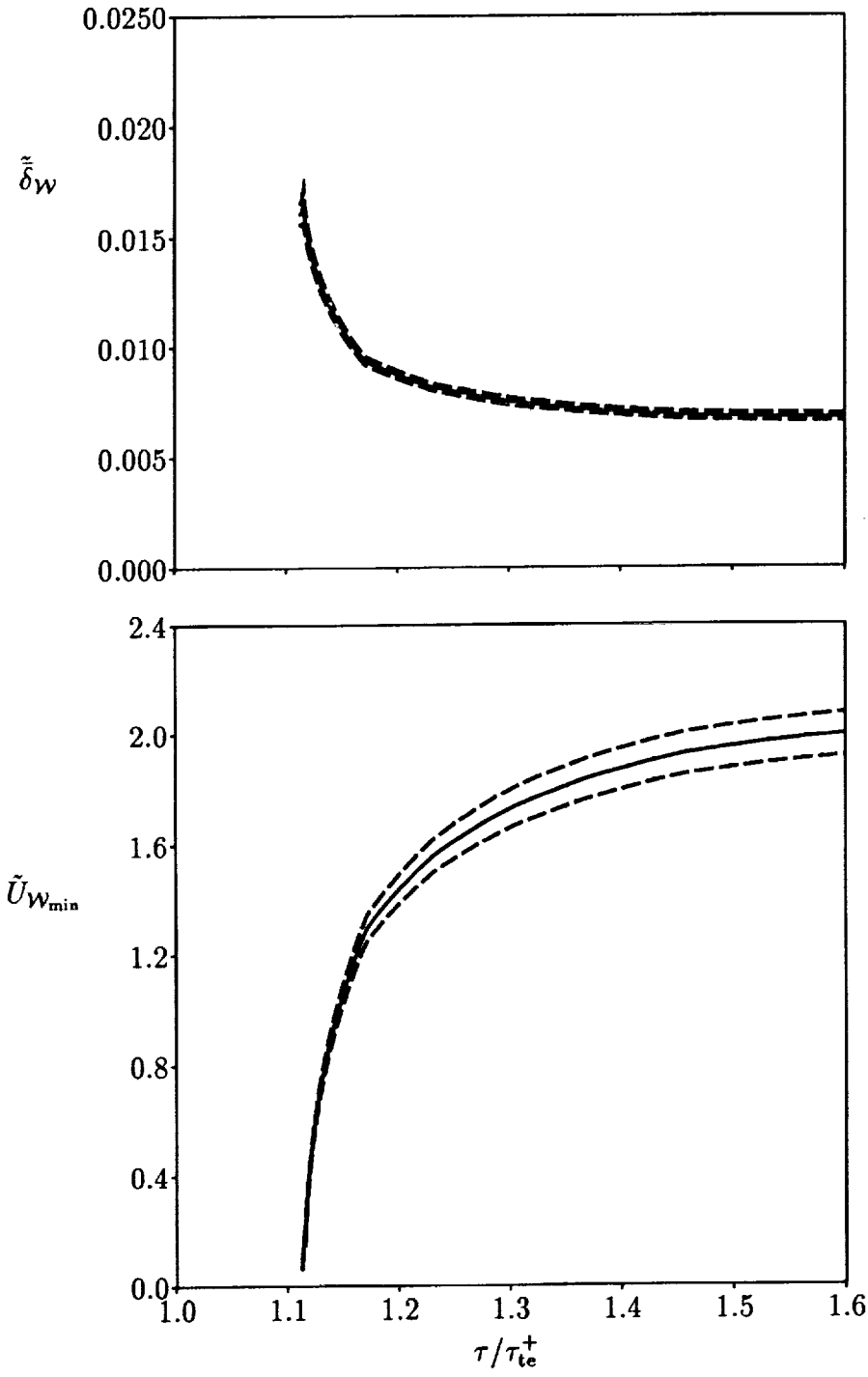

Figure 40: Temporal mean values and upper and lower bounds for the displacement thickness and minimum wake streamwise velocity along a turbine wake for an upstream pressure excitation with $p_{I,-\infty} = (0.35, 0)$, $\omega = 1$ and $\sigma = 0$.

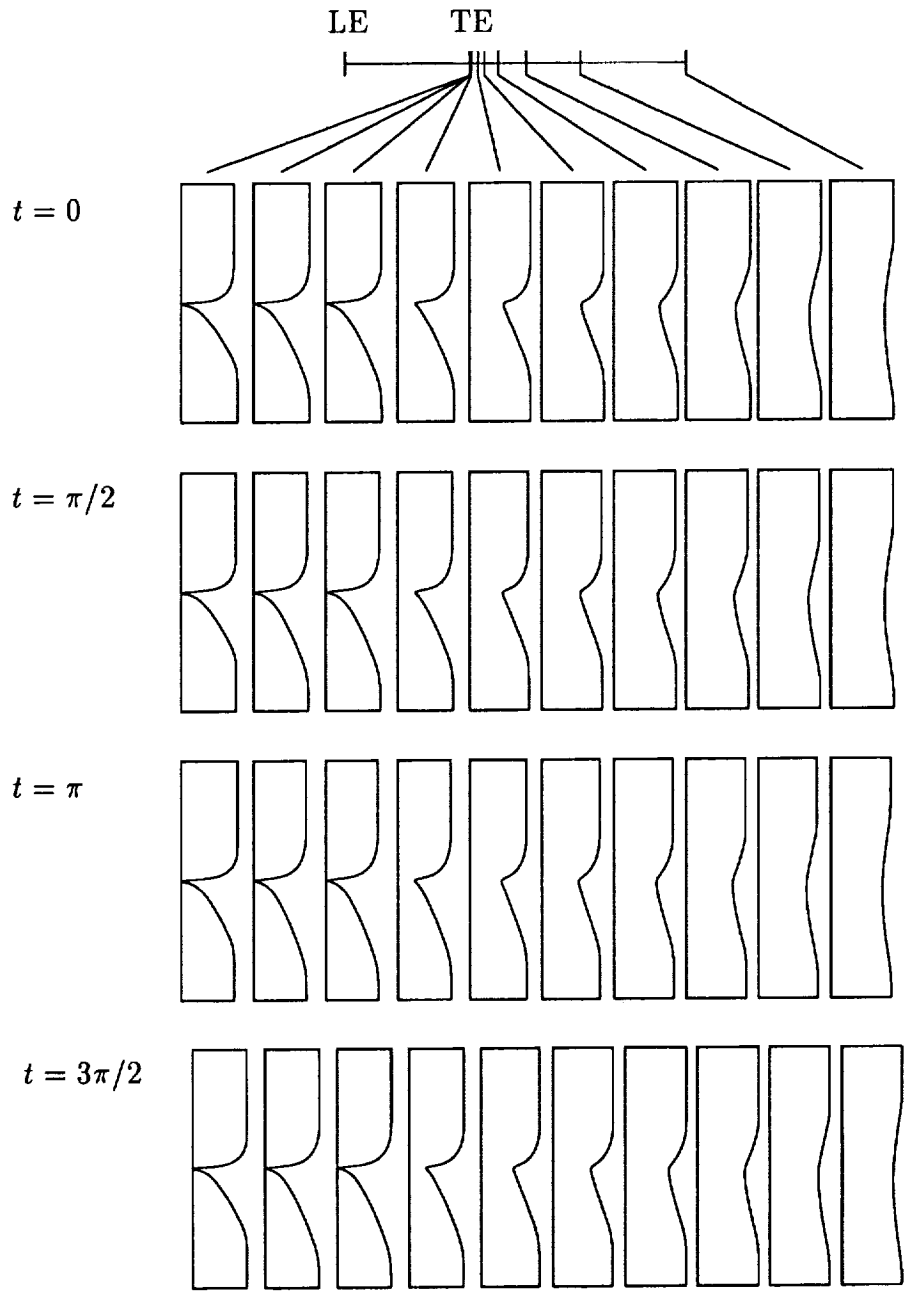

Figure 41: Streamwise velocity profiles in the wake of a turbine blade for an acoustic excitation from upstream with $p_{I,-\infty} = (0.35, 0)$, $\omega = 1$ and $\sigma = 0$.

A. Details of the Viscous-Layer Solution Procedure

The viscous-layer equations are solved numerically using an implicit finite-difference approach, which is described in this Appendix. The finite-difference approximations used to discretize the governing equations and the quasilinearization applied to the resulting system of nonlinear equations is discussed in section A.1. The recursion relations and the associated coefficients needed to solve the block-tridiagonal system of equations are given in A.2. Finally, the wake analysis is described in A.3.

A.1 Finite-Difference Approximations

The partial derivatives appearing in the governing viscous-layer equations are all first derivatives, with the exception of those accounting for viscous effects in the streamwise momentum and energy equations, which introduce second derivatives with respect to η. In the present analysis first-order accurate backward differences are used to approximate the ξ and t derivatives. First and second partial derivatives with respect to η are approximated using central differences. The notation used below is defined in the illustrations of Figures A.1 and A.2. The subscript n is the mesh-point index in the η-direction, so that $(\cdot)_n$ refers to a quantity evaluated at the location, η_n.

First derivatives of the dependent variables are written as

$$\left(\frac{\partial A}{\partial \xi}\right)_n \approx \frac{A_{2,n} - A_{3,n}}{\Delta \xi} , \tag{A.1}$$

$$\left(\frac{\partial A}{\partial t}\right)_n \approx \frac{A_{2,n} - A_{1,n}}{\Delta t} \tag{A.2}$$

and

$$\left(\frac{\partial A}{\partial \eta}\right)_n \approx \frac{A_{2,n+1} - A_{2,n-1}}{\Delta \eta_{n-1} + \Delta \eta_n} , \tag{A.3}$$

where

$$\begin{aligned} \Delta \xi &= \xi_2 - \xi_3 , \\ \Delta t &= t_2 - t_1 , \\ \Delta \eta_{n-1} &= \eta_n - \eta_{n-1} \\ \text{and} \quad \Delta \eta_n &= \eta_{n+1} - \eta_n . \end{aligned}$$

Here, the subscript 1 refers to the current ξ-station, previous time level, 2 refers to the current ξ-station and current time level (i.e., the solution station) and 3 refers to the previous ξ-station, current time level (see Figure A1). Second derivatives in the η-direction are written in the form

$$\left(\frac{\partial^2 A}{\partial \eta^2}\right)_n \approx \frac{2}{\Delta \eta_n + \Delta \eta_{n-1}} \left(\frac{(A_{n+1} - A_n)}{\Delta \eta_n} - \frac{(A_n - A_{n-1})}{\Delta \eta_{n-1}} \right) . \tag{A.4}$$

If, as in all of the calculations performed here, $|\Delta \eta_n / \Delta \eta_{n-1} - 1| \ll 1$, the η-derivatives remain formally second-order accurate.

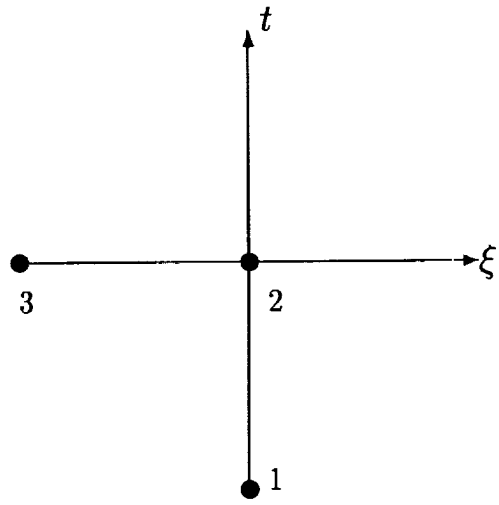

Figure A.1: Computational molecule in the ξ- and t-directions.

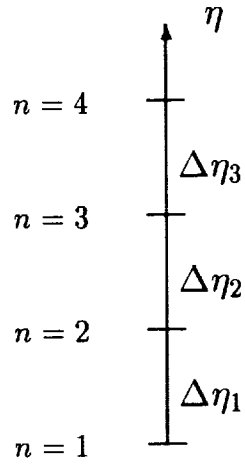

Figure A.2: Computational grid in the η-direction.

Before discretizing the equations, the continuity, Eq. (4.19), streamwise momentum (4.20) and energy (4.21) equations, respectively, are rewritten in the following forms,

$$A_1\frac{\partial \mathcal{F}}{\partial \xi}+\frac{\partial \mathcal{V}}{\partial \eta}+A_{10}\mathcal{F}+A_{11}=0\ , \tag{A.5}$$

$$A_2\frac{\partial \mathcal{F}}{\partial t}+A_1\mathcal{F}\frac{\partial \mathcal{F}}{\partial \xi}+\mathcal{V}\frac{\partial \mathcal{F}}{\partial \eta}+A_3\mathcal{F}+A_4\mathcal{F}^2+A_5\mathcal{G}-\frac{\partial}{\partial \eta}\left(l\frac{\partial \mathcal{F}}{\partial \eta}\right)=0 \tag{A.6}$$

and

$$A_2\frac{\partial \mathcal{G}}{\partial t}+A_1\mathcal{F}\frac{\partial \mathcal{G}}{\partial \xi}+\mathcal{V}\frac{\partial \mathcal{G}}{\partial \eta}+A_6\mathcal{F}\mathcal{G}+A_7\mathcal{F}^2+A_8\mathcal{G}-A_9\frac{\partial}{\partial \eta}\left[(l-\hat{l})\mathcal{F}\frac{\partial \mathcal{F}}{\partial \eta}\right]-\frac{\partial}{\partial \eta}\left(\hat{l}\frac{\partial \mathcal{G}}{\partial \eta}\right)=0\ , \tag{A.7}$$

where the coefficients $A_1, \ldots, A_{11}$ are given by [see (4.22)]

$$\begin{array}{lll} A_1 = 2\xi\bar{\mathcal{Q}}/\mathcal{Q} , & A_2 = 2\xi/(\mathcal{Q}\tilde{U}_e) , & A_3 = \alpha_1\alpha_3 , \\ A_4 = \alpha_4 + (\alpha_2\alpha_3)/2 , & A_5 = -(\alpha_4+\alpha_3) , & A_6 = \alpha_1\alpha_6 , \\ A_7 = \alpha_5 + (\alpha_2\alpha_6)/2 , & A_8 = -(\alpha_6+\alpha_5) , & A_9 = \alpha_2 , \\ A_{10} = \bar{\mathcal{Q}}/\mathcal{Q} \quad \text{and} & A_{11} = -\alpha_1\alpha_3 . & \end{array} \tag{A.8}$$

The nonlinear terms are quasilinearized by writing terms of the form AB as

$$AB \approx A\overline{B} + \overline{A}B - \overline{AB} , \tag{A.9}$$

where the overbar denotes a known quantity (e.g., from the previous iteration).

After quasilinearizing and discretizing the streamwise momentum equation, it can be written as

$$A^F_{u,n}\mathcal{F}_{2,n-1} + B^F_{u,n}\mathcal{F}_{2,n} + C^F_{u,n}\mathcal{F}_{2,n+1} + B^V_{u,n}\mathcal{V}_{2,n} + B^G_{u,n}\mathcal{G}_{2,n} = D_{u,n} , \tag{A.10}$$

where

$$A^F_{u,n} = \frac{-2l_{n-\frac{1}{2}}}{\Delta\eta_{n-1}(\Delta\eta_n + \Delta\eta_{n-1})} - \frac{\bar{\mathcal{V}}_{2,n}}{\Delta\eta_n + \Delta\eta_{n-1}} , \tag{A.11}$$

$$B^F_{u,n} = \frac{A_2}{\Delta t} + \frac{A_1}{\Delta\xi}(2\bar{\mathcal{F}}_{2,n} - \mathcal{F}_{3,n}) + A_3 + 2A_4\bar{\mathcal{F}}_{2,n} + \frac{2}{\Delta\eta_n + \Delta\eta_{n-1}}\left(\frac{l_{n+\frac{1}{2}}}{\Delta\eta_n} + \frac{l_{n-\frac{1}{2}}}{\Delta\eta_{n-1}}\right) , \tag{A.12}$$

$$C^F_{u,n} = \frac{\bar{\mathcal{V}}_{2,n}}{\Delta\eta_n + \Delta\eta_{n-1}} - \frac{2l_{n+\frac{1}{2}}}{\Delta\eta_n(\Delta\eta_n + \Delta\eta_{n-1})} , \tag{A.13}$$

$$B^V_{u,n} = \frac{\bar{\mathcal{F}}_{2,n+1} - \bar{\mathcal{F}}_{2,n-1}}{\Delta\eta_n + \Delta\eta_{n-1}} , \tag{A.14}$$

$$B^G_{u,n} = A_5 \tag{A.15}$$

and

$$D_{u,n} = \frac{A_2\mathcal{F}_{1,n}}{\Delta t} + \frac{A_1\bar{\mathcal{F}}^2_{2,n}}{\Delta\xi} + \bar{\mathcal{V}}_{2,n}\frac{\bar{\mathcal{F}}_{2,n+1} - \bar{\mathcal{F}}_{2,n-1}}{\Delta\eta_n + \Delta\eta_{n-1}} + A_4\bar{\mathcal{F}}^2_{2,n} . \tag{A.16}$$

The energy equation is similar in form to the momentum equation, except that off-diagonal terms in both $\mathcal{F}$ and $\mathcal{G}$ arise due to the presence of η-derivatives of both quantities, resulting in the quasilinear discretized form

$$A^F_{E,n}\mathcal{F}_{2,n-1} + B^F_{E,n}\mathcal{F}_{2,n} + C^F_{E,n}\mathcal{F}_{2,n+1} + B^V_{E,n}\mathcal{V}_{2,n} + A^G_{E,n}\mathcal{G}_{2,n-1} + B^G_{E,n}\mathcal{G}_{2,n} + C^G_{E,n}\mathcal{G}_{2,n+1} = D_{E,n} \tag{A.17}$$

where

$$A^F_{E,n} = \frac{2A_9(l_{n-\frac{1}{2}} - \hat{l}_{n-\frac{1}{2}})\bar{\mathcal{F}}_{2,n-1}}{\Delta\eta_{n-1}(\Delta\eta_n + \Delta\eta_{n-1})} , \tag{A.18}$$

$$B^F_{E,n} = \frac{A_1}{\Delta\xi}(\bar{\mathcal{G}}_{2,n} - \mathcal{G}_{3,n}) + A_6\bar{\mathcal{G}}_{2,n} + 2A_7\bar{\mathcal{F}}_{2,n}$$

$$- \frac{2A_9(l_{n+\frac{1}{2}} - \hat{l}_{n+\frac{1}{2}})\bar{\mathcal{F}}_{2,n}}{\Delta\eta_n(\Delta\eta_n + \Delta\eta_{n-1})} - \frac{2A_9(l_{n-\frac{1}{2}} - \hat{l}_{n-\frac{1}{2}})\bar{\mathcal{F}}_{2,n}}{\Delta\eta_{n-1}(\Delta\eta_n + \Delta\eta_{n-1})} , \tag{A.19}$$

$$C^F_{E,n} = \frac{2A_9(l_{n+\frac{1}{2}} - \hat{l}_{n+\frac{1}{2}})\bar{\mathcal{F}}_{2,n+1}}{\Delta\eta_n(\Delta\eta_n + \Delta\eta_{n-1})} , \tag{A.20}$$

$$B^V_{E,n} = \frac{\bar{\mathcal{G}}_{2,n+1} - \bar{\mathcal{G}}_{2,n-1}}{\Delta\eta_n + \Delta\eta_{n-1}} , \tag{A.21}$$

$$A^G_{E,n} = \frac{-\bar{\mathcal{V}}_{2,n}}{\Delta\eta_n + \Delta\eta_{n-1}} - \frac{2\hat{l}_{n-\frac{1}{2}}}{\Delta\eta_{n-1}(\Delta\eta_n + \Delta\eta_{n-1})} , \tag{A.22}$$

$$B^G_{E,n} = \frac{A_2}{\Delta t} + \frac{A_1}{\Delta\xi}\bar{\mathcal{F}}_{2,n} + A_6\bar{\mathcal{F}}_{2,n} + \frac{2\hat{l}_{n+\frac{1}{2}}}{\Delta\eta_n(\Delta\eta_n + \Delta\eta_{n-1})} + \frac{2\hat{l}_{n-\frac{1}{2}}}{\Delta\eta_{n-1}(\Delta\eta_n + \Delta\eta_{n-1})} + A_8 , \tag{A.23}$$

$$C^G_{E,n} = \frac{\bar{\mathcal{V}}_{2,n}}{\Delta\eta_n + \Delta\eta_{n-1}} - \frac{2\hat{l}_{n+\frac{1}{2}}}{\Delta\eta_n(\Delta\eta_n + \Delta\eta_{n-1})} \tag{A.24}$$

and

$$D_{E,n} = \frac{A_2\mathcal{G}_{1,n}}{\Delta t} + \frac{A_1}{\Delta\xi}\bar{\mathcal{F}}_{2,n}\bar{\mathcal{G}}_{2,n} + \frac{\bar{\mathcal{V}}_{2,n}}{\Delta\eta_n + \Delta\eta_{n-1}}(\bar{\mathcal{G}}_{2,n+1} - \bar{\mathcal{G}}_{2,n-1}) + A_6\bar{\mathcal{F}}_{2,n}\bar{\mathcal{G}}_{2,n} + A_7\bar{\mathcal{F}}^2_{2,n} + \frac{A_9(l_{n+\frac{1}{2}} - \hat{l}_{n+\frac{1}{2}})}{\Delta\eta_n(\Delta\eta_n + \Delta\eta_{n-1})}(\bar{\mathcal{F}}^2_{2,n+1} - \bar{\mathcal{F}}^2_{2,n}) - \frac{A_9(l_{n-\frac{1}{2}} - \hat{l}_{n-\frac{1}{2}})}{\Delta\eta_{n-1}(\Delta\eta_n + \Delta\eta_{n-1})}(\bar{\mathcal{F}}^2_{2,n} - \bar{\mathcal{F}}^2_{2,n-1}) . \tag{A.25}$$

The continuity equation, which is linear, has the discretized form

$$A^F_{c,n}\mathcal{F}_{2,n-1} + B^F_{c,n}\mathcal{F}_{2,n} + \mathcal{V}_{2,n} - \mathcal{V}_{2,n-1} = D_{c,n} \tag{A.26}$$

where

$$A^F_{c,n} = \frac{A_1\Delta\eta_{n-1}}{2\Delta\xi} + \frac{A_{10}\Delta\eta_{n-1}}{2} , \tag{A.27}$$

$$B^F_{c,n} = A^F_{c,n} \tag{A.28}$$

and

$$D_{c,n} = \frac{A_1\Delta\eta_{n-1}}{2\Delta\xi}(\mathcal{F}_{3,n} + \mathcal{F}_{3,n-1}) - A_{11}\Delta\eta_{n-1} . \tag{A.29}$$

A.2 Recursion Relations

To facilitate the solution of the above equations, the following recursion relations are introduced for $\mathcal{F}_{2,n}$ and $\mathcal{G}_{2,n}$:

$$\mathcal{F}_{2,n} = P^F_n + Q^F_n\mathcal{V}_{2,n-1} + R^F_n\mathcal{F}_{2,n-1} + T^F_n\mathcal{G}_{2,n-1} \tag{A.30}$$

and

$$\mathcal{G}_{2,n} = P^E_n + Q^E_n\mathcal{V}_{2,n-1} + R^E_n\mathcal{F}_{2,n-1} + T^E_n\mathcal{G}_{2,n-1} . \tag{A.31}$$

Substituting these expressions into the discretized governing equations and collecting terms gives

$$H^F_{1,n}\mathcal{F}_{2,n} + H^F_{2,n}\mathcal{G}_{2,n} + H^F_{3,n}\mathcal{V}_{2,n} = D^F_n - A^F_{u,n}\mathcal{F}_{2,n-1}$$

and

$$H^E_{1,n}\mathcal{F}_{2,n} + H^E_{2,n}\mathcal{G}_{2,n} + H^E_{3,n}\mathcal{V}_{2,n} = D^E_n - A^F_{E,n}\mathcal{F}_{2,n-1} - A^G_{E,n}\mathcal{G}_{2,n-1} \,, \tag{A.32}$$

where

$$\begin{aligned} H^F_{1,n} &= B^F_{u,n} + C^F_{u,n}R^F_{n+1} \,, \\ H^F_{2,n} &= B^G_{u,n} + C^F_{u,n}T^F_{n+1} \,, \\ H^F_{3,n} &= B^V_{u,n} + C^F_{u,n}Q^F_{n+1} \,, \\ D^F_n &= D_{u,n} - C^F_{u,n}P^F_{n+1} \end{aligned} \tag{A.33}$$

and

$$\begin{aligned} H^E_{1,n} &= B^F_{E,n} + C^F_{E,n}R^F_{n+1} + C^G_{E,n}R^E_{n+1} \,, \\ H^E_{2,n} &= B^G_{E,n} + C^F_{E,n}T^F_{n+1} + C^G_{E,n}T^E_{n+1} \,, \\ H^E_{3,n} &= B^V_{E,n} + C^F_{E,n}Q^F_{n+1} + C^G_{E,n}Q^E_{n+1} \,, \\ D^E_n &= D_{E,n} - C^F_{E,n}P^F_{n+1} - C^G_{E,n}P^E_{n+1} \,. \end{aligned} \tag{A.34}$$

Solving for $\mathcal{V}_{2,n}$, using continuity (A.26), and substituting into the momentum and energy equations yields

$$H^{*F}_{1,n}\mathcal{F}_{2,n} + H^{*F}_{2,n}\mathcal{G}_{2,n} = D^{*F}_n - A^{*F}_u\mathcal{F}_{2,n-1} - A^{*V}_u\mathcal{V}_{2,n-1} - A^{*G}_u\mathcal{G}_{2,n-1} \tag{A.35}$$

and

$$H^{*E}_{1,n}\mathcal{F}_{2,n} + H^{*E}_{2,n}\mathcal{G}_{2,n} = D^{*E}_n - A^{*F}_E\mathcal{F}_{2,n-1} - A^{*V}_E\mathcal{V}_{2,n-1} - A^{*G}_E\mathcal{G}_{2,n-1} \,, \tag{A.36}$$

respectively, where

$$\begin{aligned} H^{*F}_{1,n} &= H^F_{1,n} - H^F_{3,n}B^F_{c,n} \,, \\ H^{*F}_{2,n} &= H^F_{2,n} \,, \\ D^{*F}_n &= D^F_n - H^F_{3,n}D_{c,n} \,, \\ A^{*V}_u &= H^F_{3,n} \,, \\ A^{*F}_u &= A^F_{u,n} - H^F_{3,n}A^F_{c,n} \,, \\ A^{*G}_{u,n} &= 0 \end{aligned} \tag{A.37}$$

and

$$\begin{aligned} H^{*E}_{1,n} &= H^E_{1,n} - H^E_{3,n}B^F_{c,n} \,, \\ H^{*E}_{2,n} &= H^E_{2,n} \,, \\ D^{*E}_n &= D^E_n - H^E_{3,n}D_{c,n} \,, \\ A^{*V}_E &= H^E_{3,n} \,, \\ A^{*F}_E &= A^F_{E,n} - H^E_{3,n}A^F_{c,n} \,, \\ A^{*G}_E &= A^G_{E,n} \,. \end{aligned} \tag{A.38}$$

Letting b_F and b_G represent the right-hand sides of the momentum and energy equations, respectively, leads to the system of equations

$$\begin{bmatrix} H_{1,n}^{*F} & H_{2,n}^{*F} \\ H_{1,n}^{*E} & H_{2,n}^{*E} \end{bmatrix} \begin{Bmatrix} \mathcal{F}_{2,n} \\ \mathcal{G}_{2,n} \end{Bmatrix} = \begin{Bmatrix} b_F \\ b_G \end{Bmatrix} , \tag{A.39}$$

which can be solved using Cramer's rule. Defining Δ by

$$\Delta = H_{1,n}^{*F} H_{2,n}^{*E} - H_{1,n}^{*E} H_{2,n}^{*F} , \tag{A.40}$$

i.e., the determinant of the coefficient matrix, $\mathcal{F}_{2,n}$ can be written in the form

$$\begin{aligned} \mathcal{F}_{2,n} &= \frac{H_{2,n}^{*E}}{\Delta} \left(D_n^{*F} - A_u^{*V} \mathcal{V}_{2,n-1} - A_u^{*F} \mathcal{F}_{2,n-1} - A_u^{*G} \mathcal{G}_{2,n-1} \right) \\ &\quad - \frac{H_{2,n}^{*F}}{\Delta} \left(D_n^{*E} - A_E^{*V} \mathcal{V}_{2,n-1} - A_E^{*F} \mathcal{F}_{2,n-1} - A_E^{*G} \mathcal{G}_{2,n-1} \right) . \end{aligned} \tag{A.41}$$

Comparing Eq. (A.41) to Eq. (A.30) gives

$$\begin{aligned} P_n^F &= a_{11} D_n^{*F} + a_{12} D_n^{*E} , \\ Q_n^F &= -a_{11} A_u^{*V} - a_{12} A_E^{*V} , \\ R_n^F &= -a_{11} A_u^{*F} - a_{12} A_E^{*F} \\ \text{and} \qquad T_n^F &= -a_{11} A_u^{*G} - a_{12} A_E^{*G} , \end{aligned} \tag{A.42}$$

where

$$a_{11} = \frac{H_{2,n}^{*E}}{\Delta} \tag{A.43}$$

and

$$a_{12} = -\frac{H_{2,n}^{*F}}{\Delta} . \tag{A.44}$$

Analogous expressions are easily derived for $\mathcal{G}_{2,n}$.

The recursion coefficents at the η-location η_n, i.e., P_n^F, P_n^E, etc., are related to the values of the coefficients at points $m > n$ only, while the expressions for the flow variables themselves relate the unknown variables at n to the known values at points $m < n$. Therefore, the recursion coefficients can be evaluated by starting at the outer edge, $n = ne$, using the edge boundary conditions to set the values of the coefficients there, i.e.,

$$\begin{aligned} P_{ne}^F &= 1, \quad P_{ne}^E = 1 , \\ Q_{ne}^F &= 0, \quad Q_{ne}^E = 0 , \\ R_{ne}^F &= 0, \quad R_{ne}^E = 0 , \\ T_{ne}^F &= 0, \quad T_{ne}^E = 0 , \end{aligned} \tag{A.45}$$

and sweeping inward to the wall, solving for all of the coefficients. The flow variables are next determined by using the wall boundary conditions [i.e., Eq. (4.26)] to set $\mathcal{F}$, $\mathcal{V}$ and $\mathcal{G}$ at $n = 1$, and then directly applying the recursion relations to solve for the flow variables by sweeping outward from the wall to the edge of the viscous layer.

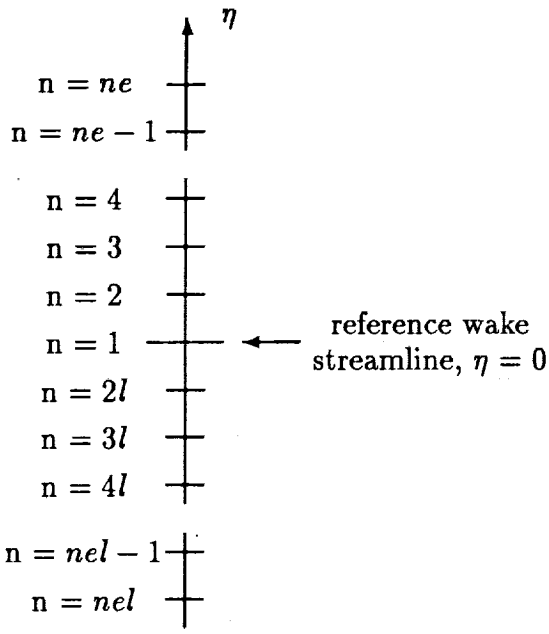

Figure A.3: Computational grid in the η-direction for the wake.

A.3 Wake Solution Procedure

The wake viscous-layer analysis is similar to the blade-surface analysis, with changes to the boundary conditions and the introduction of modifications to the definitions of some of the independent and dependent variables, as described below. Edge conditions are applied at both the upper and lower edges of the wake viscous layer and the $\eta = 0$ coordinate line is assumed to correspond to the wake reference streamline, so that $\mathcal{V} = 0$ at $\eta = 0$. As discussed in Chapter 4, the variables used in the upper- (i.e., $\eta \geq 0$) and lower-wake (i.e., $\eta < 0$) regions are defined differently, so that, for example, in the upper wake

$$\mathcal{F} \equiv \mathcal{F}^+ = \frac{\tilde{U}}{\tilde{U}_e^+} \quad \text{and} \quad \mathcal{G} \equiv \mathcal{G}^+ = \frac{\tilde{H}}{\tilde{H}_e^+} , \tag{A.46}$$

while in the lower wake

$$\mathcal{F} \equiv \mathcal{F}^- = \frac{\tilde{U}}{\tilde{U}_e^-} \quad \text{and} \quad \mathcal{G} \equiv \mathcal{G}^- = \frac{\tilde{H}}{\tilde{H}_e^-} . \tag{A.47}$$

In order to ensure that the physical variables (i.e., $\tilde{U}$, $\tilde{V}$ and $\tilde{H}$) remain continuous across the entire wake, the different variable definitions must be accounted for at the interface between the upper and lower portions of the wake, at $\eta = 0$. This is easily done when evaluating the governing equations at $\eta = 0$, where both upper- and lower-wake variables are used simultaneously.

The details of the wake solution procedure are given below. For the purpose of the present discussion, we assume that the mesh-point index in the η direction, n, is equal to one at $\eta = 0$ and increases in the $+\eta$-direction (i.e., in the upper wake), with $n = ne$ at the

upper edge of the η-mesh. In the lower wake, the mesh-point index is given by $2l$, $3l$,..., nel, ascending with increasing distance from the reference wake streamline (see Figure A.3), with $n = nel$ at the lower edge of the η-mesh..

Wake Boundary Conditions

The boundary conditions for the wake are given in Eqs. (4.25) and (4.27). The implementation of these conditions into the numerical algorithm is discussed below.

The recursion relations used in the wake are defined like on the blade surface, i.e., in the upper-wake region,

$$\mathcal{F}_{2,n} = P_n^F + Q_n^F \mathcal{V}_{2,n-1} + R_n^F \mathcal{F}_{2,n-1} + T_n^F \mathcal{G}_{2,n-1} \tag{A.48}$$

and

$$\mathcal{G}_{2,n} = P_n^E + Q_n^E \mathcal{V}_{2,n-1} + R_n^E \mathcal{F}_{2,n-1} + T_n^E \mathcal{G}_{2,n-1} \ , \tag{A.49}$$

and in the lower-wake region,

$$\mathcal{F}_{2,nl} = P_{nl}^F + Q_{nl}^F \mathcal{V}_{2,(n-1)l} + R_{nl}^F \mathcal{F}_{2,(n-1)l} + T_{nl}^F \mathcal{G}_{2,(n-1)l} \tag{A.50}$$

and

$$\mathcal{G}_{2,nl} = P_{nl}^E + Q_{nl}^E \mathcal{V}_{2,(n-1)l} + R_{nl}^E \mathcal{F}_{2,(n-1)l} + T_{nl}^E \mathcal{G}_{2,(n-1)l} \ . \tag{A.51}$$

With the edge conditions on $\mathcal{F}$ and $\mathcal{G}$ given at $n = ne$ and $n = nel$, the edge values of the recursion relations are written as

$$P_{ne}^F = P_{nel}^F = P_{ne}^E = P_{nel}^E \equiv 1 \ , \tag{A.52}$$

$$Q_{ne}^F = Q_{ne}^E = R_{ne}^F = R_{ne}^E = T_{ne}^F = T_{ne}^E \equiv 0 \tag{A.53}$$

and

$$Q_{nel}^F = Q_{nel}^E = R_{nel}^F = R_{nel}^E = T_{nel}^F = T_{nel}^E \equiv 0 \ . \tag{A.54}$$

The recursion relation coefficients are determined by applying Eqs. (A.42) in both the upper- and lower-wake regions.

The values of $\mathcal{F}$ and $\mathcal{G}$ at the wake reference streamline ($n = 1$) are determined by writing the momentum and energy equations there, substituting the recursion relations from the points immediately above and below this line (i.e., at $n = 2$ and $n = 2l$, respectively), and simultaneously solving the resulting equations. The governing equations are written at $n = 1$ in terms of upper-wake variables, so that whenever a value of $\mathcal{F}$ or $\mathcal{G}$ at $n - 1 = 2l$ is used, it is transformed to the appropriate form. Thus, at $n = 1$,

$$\mathcal{F}_{2,n-1} = \frac{\tilde{U}_e^-}{\tilde{U}_e^+} \mathcal{F}_{2,2l} \ \text{ and } \ \mathcal{G}_{2,n-1} = \frac{\tilde{H}_e^-}{\tilde{H}_e^+} \mathcal{G}_{2,2l} \ . \tag{A.55}$$

The discretized s-momentum equation at the point $n = 1$, with the boundary condition $\mathcal{V}_{2,1} = 0$ incorporated, is

$$A_{u,1}^F \frac{\tilde{U}_e^-}{\tilde{U}_e^+} \mathcal{F}_{2,2l} + B_{u,1}^F \mathcal{F}_{2,1} + C_{u,1}^F \mathcal{F}_{2,2} + B_{u,1}^G \mathcal{G}_{2,1} = D_{u,1} \ . \tag{A.56}$$

The recursion relations for $\mathcal{F}$, written at $n = 2$ and $n = 2l$ after expressing $\mathcal{F}$ and $\mathcal{G}$ at $n = 1$ in terms of upper variables, are given by

$$\mathcal{F}_{2,2} = P_2^F + R_2^F \mathcal{F}_{2,1} + T_2^F \mathcal{G}_{2,1}$$

and (A.57)

$$\mathcal{F}_{2,2l} = P_{2l}^F + R_{2l}^F \frac{\tilde{U}_e^+}{\tilde{U}_e^-} \mathcal{F}_{2,1} + T_{2l}^F \frac{\tilde{H}_e^+}{\tilde{H}_e^-} \mathcal{G}_{2,1} \ .$$

Using Eq. (A.58) for $\mathcal{F}_{2,2}$ in the momentum equation gives

$$H_{1,1}^F \mathcal{F}_{2,1} + H_{2,1}^F \mathcal{G}_{2,1} = D_{u,1}^F - A_{u,1}^F \frac{\tilde{U}_e^-}{\tilde{U}_e^+} \mathcal{F}_{2,2l} \ , \tag{A.58}$$

where

$$\begin{aligned} H_{1,1}^F &= B_{u,1}^F + C_{u,1}^F R_2^F \ , \\ H_{2,1}^F &= B_{u,1}^G + C_{u,1}^F T_2^F \\ \text{and} \quad D_{u,1}^F &= D_{u,1} - C_{u,1}^F P_2^F . \end{aligned} \tag{A.59}$$

Similarly, substituting for $\mathcal{F}_{2,2l}$ in Eq. (A.58) yields

$$H_1^{*F} \mathcal{F}_{2,1} + H_2^{*F} \mathcal{G}_{2,1} = D_1^{*F} \ , \tag{A.60}$$

where

$$\begin{aligned} H_1^{*F} &= H_{1,1}^F + A_{u,1}^F R_{2l}^F \ , \\ H_2^{*F} &= H_{2,1}^F + A_{u,1}^F T_{2l}^F \frac{\tilde{U}_e^-}{\tilde{U}_e^+} \frac{\tilde{H}_e^+}{\tilde{H}_e^-} \\ \text{and} \quad D_1^{*F} &= D_{u,1}^F - A_{u,1}^F \frac{\tilde{U}_e^-}{\tilde{U} u_e^+} P_{2l}^F \ . \end{aligned} \tag{A.61}$$

The same procedure is applied to the energy equation, which is written at $n = 1$ in the form

$$A_{E,1}^F \frac{\tilde{U}_e^-}{\tilde{U}_e^+} \mathcal{F}_{2,2l} + B_{E,1}^F \mathcal{F}_{2,1} + C_{E,1}^F \mathcal{F}_{2,2} + A_{E,1}^G \frac{\tilde{H}_e^-}{\tilde{H}_e^+} \mathcal{G}_{2,2l} + B_{E,1}^G \mathcal{G}_{2,1} + C_{E,1}^G \mathcal{G}_{2,2} = D_{E,1} \ , \tag{A.62}$$

where $\mathcal{V}_{2,1}$ has been eliminated. The recursion relations for $\mathcal{G}$, written at $n = 2$ and $n = 2l$ after expressing $\mathcal{F}$ and $\mathcal{G}$ at $n = 1$ in terms of upper variables, are given by

$$\mathcal{G}_{2,2} = P_2^E + R_2^E \mathcal{F}_{2,1} + T_2^E \mathcal{G}_{2,1}$$

and (A.63)

$$\mathcal{G}_{2,2l} = P_{2l}^E + R_{2l}^E \frac{\tilde{U}_e^+}{\tilde{U}_e^-} \mathcal{F}_{2,1} + T_{2l}^E \frac{\tilde{H}_e^+}{\tilde{H}_e^-} \mathcal{G}_{2,1} \ .$$

Substituting for $\mathcal{F}_{2,2}$ and $\mathcal{G}_{2,2}$ in Eq. (A.62) yields

$$H^E_{1,1}\mathcal{F}_{2,1} + H^E_{2,1}\mathcal{G}_{2,1} = D^E_1 - A^F_{E,1}\frac{\tilde{U}^-_e}{\tilde{U}^+_e}\mathcal{F}_{2,2l} - A^G_{E,1}\frac{\tilde{H}^-_e}{\tilde{H}^+_e}\mathcal{G}_{2,2l} \ , \tag{A.64}$$

where

$$\begin{aligned} H^E_{1,1} &= B^F_{E,1} + C^F_{E,1}R^F_2 + C^G_{E,1}R^E_2 \ , \\ H^E_{2,1} &= B^G_{E,1} + C^F_{E,1}T^F_2 + C^G_{E,1}T^E_2 \\ \text{and} \quad D^E_1 &= D_{E,1} - C^F_{E,1}P^F_2 - C^G_{E,1}P^E_2 \ . \end{aligned} \tag{A.65}$$

Substituting for $\mathcal{F}_{2,2l}$ and $\mathcal{G}_{2,2l}$ gives

$$H^{*E}_1\mathcal{F}_{2,1} + H^{*E}_2\mathcal{G}_{2,1} = D^{*E}_1 \tag{A.66}$$

where

$$\begin{aligned} H^{*E}_1 &= H^E_{1,1} + A^F_{E,1}R^F_{2l} + A^G_{E,1}R^E_{2l}\frac{\tilde{U}^+_e}{\tilde{U}^-_e}\frac{\tilde{H}^-_e}{\tilde{H}^+_e} \ , \\ H^{*E}_2 &= H^E_{2,1} + A^F_{E,1}T^F_{2l}\frac{\tilde{U}^-_e}{\tilde{U}^+_e}\frac{\tilde{H}^+_e}{\tilde{H}^-_e} + A^G_{E,1}T^E_{2l} \\ \text{and} \quad D^{*E}_1 &= D^E_1 - A^F_{E,1}P^F_{2l}\frac{\tilde{U}^-_e}{\tilde{U}^+_e} - A^G_{E,1}P^E_{2l}\frac{\tilde{H}^-_e}{\tilde{H}^+_e} \ . \end{aligned} \tag{A.67}$$

With the starred coefficients defined in this form, Eqs. (A.60) and (A.66) can be solved as before, to yield

$$\mathcal{F}_{2,1} = \frac{H^{*E}_2}{\Delta}D^{*F}_1 - \frac{H^{*F}_2}{\Delta}D^{*E}_1 \tag{A.68}$$

and

$$\mathcal{G}_{2,1} = -\frac{H^{*E}_1}{\Delta}D^{*F}_1 + \frac{H^{*F}_1}{\Delta}D^{*E}_1 \ , \tag{A.69}$$

where

$$\Delta = H^{*F}_1 H^{*E}_2 - H^{*F}_2 H^{*E}_1 \ . \tag{A.70}$$

Note that these reference streamline values are expressed in terms of upper-wake variables.

The solution in the wake is computed as follows. Using the edge conditions for the upper- and lower-wake viscous layers, the recursion relation coefficients for each are computed by sweeping inward from the edges to the centerline. The flow variables $\mathcal{F}_{2,1}$ and $\mathcal{G}_{2,1}$ are calculated from Eqs. (A.68) and (A.69), yielding their upper-wake values (i.e., $\mathcal{F}^+_{2,1}$ and $\mathcal{G}^+_{2,1}$). The quantities $\mathcal{F}$ and $\mathcal{G}$ at $n = 1$ need to be re-expressed in in terms of the lower-wake variables, in order to apply the recursion relations, Eqs. (A.50) and (A.51), to obtain the solution in the lower-wake region. These are calculated from the expressions

$$\mathcal{F}^-_{2,1} = \frac{\tilde{U}^+_e}{\tilde{U}^-_e}\mathcal{F}^+_{2,1} \quad \text{and} \quad \mathcal{G}^-_{2,1} = \frac{\tilde{H}^+_e}{\tilde{H}^-_e}\mathcal{G}^+_{2,1} \ . \tag{A.71}$$

With the variables at $n = 1$ known, including $\mathcal{V}_{2,1}$ from the boundary condition applied there, the recursion relations and the continuity equation are used to solve for all of the unknowns at each mesh point, sweeping from $n = 2$ to $n = ne$ on the upper wake and from $n = 2l$ to $n = nel$ on the lower wake.

Because the nonlinear discretized equations have been quasilinearized, the solution procedure described above is applied iteratively at each spatial and temporal location, until the local solution has converged to a specified tolerance level.

REPORT DOCUMENTATION PAGE

Form Approved
OMB No. 0704-0188

1. AGENCY USE ONLY (*Leave blank*)	2. REPORT DATE	3. REPORT TYPE AND DATES COVERED
	October 1991	Interim Contractor Report

4. TITLE AND SUBTITLE

Development of Unsteady Aerodynamic Analyses for Turbomachinery Aeroelastic and Aeroacoustic Applications

5. FUNDING NUMBERS

WU 505-63-5B
and 590-21-31
C NAS3-25425

6. AUTHOR(S)

Joseph M. Verdon, Mark Barnett, Kenneth C. Hall, and Timothy C. Ayer

7. PERFORMING ORGANIZATION NAME(S) AND ADDRESS(ES)

United Technologies Research Center
Silver Lane
East Hartford, Connecticut 06108-1049

8. PERFORMING ORGANIZATION REPORT NUMBER

E-6528

9. SPONSORING/MONITORING AGENCY NAMES(S) AND ADDRESS(ES)

National Aeronautics and Space Administration
Lewis Research Center
Cleveland, Ohio 44135-3191

10. SPONSORING/MONITORING AGENCY REPORT NUMBER

NASA CR-4405
R91-957907-3

11. SUPPLEMENTARY NOTES

Project Manager, George Stefko, Structures Division, NASA Lewis Research Center, (216) 433-3920.

12a. DISTRIBUTION/AVAILABILITY STATEMENT

Unclassified - Unlimited
Subject Category 02

12b. DISTRIBUTION CODE

13. ABSTRACT (*Maximum 200 words*)

Theoretical analyses are being developed to predict compressible unsteady inviscid and viscous flows through blade rows. Flows driven by small-amplitude unsteady excitations in which viscous effects are concentrated in thin layers are being considered. The resulting analyses should apply in many practical situations, lead to a better understanding of the relevant physics, and they should be efficient computationally and therefore appropriate for aeroelastic and aeroacoustic design applications. Under Task III of this research program, a composite (global/local) mesh gust response capability for the linearized inviscid component of the flow has been developed, and an existing nonlinear viscous-layer analysis has been extended and coupled to the inviscid analysis to provide a weak inviscid/viscid interaction solution capability for unsteady subsonic cascade flows. The linearized inviscid and the nonlinear viscous layer analyses are described in detail in this report. Numerical results are also presented to illustrate the effects of vortical excitation on the inviscid pressure response and acoustic excitation on the viscous-layer response for representative two-dimensional compressor, turbine and flat plate cascades. These results show that nonuniform mean flow phenomena can have a substantial impact on the pressure response of cascades to vortical gusts. In addition, the viscous-layer responses to acoustic excitations from upstream tend to be linear, but acoustic excitations from downstream, which travel against the main stream flow direction, excite significant nonlinear responses. Finally, because of boundary layer separation, a strong, or simultaneous, coupling of the inviscid and viscous-layer analyses must be developed to provide a useful unsteady viscous aerodynamic analysis for realistic cascade configurations.

14. SUBJECT TERMS

Forced response; Cascade; Aeroelastic; Aeroacoustic; Boundary layer; Vortical gust; Entropic gust

15. NUMBER OF PAGES
112

16. PRICE CODE
A06

17. SECURITY CLASSIFICATION OF REPORT	18. SECURITY CLASSIFICATION OF THIS PAGE	19. SECURITY CLASSIFICATION OF ABSTRACT	20. LIMITATION OF ABSTRACT
Unclassified	Unclassified	Unclassified	